A Data Storage System Based on Patterned Magnetic Media and Magnetic Force Microscopy

by

Jungmok Bae

B.S., Mechanical Engineering
Seoul National University, 1992

M.S., Mechanical Engineering
Massachusetts Institute of Technology, 1994

**Submitted to the Department of Mechanical Engineering
In Partial Fulfillment of the Requirements for the Degree of
Doctor of Philosophy in Mechanical Engineering**

at the

MASSACHUSETTS INSTITUTE OF TECHNOLOGY

May 1999
June 1999

Signature of Author _____
Department of Mechanical Engineering
May 17, 1999

Certified by _____
Dr. Kamal Youcef-Toumi
Professor of Mechanical Engineering
Thesis Supervisor

Accepted by _____
Dr. Ain A. Sonin
Chairman, Department Committee on Graduate Students

Acknowledgements

First, I dedicate this work to my grand father, Donghwan Bae, who passed away last month.

Last 6 years in Boston will remain a special memory in my life. I will remember those times as the most meaningful times in my life. I had enjoyed and I especially thank many friends who encouraged me when I had difficult times.

I would first like to thank professor Kamal Youcef-Toumi for his continued support and encouragements. It was a great opportunity to know Kamal both as a research advisor and as a friend. I thank him that he helped me throughout the thesis writing, especially when I had to leave suddenly to Korea for my military service. I had a great fun struggling with a new topic. It surely required a lot of work and patience, but turned out to be such an exciting topic.

I also want to thank Hank Smith for giving me a great opportunity to work in his laboratory. I would like to thank Prof. Caroline Ross for her support with her expertise. I would like to thank Prof. Suh, Prof. Sonin, Prof. Chun, Dr. Saka, Dr. O'handley, Dr. Moodera, and Fred Cote for their generous support and advices. Especially, I thank Leslie Reagan for all the things she did for me and Libby Shaw who helped me when I had to struggle with that MFM – it surely was a difficult machine to deal with. I would like to thank Mark who helped me make the samples and also Maya, Minha, Tim, Michael and all other people in NSL who taught me all the things in the lab.

I would like to thank my labmates, Florine Schmidt, Shigeru Sakuta, Bernardo, Osama, Bennie, T.J., Tetsuo, Wooseok, Kiseok, and others. I would like to thank Dr. Sang-gook Kim and all the other TMA engineers for the support.

I also would like to thank Chris, Kyungdeok, Byungwon, Haesung, Insoo, Shinsuk, Kundong, Junehee, Taejung, Junbeom, Kwangpyo, Jaekwan, Sanghoon, Sangjoon, Jinwoo, Harry, Sangwon, Kwansoo, Jisoo, Sanghee, and Seokmin for making my Boston life such a memorable one.

I especially thank Sherrie Kim for her love and supports. I would have lost my faith without her.

I would like to thank my sister, Heeyoung, and my brother, Jungwan, for always being there to cheer me.

I would like to thank my folks for their continued love and support. I will not have said enough of their concerns and love during my stay at MIT.

A Data Storage System Based on Patterned Magnetic Media
And Magnetic Force Microscope

By

Jungmok Bae

Submitted to the Department of Mechanical Engineering
On May 17, 1999 in Partial Fulfillment of the
Requirements for the Degree of Doctorate in
Mechanical Engineering

ABSTRACT

In recent years, there are increasing demands for the high performance data storage systems. Periodic arrays of nanostructured magnetic pillars have been proposed as a patterned medium for high density data storage. In patterned media, each single domain magnetic pillar is used to store one bit of data. This media can theoretically provide an extremely high recording density. A writing method, based on the point magnetic recording scheme, is suggested and tested experimentally in this thesis. By using this method, a recording density of as high as 16 Gbits/in^2 can be achieved with this perpendicular patterned media. The point magnetic recording (PMR) is based on the magnetic force microscopy (MFM). In this scheme, the MFM tip comes in contact with the sample and the magnetic field is applied by an external coil. The resulting magnetic field, concentrated near the tip, is used in the writing process. The exact writing field used in PMR process was experimentally measured and verified by simulation using a commercial magnetostatic simulation tool.

By using this method, the important properties of the patterned media were studied. First, the switching field, defined as the external field at which a pillar reverses its magnetization, was measured. The curling mode model agreed well with the experimental data obtained from the Ni pillars of 90 nm in diameter and 180 nm in height. The samples used in the measurement were fabricated using lithography and electroplating with magnetic materials such as Ni and Co. The average switching field was 420 Oe but a high non-uniformity, ranging from 200 Oe to 700 Oe was observed. Secondly, the interaction field between the pillars was studied. For the first time, we measured the interaction field directly from pillars with spacing as small as 200 nm using the PMR method. Corresponding results were generated using a model based on the dipole approximation and compared with the experimental data. A good agreement was obtained. This thesis, also, discusses some of the system level issues including the design related to the high data rate and the tracking of the individual bits for precise positioning of the head during the writing process.

Thesis Supervisor: Kamal Youcef-Toumi
Title: Professor of Mechanical Engineering

Table of Contents

List of Figures

Chapter 1
Introduction

1.1 Introduction

Recently, demands for the high performance data storage devices have been increasing rapidly due to the advent of new digital technologies such as high definition television (HDTV), global networks and high performance microprocessors. The magnetic recording industry now has annual revenues of 100 billion dollars and employs of over 500,000 people. The market is projected to grow continuously in the next decades. Such success in the data storage market brought about highly competitive atmosphere among the researchers in this field. This is well indicated in the recent growth of recording density of hard disk drives (HDD) [1]. Figure 1-1 shows the trend of the density growth during the recent two decades. According to the figure, the density has grown at a compound growth rate (CGR) of 60% increase per year in recent 10 years. Such trend appears shortly after the introduction of the magnetoresistive (MR) recording heads in 1990. This shows that the performance of the recording heads was the key design factor in increasing the recording density at that time. Recently, the recording density of 11 Gbits/in^2 was demonstrated in the laboratory and the commercial HDD products 3 Gbits/in^2 in recording density are now available[1]. According to the rate, the demonstration of 100 Gbits/in^2 will be possible by the year 2004.

Will the recording density of 100 Gbits/in^2 be ever possible? In order to discuss

[1] Check IBM's website at http://www.almaden.ibm.com for the recent updates.

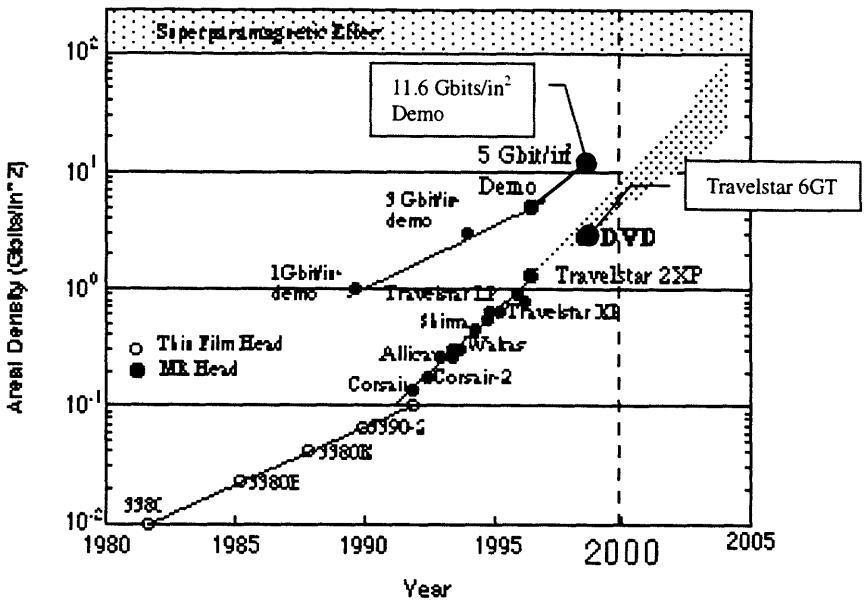

Figure 1-1 Areal density growth of the hard disk drives

this issue, we should examine the three main components of a HDD, namely recording media, recording head and positioning system. The recording media used in current HDD's are the thin film media, usually cobalt based alloys deposited on a substrate. The limiting factor of such media is the media noise. As the bits become smaller, their magnetic fields are reduced till they are finally overtaken by the random nature of the grains. In order to reduce the bit size while retaining a decent signal to noise ratio, the size of the grains should be reduced as well. However, if the grains become too small in size, the grains become thermally unstable at a normal room temperature. This is known as the superparamagnetic limit. The critical size of the grains can be estimated for various materials [2]. For the spherical Co grains, the critical diameter is about 10 nm and for the Ni grains, it is about 30 nm.[1] If the individual bit consists of 1000 grains to cancel out the random effect of the grains, the diameter of the bits becomes 100 nm for Co and 300 nm for Ni. These are the minimum sizes of the bits that can be recorded in thin film media. For the

[1] We used the equation of the magnetization reversal rate, which is a function of the anisotropy constants, temperature and volume of the grain. In the calculation, the relaxation time of 100 seconds was assumed for the superparamagnetic effect.

Co thin film media, the number indicates that the recording density can be increased up to 65 Gbits/in^2 before it meets the superparamagnetic limit.

The recording head technology had a notable progress in recent years. According to Figure 1-1, MR head technology was the main drive of the recording density growth in 1990's. The giant magnetoresistive (GMR) technology is now successfully implemented in commercial hard disk drives. The recording density of the systems using these heads was up to 11 Gbits/in^2. Currently the sensitivity of these heads is about 2 times higher than that of MR heads and projected to increase higher. The increased sensitivity makes it possible to detect smaller recorded bits and to read these bits at higher data rates. For a higher recording density, the thickness of GMR sensor should be reduced to the required size, usually smaller than the recorded bit length[1]. Currently, the fabrication of GMR heads that meet such requirements is a challenging task.

The positioning system is responsible for precise positioning of a recording head on a specified track. During a read/write process, the recording head slides on the top of a spinning disk, following the concentric circular data tracks. A small gap between the head and the disk is kept by a thin air film, generated by a rapidly spinning disk. Currently, HDD has a low track density due to its flexible structure that holds the head. A two-stage microactuator is proposed to achieve a higher track density.

The general notion is that the most critical component, limiting the areal density of 100 Gbits/in^2, is the recording media. The superparamagnetic limit of thin film media will probably limit the density higher than 50 Gbits/in^2.[2]

Optical data storage had also a notable progress in recent years. Recently, the digital video disk (DVD) is introduced in the market. The system reportedly has the areal density of 3.28 Gbits/in^2. See Figure 1-1 for the comparison. Such high recording density

---

[1] The recorded bit length for the recording density of 2.6 Gbits/in^2 is about 120 nm.
[2] The prediction is different from people to people. See for example reference [3].

was achieved because the system can provide a good signal to noise ratio down to very narrow track widths. This is possible because the optical system can afford a large working distance between the head and the media. It doesn't require a tight control of the gap as in the case of HDD. However, there are a few technical difficulties for the higher recording density applications. To detect smaller bits, an optical source with shorter wavelength should be used. Currently a semiconductor laser in a blue-purple range, stable at room temperature, is being developed but the performance vs. cost did not yet reach the proper level for commercial products. Near-field optical scanning microscope (NSOM) is another approach to increasing the detection capability.

The concept of patterned media is introduced to overcome the limitation of thin film media. The patterned media consist of periodic arrays of single domain magnetic particles fabricated using current lithography technology. Each particle is used to store one bit of data. The advantages of such media are well recognized. First, the patterned media can be a solution to overcome the superparamagnetic limit of thin film media. In thin film media, because the size and the orientations of the grains in a bit are random in nature, the signal to noise ratio (SNR) of a magnetic signal from each bit increases as the number of grains in each bit increases and therefore it averages out the effect of individual grains. As a result, to reduce the bit size while maintaining the same level of SNR, the size of grains must be reduced. There is a limit, however, in reducing the size of the grains, known as the superparamagnetic limit. At this scale, the grains are weakly coupled to each other by an exchange force so that the energy required to switch the magnetization of a grain becomes smaller than the thermal fluctuation at room temperature. As a result, all written bits are erased. In patterned media, each bit is stored in a spontaneously magnetized single domain particle, having two stable magnetic states. Since current thin film media requires bits to have 1000 grains for the adequate SNR, making the bit stored in a grain promises a 1000 times increase of a recording density.

Secondly, the patterned media do not suffer from the transition effect between neighboring bits. In thin film media, when a bit is placed next to another bit magnetized in opposite direction, a transition, called domain wall, must be formed to reduce the exchange energy. The spacing between two bits cannot be smaller than the width of the domain wall. Also, to minimize the total energy consisting of the magnetostatic force and exchange force, the transition area between two bits becomes a random zig-zag shape, called Neel spikes. Such shape can become a significant noise source in read back signal. The transition width in current thin film media runs between 40 nm and 80 nm. In patterned media, there is no transition area existing between bits, because the bits are separated by non-magnetic materials.

Thirdly, the patterned media do not have the side track problem. In thin film media, the fringing field generated at both sides of a write head creates the garbage next to the data track and therefore an extra space should be provided between the two data tracks. This limits the recording density in the radial direction.

Another advantage of the patterned media is that it provides a self tracking signal. In conventional media, the tracking is a blind motion since there is no physical boundary between the two bits when they have the same magnetization direction. Therefore the tracking must rely on the data recorded solely for the purpose of tracking. This method would not only require an accurate servo and a disk spindle motor but also use up 20% of disk space for the tracking data.

The main focus of this thesis is to design a data storage system with an extremely high recording density beyond 100 Gbits/in^2. We start from the characterization of the media property to prove and demonstrate the advantages of the patterned media in high recording density data storage. We pursue this issue further to discuss the design of an actual system based on this concept using a high resolution magnetic imaging technique called magnetic force microscopy.

1.2 Historical Review

The advantages of the patterned media were first discussed in the study of discrete track media [4-6]. Lambert et al showed that patterned track on the media can suppress the noise problems and allow a narrow track width [4][5]. Early works of fabrication and characterization of the array of submicron patterned magnetic particles were presented by Smyth et al. [7][8]. In their studies, the arrays of permalloy particles at an areal density of 160 Mbits/in^2 were fabricated by using electron beam lithography. The collective behaviors of the particles were examined with alternate gradient magnetometer (AGM). The effects of the particle size, aspect ratio, and angular dependence on the hysteresis loop parameters were studied. It was shown in their papers that the coercive force of the patterned media is much higher than the film media of the same thickness along the long axis of the particles. Schultz et al. conducted further analysis on the patterned array by using magnetic force microscope (MFM) which enabled them to observe the properties of the individual particles [9-15]. The array of permalloy bars with the size of 130 nm × 50 nm × 1,000 nm at an areal density, ranging from 220 Mbits/in^2 to 1 Gbit/in^2 were fabricated and observed with an MFM. The investigations on the switching and interaction properties of the individual particles indicated that those particles are single domains. Also, they experimentally showed that the single domain particles at such densities are actively interacting although they failed to provide quantitative data. Later, O'Bar et al. from the same group investigated the switching properties of the isolated Ni columns 120 nm in diameter and 1,400 nm in length, using an MFM and an electromagnet [12-14]. They showed that the magnetization state of the column is always in one of two equivalent, but opposite polarity states, even when the applied field was near the saturation field of the column, thus the column can be considered as a single domain. The authors also examined the relationship between the switching field and the angle of the applied field and also the switching field

and the size of the particles. They found that they agree well with the curling mode.

More experimental works have been conducted by Chou et al. [16-19]. They fabricated the arrays of Ni pillars 50 nm in diameter and 200 nm in height with an areal density of 65×10^9 pillars/in^2 using electron beam lithography. The magnetic properties of the pillars were observed with MFM. They examined the switching and interaction properties of isolated Ni and Co bars with a wider range of geometry. The Ni/Co particles with a thickness of 35 nm and a length of 1,000 nm were observed as their width varied from 30 nm to 300 nm. Also, the switching properties of the particles, 100 nm in width and 35 nm in thickness, were observed as the length varied from 100 nm to 5,000 nm. Their results showed that the pillars follow the behavior of both the multi-domains or single domain and therefore had different switching mechanisms.

White et al. provided important theoretical works regarding the patterned media [3][19-23]. They have fabricated arrays of single domain Co/Fe particles with electron beam lithography and studied the effect of magneto-crystalline, surface and shape anisotropy on the magnetic states and easy axes [20][23]. They theoretically showed that, for small size hard magnetic particles, it is difficult to have a predictable and well-defined easy axis and switching properties. They, also, showed that *[110]* single crystal iron thin film has a strong uniaxial surface anisotropy and an easy axis of magnetization lying in the *[001]* direction, regardless of the particles' shape, suggesting a new approach to making of the particle arrays with uniform magnetic properties. Shi et al. have also fabricated single domain ferromagnets in GaAs with ion implantation and subsequent heat treatment. They studied the property of the sample with MFM under the varying external magnetic field [24][25]. Fernandez et al. fabricated arrays of Co dots with spacing of 300 nm using interferometric lithography [26-28]. Later, the fabrication of 200 nm period pillar array with interferometric lithography was reported by Farhoud et al. [30]. The potential applications to the fabrication of the particle array with a period of 100 nm and below are

explained [31]. This method has been proven to be a good candidate for the mass production technology.

1.3 Thesis Outline

Chapter 2 discusses the switching properties of the patterned media. The experimental measurements were performed on the Ni nano-pillar array with a small period, 150 nm – 300 nm. A commercial MFM and an electromagnet were used to determine the switching field of each individual pillars, 90 nm in diameter and 180 nm in height. Based on the results, the single domain behavior and the switching mechanism for these pillars are discussed. This chapter also discusses the variations of the switching field for the pillars with nearly identical size, which may be critical in data storage applications. Chapter 3 discusses a possible read/write method for the high density perpendicular patterned media using magnetic force microscopy. We found that this method could readily write on the pillar array with a period of as small as 200 nm. The resolution of this technique depends on the shape of the tip and is expected to write bits with size comparable to the radius of curvature of the MFM tip, currently in the range of 30–50 nm. Chapter 4 discusses the magnetic field interactions between the pillars. The experimental method of measuring the interaction fields between individual pillars is proposed and explained. A key factor in this method is to keep the adjacent pillars in the same magnetic state during the measurement of the interaction field applied to the selected pillar. This is possible with writing method described in Chapter 3. With this method, we could measure the interaction fields between the pillars with spacing as small as 200 nm, 250 nm, and 300 nm, much smaller than previously reported. The experimental data are compared with the theoretical values calculated from the dipole approximated magnetostatic equation. Chapter 5 discusses a design of the data storage system based on the magnetic force microscopy. First, the current

performance of HDD is reviewed to determine the required specifications of the proposed system. Next, the design and the possible performance of the system based on the parallel operation of MFM recording heads are described. Calculations on various performance parameters were performed to ensure that the proposed design could become a viable high density data storage system.

Chapter 2

Switching Properties

2.1 Introduction

Coercivity is one of the key properties in the studies of fine magnetic particles. The reason is that, first, it must be sufficiently high for the particles to be of use in recording applications and it is a property, which can be naturally obtained from the computed hysteresis loop. In the case of patterned media where each bit is stored in a single domain particle, coercivity is the field that switches the magnetization direction of the particle from one state to the other state. It is also known as the switching field. The goal of this chapter is to investigate the switching properties of single domain magnetic particles in patterned media. Possible mechanisms of magnetization switching are studied by evaluating important theoretical models suggested by researchers such as Wohlfarth [32] and Frei [33].

The test samples were fabricated in the Nano-Structures Laboratory headed by Professor H. I. Smith and in the laboratory of Professor C. Ross. The samples were fabricated for the purpose of fundamental experimental characterizations on the patterned media. There were several key issues concerning a design of the samples. First, the long axis of each particle was along the axis, out of sample plane and therefore the particle has an easy axis of magnetization along that direction due to a shape anisotropy. Such particle is also called a nano-pillar or simply a pillar. The thin film media with the same axis of magnetization, called perpendicular media, have gotten attentions because it allows theoretically higher recording density than that of conventional longitudinal media. The recording density of the test samples was as high as $3x10^{10}$ bit/in^2, which is about 3 times

higher than that of current hard disk drives. Such density was chosen because this density is close to the known range of superparamagnetic limit.

Section 2.2 reviews the crystal anisotropy and a shape anisotropy, which fundamentally affect the switching properties of the pillars. Section 2.3 describes the experimental procedures and results of the measurements performed on individual pillars. This section studies in depth of the single domain behavior of each pillar and the relationship between the switching field and the geometry of the pillar array. Section 2.4 discusses theoretical models that describe the switching behaviors of the same pillars studied in previous sections. A recent trend is to calculate the switching field with a micromagnetic simulation software. Immense calculations involved in micromagnetic simulation have been possible due to the rapid development of computers. Many papers addressing the computation methods of these models have been published [34-41]. This thesis, however, takes simpler approaches, which use theoretical models based on a fundamental driving physics. A model that best describes the experimental behavior of the pillars was used to show the dependence of the switching field on the geometry and the material of the pillars. Section 2.5 discusses the variations of the switching field observed in the array where the pillars have nearly identical geometry.

2.1.1 Background

Studies of the magnetization reversal process of nano-scale ferromagnetic particles both in theory and experiment have been of interest to many researchers. A calculation of the field that rotates the M_s vector of a single domain particle out of its easy axis were performed by using micromagnetic computer simulations [34-41]. In these simulations, it was assumed that the rotation was taking place against the restoring force of some anisotropy, usually the anisotropy of shape, stress, or crystal, which depend on the shape, size, roughness and

materials properties of the particle. This aspect was also investigated by using experimental methods. Chou et al. studied the effect of a shape anisotropy on the switching field of nano-scale single domain particles by using a magnetic force microscope [16][17]. It was shown in their work that when the length of Ni bars 100 nm in width and 35 nm in thickness was increased from 500 nm to 1000 nm, the switching field increased from 450 Oe to 640 Oe, following a model of coherent switching. But, when the length was increased from 1000 nm to 5000 nm, the switching field decreased from 640 Oe to 400 Oe, showing an incoherent switching behavior. Schultz et al. [12][13] performed similar experiments. Their group showed that a Ni column of 1400 nm in length and 120 nm in diameter followed a curling mode behavior. White et al. investigated the effect of surface anisotropy in single crystal iron particles and found that the surface anisotropy was stronger than the shape anisotropy in these particles, so that the easy axis of magnetization lied in the *[001]* direction regardless of the shape of the particles.

Numerous fabrication techniques for the arrays of nano-scale ferromagnetic particles were introduced. Two-dimensional assemblies of magnetic wire or rods were made by deposition inside holes in a polymer membrane [42-44] or through pores in anodized aluminum [11][13-15]. These techniques allowed large area samples with densities up to 10^{11} bit/cm^2 and the pillar height as large as several microns. However, the spacing between the bits was random or semi-random in the case of alumina pores, making it difficult to model and to take measurements of the properties. Electron beam lithography was used by numerous researchers because it could produce particle arrays with precise dimensions and various patterns. Chou et al. fabricated high density magnetic pillar arrays with a period of 100 nm in Co or Ni by electroplating through photoresist exposed with electron beam lithography [45-47]. Interferometric lithography (IL) had recently been applied to the fabrication of nano-magnet arrays over a large area. A 300 nm period IL system was demonstrated by both Fernandez et al. [26-28] and Kirsch et al. [48] for making

arrays of magnetic dots using an evaporation and lift-off process. Farhoud et al. used electrodeposition technique to make higher aspect ratio pillars in Co and Ni with periods of 200 nm and heights up to 400 nm [30].

In this thesis, the electron beam lithography technique was used to build the array of nano-scale single domain pillars with a range of sizes and spacings. The thesis investigates the magnetic behavior of the pillars with size and spacing smaller than those previously reported. The Ni Pillars with a diameter of 90 nm, a height ranging from 130 nm to 180 nm, an spacing ranging from 150 nm to 300 nm (7 Gbit/in^2-30 Gbit/in^2) were fabricated and their magnetic properties were investigated.

2.2 Fundamental Concepts

Figure 2-1 (a) shows a diagram of perpendicular patterned media. The media consists of single domain magnetic pillars evenly embedded in a nonmagnetic filler. The orientation of the pillars' main axis is perpendicular to the surface of the medium. In the figure, the distance between the pillars is represented as S, constant for all pillars in the array. Figure 2-1 (b) shows the picture of a single pillar. The shape of the pillar is a cylinder with diameter, D, and height, H. The aspect ratio of a pillar is simply H divided by D.

Due to their size and aspect ratio, the magnetic pillars in the patterned media are assumed to be single magnetic domain in character[1]. As a result, the shape anisotropy forces the magnetization along the main axis of the pillar. A single domain particle in theory is spontaneously magnetized to the saturation magnetization, M_s, along a preferred axis of magnetization, called an easy axis. It has, therefore, only two stable states, equal in magnitude but opposite in direction. The switching process of single domain pillars can be explained with a hysteresis loop, shown in Figure 2-1 (b). If an external field is applied to

[1] See Section 2.3.4 for the detailed discussions of single magnetic domain.

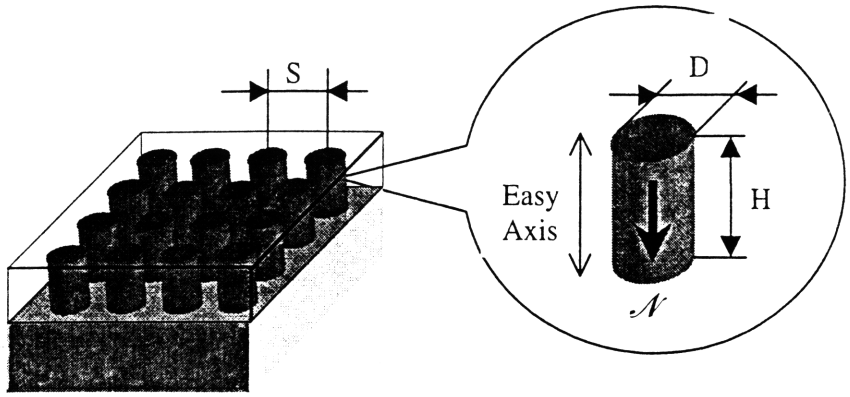

(a)

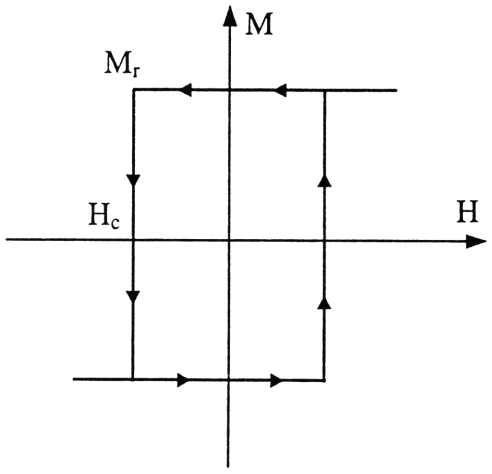

(b)

Figure 2-1 (a) Sectioned diagram of perpendicular patterned media and a single pilla magnetized in *N* direction (b) Hysteresis loop of a single magnetic domain pillar in it long axis

the pillar along its main axis and increased to H_c, the magnetization of the single domain pillar is not reduced to zero but instantly reversed to the other state.

The switching field, denoted as H_c in Figure 2-1 (b), is defined to be the magnetic field needed to reverse the magnetization of a single-domain element from one direction to the other. Among the factors that affect the switching field strength and the easy axis of the

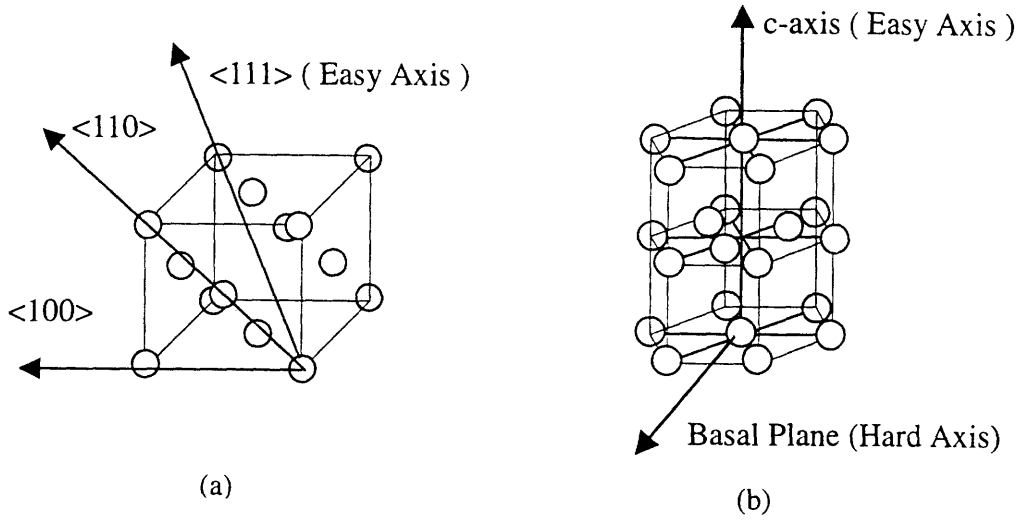

Figure 2-2 (a) Face centered cubic (FCC) crystal structure (b) Hexagonal closed-packed crystal structure

single domain particles, magnetocrystalline anisotropy[1] and the shape anisotropy are the most important ones. The magnetocrystalline anisotropy, also called crystal anisotropy, is due to the crystal structure, forcing a certain crystal direction to be an easy axis. The shape anisotropy originates from the shape of the particle. When this factor is dominant, the easy axis aligns with the long axis of the particle.

Magnetocrystalline anisotropy is mainly due to the spin-orbit coupling. The magnetization is due to the electron spin of the atoms. When the external field tries to reorient the spins and therefore to change the magnetization, it is resisted by strong coupling between the spin and the orbit, again strongly coupled with the crystal lattice. As a consequence, the magnetocrystalline anisotropy energy required to rotate the spin is the energy required to overcome the spin-orbit coupling. The strength of an anisotropy in any

[1] Anisotropy indicates that the magnetic properties depend on the direction of the measurement.

particular cubic crystal is experimentally determined by the magnitude of the anisotropy constants, K_1 and K_2. Nickel has a face centered cubic structure and the easy direction, from experiment, is known to be <111> direction. The crystal coordinates and the easy axis of single crystal Nickel is shown in Figure 2-2(a). The equation of crystal anisotropy energy for Ni is

$$E = K_0 + K_1(\alpha_1^2\alpha_2^2 + \alpha_2^2\alpha_3^2 + \alpha_3^2\alpha_1^2) + K_2(\alpha_1^2\alpha_2^2\alpha_3^2) + \Lambda \qquad (2.1)$$

where $\alpha 1$, $\alpha 2$, and $\alpha 3$ are defined as the cosines of the angles between the magnetization vector and each of the crystal axes. The easy axis is along the magnetization direction at which the energy, E, in Eq. (2.1) is minimum. Co, on the other hand, has a hexagonal closed packed structure as shown in Figure 2-2 (b). In such a structure, the hexagonal c axis is always the direction of easy magnetization and any direction in the basal plane is found to be equally hard to magnetize. In this case, the crystal anisotropy energy only depends on one angle, θ, between the magnetization vector and the c axis.

The shape anisotropy is due to the shape of a magnetic structure. If the structure is spherical in shape, there is no preferred direction of magnetization due to the shape effect. But, for a non- spherical structure, it's easier to magnetize along the long axis than the short axis. For the quantitative representation of the shape anisotropy energy, the anisotropy constant, K_s, is given by

$$K_s = \frac{1}{2}(N_a - N_c)M^2 \qquad (2.2)$$

where N_a is the demagnetizing factor along the short axis and N_c is the demagnetizing factor along the long axis for the axially symmetric case. The strength of a shape anisotropy depends on the aspect ratio of the structure, which determines the term ($N_a - N_c$) in Eq. (2.2) and the magnetization M [2]. For the case of single domain particles, M is equal to M_s, saturation magnetization.

Shape anisotropy and crystalline anisotropy are the most contributing factors that determine the switching properties of the single domain particles. But as is often the case, the one is dominant over the other and responsible for the magnetic behaviors of a particle. The switching field and the easy axis of a pillar can be estimated from the anisotropy energy equation of the dominant anisotropy energy.

2.3 Switching Field Measurement

In this section, we present the results of the switching field measurements, performed on the nano-pillar arrays with various geometries. First, the experimental setup, test structures, and experimental procedures are described. The next part presents the experimental results of the switching field measurements. These include the hysteresis loop of a few selected pillars and the graphs showing the switching field properties.

2.3.1 Experimental Setup

Figure 2-3 shows the experimental setup used in the switching field measurement. The setup can be divided into a writing module and a reading module as depicted in the figure. The reading module checks the magnetization state of the pillars at each time a field is applied. The writing module applies specified magnetic fields to the pillars under observations. For our case, the field should be applied along the pillar's long axis, perpendicular to the media surface.

The reading module must meet the following requirements.

- The sensitivity should be high enough to detect a weak flux from a single pillar. Nickel pillar, 90nm in diameter and 180 nm in height, the magnetic moment, available for the

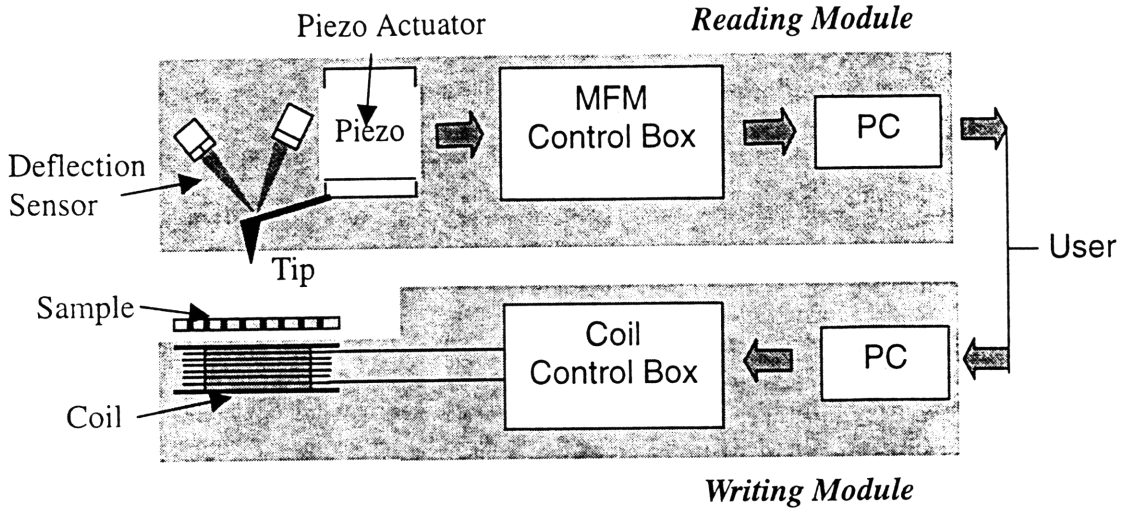

Figure 2-3 Experimental setup for the switching field measurement

sensor is only about $5.53X10^{-13}$ emu.

- The spatial resolution of the sensor should be in the order of nano-meters. Such resolution is needed to observe the magnetic pattern of the pillars.

The magnetic force microscope (MFM) meets these requirements well by providing high field sensitivity and an excellent spatial resolution. The MFM is a scanning probe microscopy (SPM) techniques, which uses a fine probe and high resolution actuators to measure extremely small quantities of surface properties. The main purpose of these instruments is to measure the surface topography in an atomic scale resolution. The MFM uses a probe coated with magnetic material to image the magnetic patterns on the sample. During the imaging, a probe consisting of a sharp tip and a flexible cantilever is oscillated near the sample surface and moved along the sample surface while the distance between the tip and sample is kept constant. At the same time, the shifts in resonant frequency are monitored by measuring the phase of the cantilever's oscillation relative to the drive signal. The phase change measured at each location on the sample constitutes a data set that can be mapped to the magnetic force gradient image of the area. The tip-sample distance for MFM

imaging is about 100nm, long enough to avoid the effect of van der Waals force[1]. The resolution of MFM depends heavily on the quality of the tip. Currently, for a normal MFM mode, the resolution is about 10nm.

Other similar instruments for the imaging of nano-scale magnetic domains include Lorentz microscopy [49-50], electron holography [51][52], and spin polarized scanning electron microscope [53]. These techniques have comparable resolutions but require a cumbersome vacuum process.

Figure 2-4 shows the detailed description of the experimental setup used in the switching field measurement. A commercial MFM, Dimension 3500 by Digital Instruments, was used as a reading module. In the system, a piezoelectric scanner consisting of piezoelectric stack and flexures is used to position the probe to required locations. The moving range of the scanner is approximately 90 μm in horizontal direction and 6 μm in vertical direction. The scanner is closed-loop controlled in all three directions and maintains the resolution down to 1 nm[2]. Such a feature removes the effect of the hysteresis and creep behavior, usually observed in piezoelectric actuators, and allows more accurate and faster imaging. The system also has a separate piezoelectric actuator for the oscillation of the cantilever and a lock-in amplifier for AC detection imaging. These components are needed in MFM and Tapping mode scan[3]. The D3500 has an XY stage for the macro-positioning of the sample and a vacuum chuck for fixing of the sample. In our setup, the vacuum chuck is used to hold both the coil and the sample. See Figure 2-4.

---

[1] MFM measurement usually runs in two scans per line. In the first pass, the topography is measured near the sample and, in the second pass, the magnetic force gradient is measured at some lifted height above the sample topography. This is to remove the effect of the topography in the magnetic measurement.

[2] Note that the resolution in vertical direction during contact AFM mode is much higher than 1 nm since the atomic force data sensed by the cantilever is used to control the vertical motion of the tip.

[3] Tapping mode, patented by Digital Instruments, is one of the AFM imaging techniques. During the imaging, the cantilever oscillates while the tip lightly touches the sample surface. The amplitude of the cantilever oscillations are monitored and mapped into the topographic image.

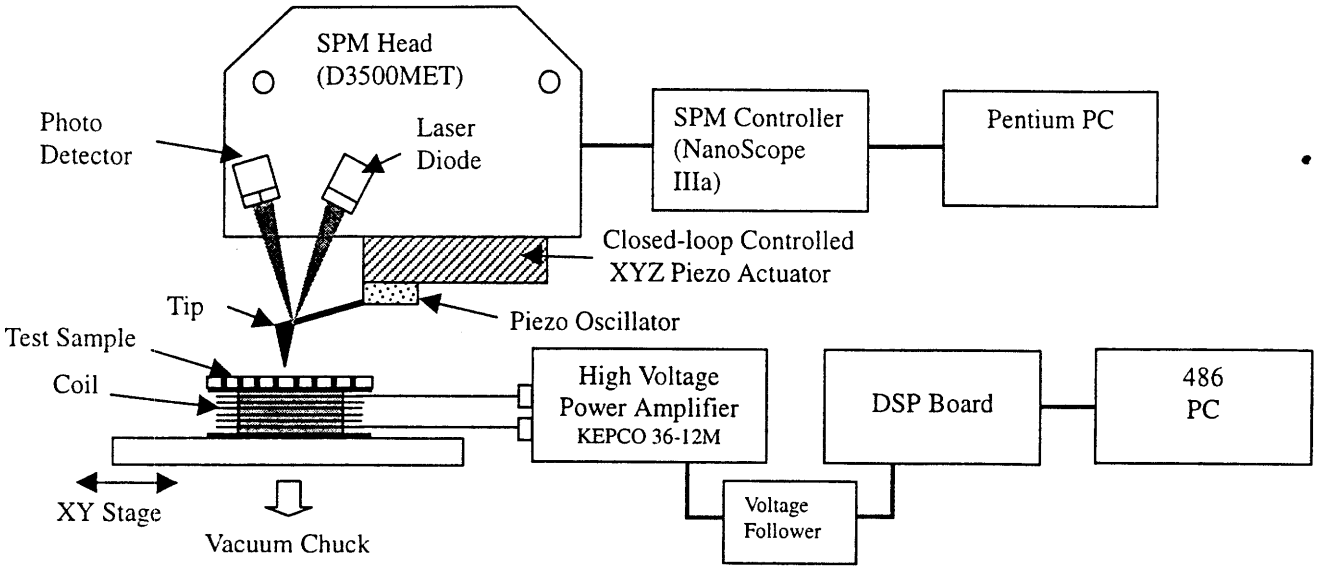

Figure 2-4 Detailed diagram of the experimental setup

In our experiments, two types of MFM probes were used, the standard probe and the low moment probe. We found that the standard probe affects the magnetization of the sample during the imaging. The stray field from these probes was strong enough to affect the states of pillars. Low moment probes were used for most of the switching field related experiments. It has a thinner magnetic coating on the tip and therefore a lower field strength. The spatial resolution of the MFM was improved since the radius of curvature of these tips is smaller[1]. However, due to a small magnetic volume on the tip, the sensitivity of the probe was reduced and consequently, the contrast of the MFM image was lowered.

A common method to realize the writhing module is to use an electromagnet. The following is the design criteria for the electromagnet to be used in our application.

---

[1] According to the manufacturer's data, the radius of curvature for the standard tip is 25–50 nm and 20-40 nm for the low moment tip.

- The range of magnetic field that can be generated from the coil should cover at least -1000 Oe $\leq H_{ext} \leq$ 1000 Oe
- The rise time of the field in response to the current step input should be shorter than a few mili-seconds.
- The coil or other experimental components located near the sample during the measurement should not interfere with MFM imaging. Non-magnetic materials are preferred for these components.
- The size of the coil should be small enough to fit inside the MFM platform. The height of the coil should be smaller than 2 cm. Maximum allowable distance between the tip and the sample stage in D3500 is about 2.5cm

The coil used in our experiments can generate a magnetic field as high as ±1000 Oe. The shortest pulse it can produce was around 3 msec. A plastic bobbin was used for the coil base instead of the common magnetic ferrite core because it had been reported that the latter type of core seriously degrades the MFM imaging. Because we used the plastic base, we needed a high current of 12 A supplied to the coil in order to meet the requirements. Producing a current pulse of 12 A with duration as short as 3msec was a difficult task because of the high inductance of the coil and the high capacitance of the amplifier circuit. Table 2.1 shows the final specifications of the coil used in our experiment. The detailed design process and the specifications of other test coils are provided in Appendix B. Note that the actual field generated from these coils was measured with a commercial gaussmeter. The measured data, input current vs. coil field, are provided also in Appendix B. As depicted in Figure 2-4, the coil was fixed between the sample and the stage and held by the vacuum chuck. This orientation enables the coil to directly apply a field vertical to the sample and, at the same time, the MFM probe to scan across the sample. The power amplifier[1] was used to produce a current pulse with amplitude ranging from –12A to 12 A.

[1] KEPCO 36-12M manufactured by KEPCO

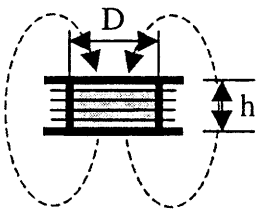

Number of Turns	150
Size(D, h)	8.6 [mm], 6 [mm]
Wire A.W.G. Size	29
Resistance of Wire	81.22 [Ω/1000 ft.]
Time Constant	68 [μsec]
Maximum Field	±1000 [Oe]

Table 2.1 Specifications of the coil

The shortest pulse the amplifier and the coil can produce has a width of 3 msec. The amplitude and the duration of the current pulses were set by the digital signal processing (DSP) board through the programming input port of the amplifier

In summary, our experimental setup consists of the coil and a commercial AFM/MFM instrument. Fields ranging from –1000 Oe to 1000 Oe can be applied vertically to the sample and the resulting magnetic state of the sample can be monitored by MFM imaging.

2.3.2 Sample Fabrication

The samples were fabricated for the study of various media properties. Two properties of most interest were the switching field and the interactions. The dimensions of the pillars were chosen so that they were within the predicted range of a single magnetic domain. Pillar arrays with 150 nm, 200nm, 250nm, 300nm, and 1,500nm in spacing were fabricated.

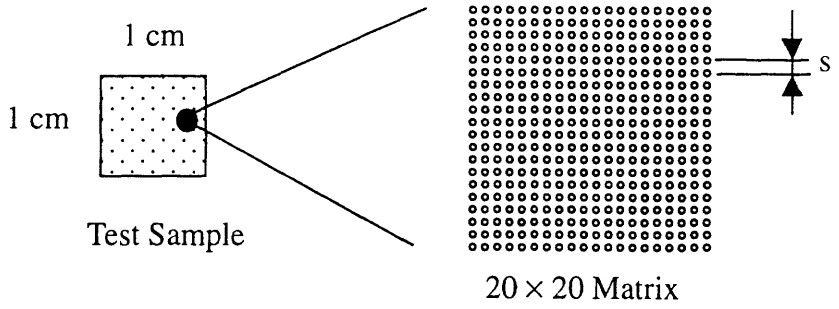

Figure 2-5 The layout of the test sample (s = 300 nm, 250 nm, 200 nm, and 150 nm for pillar arrays, s = 1,500 nm for isolated pillars)

The pillar arrays with various spacings allow the study of the interaction field as a function of the distance between the pillars. The pillar arrays with 1,500 nm in spacing were intended for the study of completely isolated magnetic particles. All the samples used in these experiments were fabricated at the Nano-Structures Laboratory in the Department of Electrical Engineering and the laboratory in the Department of Material Science at MIT[1]. The following summarizes the features of the test sample design.

- Each pillar has the aspect ratio of more than 1 and therefore it's assumed that the shape anisotropy forces the easy axis to be in the main pillar axis, vertical to the sample surface. The perpendicular patterned media were of most interest in this thesis because it theoretically allows a higher recording density than the conventional longitudinal

[1] The author credits May Farhoud, Mark Mondol, and Minha Hwang for their support on the sample fabrications.

media.

- The smallest spacing of the pillar array is 150 nm. If each pillar stores one bit of data, the array has the recording density of nearly 30 Gbits/in^2. The areal density of the hard disk drive has now passed the 10 Gbits/in^2 mark. Such rapid increase in recording density is getting very close to the superparamagnetic limit, expected to occur around the 30-50 Gbits/in^2 range.
- Both Ni and Co are used for the pillars. However, most of the experiments are performed on Ni pillars because the Co pillar arrays showed such wide variations in switching field, making it impossible to pursue further analysis.

The fabrication process included electron beam lithography and electroplating. The reason for using electroplating rather than the lift-off process was that it easily produced high aspect ratio vertical structures. The following summarizes the fabrication procedures.

1. Deposition of an electroplating seed layer

100 Å of Ti and 200 Å of Au were evaporated on to the 3″ bare silicon wafer. A conductive Au layer was used as a seed layer for the electroplating of Co and Ni.

2. Spin coating of a photoresist

The positive resist, 3% PMMA of 950 K molecular weight, was spun onto the substrate. The resulting thickness of the PMMA layer was around 250nm. Because the plating material eventually fills up the holes on PMMA template and constructs the pillars, the thickness of the PMMA layer determines the final height of the pillars. The empirical plot of a spin curve, the thickness of PMMA vs. spin speeds, was used to predict the correct speed for the target thickness.

3. Electron beam lithography

The patterns, shown in Figure 2-5, were exposed on the PMMA using an electron beam lithography technique.

4. Flood exposure.

In order to predict the plating rate, the area outside the 1 cm × 1 cm region where the test patterns were written was exposed with a flood exposure system. The area was later plated simultaneously with the test pattern. The plating rate inside the test pattern, then, was estimated based on the known area outside the pattern, The whole wafer with test structures covered with a piece of aluminum was exposed to the UV light for about 15 minutes.

5. Develop

The exposed PMMA was developed in MiBK:IPL=2:1 solution for 45 seconds.

6. Reactive Ion Etching (RIE)

By using the RIE, the remaining PMMA and other possible contaminants on the surface of the plating layer were removed.

7. Electroplating

Ni was deposited from sulfamate electrolyte with a plating temperature at 50°C. The solution contained 327 g/l of anhydrous nickel sulfamate, 30 g/l of boric acid, 3 g/l of a properietary anode corrosion aid and 0.3% by volume of wetting agent. Boric acid was used to adjust the pH to 3.6. Co was deposited from either a sulfate or a sulfamate electrolyte. The sulfate solution contained 200 g/l Co sulfate, 30 g/l cobalt chloride and 30 g/l boric acid with pH of 3.5. The sulfamate solution contained 75 g/l cobalt and 45 g/l boric acid, and the pH was in the range of 3.5 to 4.5. The plating rate was controlled by the plating current density, ranging from 1 to 11 mA/cm^2, but was very sensitive to the conditions of the plating solution. Refer to [30] for further details.

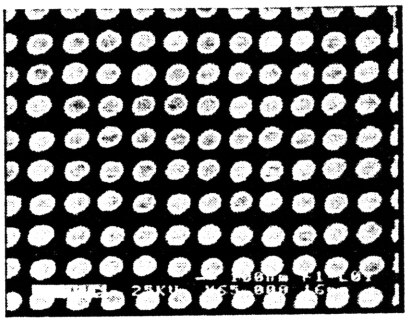

(a) 150 nm Pillar Array

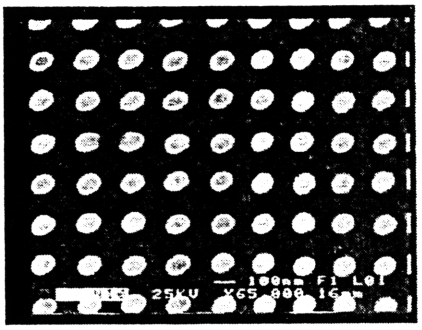

(b) 200 nm Pillar Array

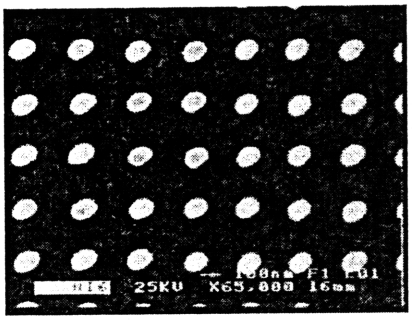

(c) 250 nm Pillar Array

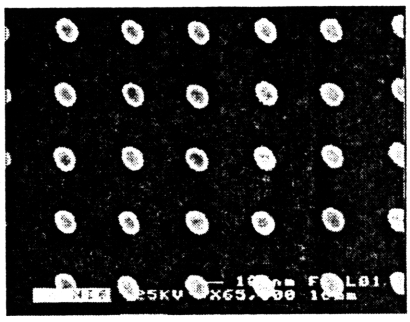

(d) 300 nm Pillar Array

Figure 2-6 SEM image of the Ni pillar arrays

8. Inspections

The PMMA template was removed in the acetone bath to leave the pillar array, ready for the inspection. The resulting test patterns were observed with the scanning electron microscope (SEM).

The SEM images for the Ni pillar arrays with 150 nm, 200 nm, and 300 nm in spacing are shown in Figure 2-6. The average diameter of the pillars in these arrays was 90 nm. The diameter was measured based on the known spacing between the pillars. The height of the pillars was measured with AFM. The height ranged from 130 nm to 200 nm for the samples plated at different conditions. It was known that the height of the pillar depends on the plating time, input current density, temperature, etc, but the accurate prediction of the plating rate was difficult, probably due to some unknown plating

parameters. The shape of the pillars in Figure 2-6 (d) indicates that the electron beam is not perfectly stigmatized. This, however, is not significant enough to induce the shape anisotropy in such a direction.

In summary, the electron beam lithography and electroplating were used to fabricate the arrays of Ni pillars having a diameter of 90 nm, a height of 120 nm – 200 nm and spacing of 150 nm – 300 nm. The electron beam lithography system provides a flexible and easy way to make small structures, but its inherent scanning method results in slow throughput. A different approach using the interferometric lithography is currently developed at the Nano-Structure Laboratory as a mass production technology of the patterned media [30][31].

2.3.3 Experimental Procedures

The switching field of the pillars was measured following the procedures described below.

1. Initial magnetization of the sample and the MFM tip

First, the sample was placed at the center of the coil shown in Figure 2-4 and secured with a vacuum. A visible mark was made on the sample to indicate the location of the patterns. First, the sample was magnetized along the pillar axis under a field of 3000 Oe. The MFM tip, fixed in the microscope, was magnetized along the direction opposite to that of the pillars. The magnetization direction of the tip is in the same direction as the coil field, applied to the sample in step 3. This is to prevent the magnetization of the tip from changing as the increasing coil field is applied.

2. Initial topography and magnetic imaging

First, the sample was scanned in tapping mode and the location of the test patterns was found. Here, the 13×13 array of pillars in each array were scanned. Next, the MFM images

of the same pillars were taken in Lift mode[1] with a scan rate of 0.8 [number of scanned lines/sec]. In the MFM image, a black circle with a white band around on the location of a pillar indicates that the tip and the pillar are in an attractive mode. A white circle with black band around indicates that those are in a repulsive mode. A sudden reversal of the color indicates that the magnetic polarity of the pillar has flipped. The ideal MFM images of the single domain particle in various magnetization states of the tip and the particle can be found in [24][25]. From the resulting images, we examined the MFM image of the pillars to verify that the stray field from the tip didn't affect the state of the pillars during the scan. Those pillars that have changed the polarity were excluded from this experiment.

3. Measurement of switching field

A known field was applied to the pillars along its long axis and increased from 0 Oe to 1000 Oe with increments of 30 Oe. At each increment, an MFM image of the pillars and the number of pillars with the switched polarity was recorded. The field is applied in the form of a pulse with duration as short as 3 msec[2] to prevent the coil from being heated. The variation of the ambient temperature may have effect on the switching field.

2.3.4 Single Magnetic Domain

Before the switching properties of the pillars are discussed, it should be verified that the pillars under study are single magnetic domains. In the following section, the critical size of the single domain for each material that forms the pillar is calculated. The next section

---

[1] Lift mode is the MFM imaging technique patented by Digital Instruments. After the topography scan, the tip is lifted up to the height where a long range magnetic force is dominant. The tip follows the topography of the sample while the magnetic force is measured by detecting a phase change of the cantilever oscillation.

[2] The measured switching field depends on the time the field is applied to the pillar.

discusses an experimental approach to determine whether the pillars are single magnetic domains.

2.3.4.1 Critical Size

The critical size can be calculated by equating the effects of the two dominant energies in a domain formation, namely the magnetostatic energy and the exchange energy [38]. For a particle smaller than the critical size, exchange interactions become more important than magnetostatic effects and consequently the particles tend to remain uniformly magnetized. However, if a particle is larger than the critical size, the magnetostatic effect is dominant and thus the particle spontaneously breaks up into a number of domains in order to reduce the large magnetostatic energy it would have if it were a single domain. The equation for the critical size of prolate spheroids is given by

$$a_{co} = qC^{1/2} / M_s \tag{2.3}$$

Constant q is a geometry constant that can be found from the graph given by Aharoni for a given aspect ratio of the pillar [38]. M_s is the saturation magnetization and C is the exchange constant. The critical size, a_{co}, is actually the lower bound, as defined by Brown, under which the pillars are always single domain [54]. Using the above equation, we found that a Ni pillar with an aspect ratio of 2 has a critical diameter of 50 nm. Ms of 484 emu/cm^3 and C of 7.7×10^{-7} were used in the calculation. The exchange constant, C, is actually the least known in the equation and expected to cause errors in the calculations. We used the equation given in [2] as described in Section 2.4 to calculate this constant. Also, in the calculation, we ignored the effect of a slight variation in shape because it's shown that the existence of some variation in geometry does not affect the relevant energies significantly [38]. The diameter of Ni pillars in the test structure is actually larger than the

calculated critical size, leaving possibility that the pillars are not single domains.

2.3.4.2 Experimental Results

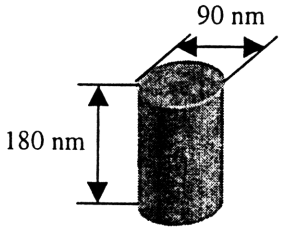

Figure 2-7 The dimension of the pillar

The Ni pillars have a cylindrical shape, shown in Figure 2-7 and their average diameter was 90 nm and the height was 180 nm. To determine whether the pillar is a single magnetic domain, we tried to find evidences in MFM images. It's actually difficult to obtain quantitative information from these MFM images, but we concluded that the pillar is a single domain or in almost single domain state from the following two facts. First, the MFM image of the pillars resembles the ideal MFM image of the single domain pillar taken with the same orientation of tip and pillar magnetizations. The ideal magnetic image of a pillar has a bright spot at the center and a dark band around it or its reversed pattern. Figure 2-8 (b) and (c) are the experimental MFM images of the pillars, clearly resembling the two ideal images. Secondly, under the changing field, the remanent magnetization state of the pillars is always in one of two equivalent but opposite polarity states. To show this behavior, a plot similar to the hysteresis loop is drawn based on MFM measurements. In Figure 2-8 (a), the horizontal axis represents the applied field and the vertical axis represents a normalized phase obtained from the MFM data. The phase is not an absolute value of the magnetization of the pillar but it can be considered as a value proportional to it. The plot resembles in shape the ideal hysteresis loop of a single domain particle. In the plot, it can be seen that at each corner there exists a sudden switch of magnetization states. In other parts of the plot, there is no change of states regardless of the input field. Figure 2-8 (b) shows the MFM

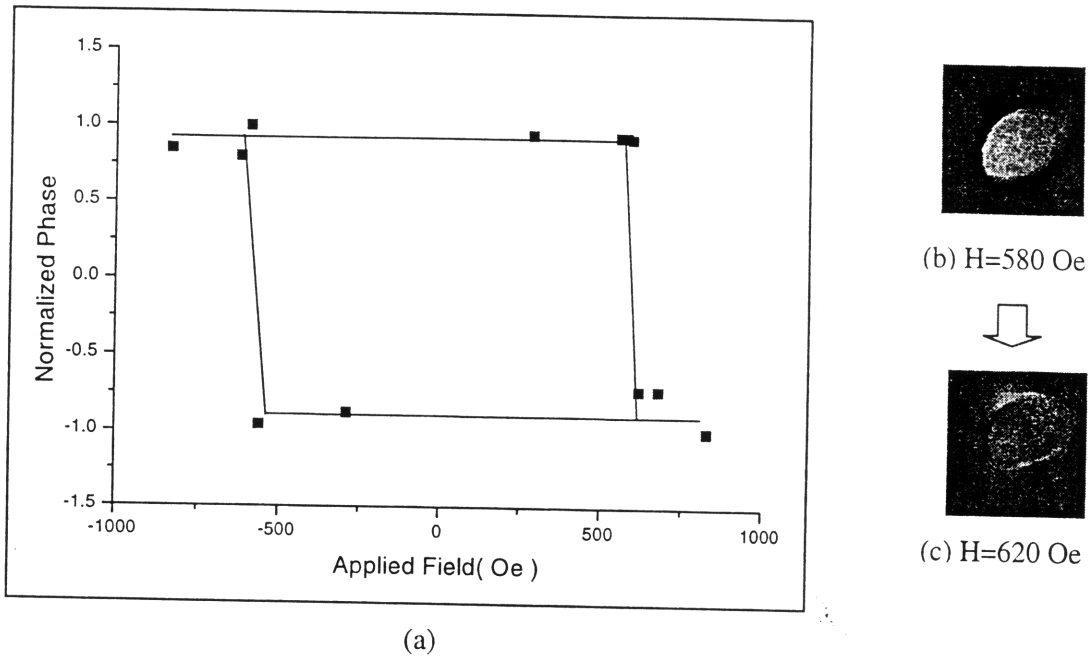

Figure 2-8 (a) Experimental hysteresis loop of a single Ni pillar (90 nm × 180 nm) (b) MFM image at H = 580 Oe (c) MFM image at H = 620 Oe

image of the pillar at an input field of 580 Oe while Figure 2-8 (c) shows the image of the same pillar after the field of 620 Oe is applied. With a small increment of 40 Oe, the magnetic image of the pillar is completely reversed. These behaviors exactly match those of single domain particles.

2.3.5 Results

The switching fields of the Ni pillars were measured following the procedure described in Section 2.3.3. The pillars in the 13 × 13 matrix of 300 nm period array were observed under an increasing external field. It is assumed that the effect of the interaction field is very small. Figure 2-9 shows the accumulative fraction of switched pillars at each given external

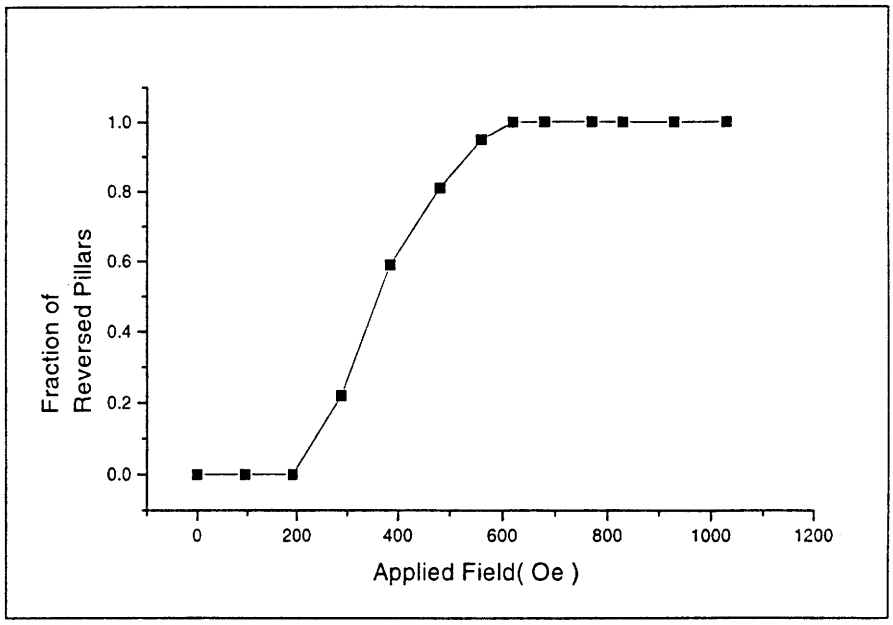

Figure 2-9 Switching field distributions of 300 nm Ni pillar array

field. In the figure, the horizontal axis represents the external field, ranging from 1 Oe to 1000 Oe, applied to the pillars, and the vertical axis represents the fraction of the switched pillars in 13 x 13 pillar array. The fraction is 0 if none of the pillars are flipped and 1 if all pillars in the matrix are flipped. Ideally, for the pillars with identical geometry, the curve should rise vertically from 0 to 1 at some given external field. However, the experimental curve shows that it gradually increases from 0 at 200 Oe to 1 at 700 Oe. This means that the switching fields of the pillars are distributed evenly between 200 Oe and 700 Oe. The average switching field of the pillars was 420 Oe. The average, H_{avg}, was computed from the equation given by

$$H_{avg} = \frac{1}{N}\sum_{i=1}^{N} H_i \tag{2.4}$$

where H_i was the switching field of i-th pillar and N was the total number of pillars, The standard deviation was around 100 Oe. Such wide variations of the switching field were

against our expectations because we observed no significant deviations in dimensions from pillar to pillar. The difference between the heights of the pillar was ± 10 nm. Furthermore, it was found that there were no correlation between the height of the pillar and the switching field. The issues related to the switching field variations are further discussed in Section 2.5. In the following, several factors that may have effect on the measurement results are presented.

- Because a field strength of the coil depends on the position with respect to the coil's center, the pillar array has to be precisely positioned at the top center of the coil. In the experiments, the sample was aligned manually. Such a procedure may have caused an error in estimating the actual field applied to the pillar. For example, if the sample is off the coil center by 2 mm, the error is about 7% of the predicted field from the coil.
- It was observed that the repeated supply of high currents heated up the coil significantly. This may have an effect on the switching behavior of the pillars.
- Magnetic objects near the sample such as the MFM tip, the SPM head, and the sample holder can interfere during the field application to the pillars.
- For some pillars, their MFM image did not show either pattern of the saturation states. It is possible that those pillars are not the single domains. If a pillar consists of multi-domains, it will exhibit a switching behavior, different from that of single domain pillars. The MFM image taken at each increment of external field will show a gradual change before a complete reversal of the state. Such behavior of multi domain pillars is difficult to distinguish from the effect of the measurement noise.

However, none of the factors above can sufficiently explain such wide variations of switching fields in our pillar array. In fact, the repeatability from one measurement to another was in good agreement. In two consecutive switching field measurements performed on the same array, consisting of 160 pillars, 98% of the data were in agreement.

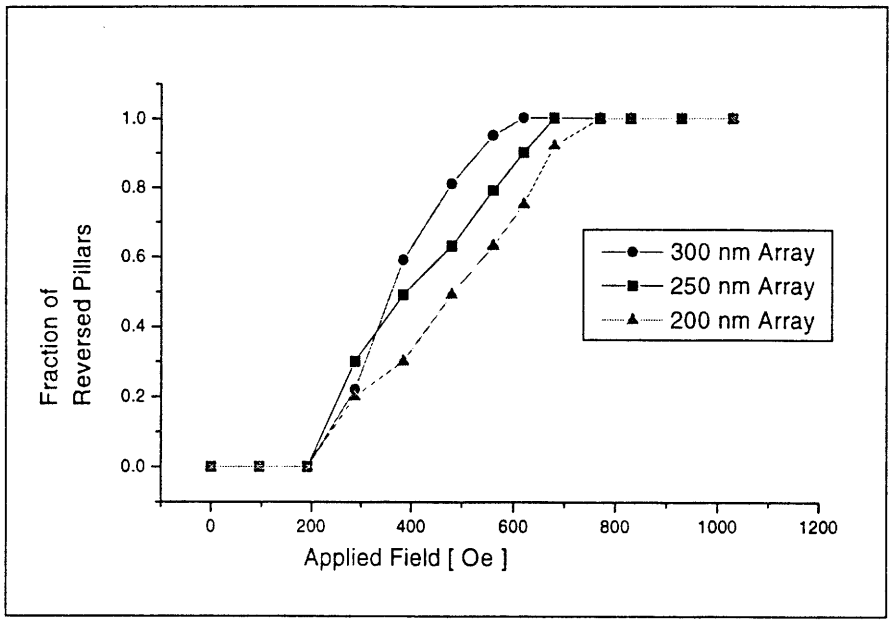

Figure 2-10 Switching field distribution of 300 nm, 250 nm, and 200 nm period arrays

Figure 2-10 shows the switching field distribution of the pillars in 300 nm, 250 nm, and 200 nm period arrays. It is already seen that those pillars in the arrays have the same geometry and dimensions. The figure shows that the switching field variations become wider as the spacing is decreased. This indicates that the field interactions between pillars affect the result of the switching field measurements, as it is known that the interaction becomes stronger as distance between the pillars is decreased. Further detailed discussions on interaction fields are provided in Chapter 4.

Figure 2-11 shows the switching field distributions of the two arrays that have the same spacing but different pillar aspect ratio. One has an average pillar height of 185 nm and the other has 130 nm. Since the diameters of the pillars in both arrays are 90 nm, the aspect ratios are 2 and 1.4 respectively. The pillars with aspect ratio of 1.4 have an average switching field of 520 Oe and the pillars with aspect ratio of 2 have 460 Oe.

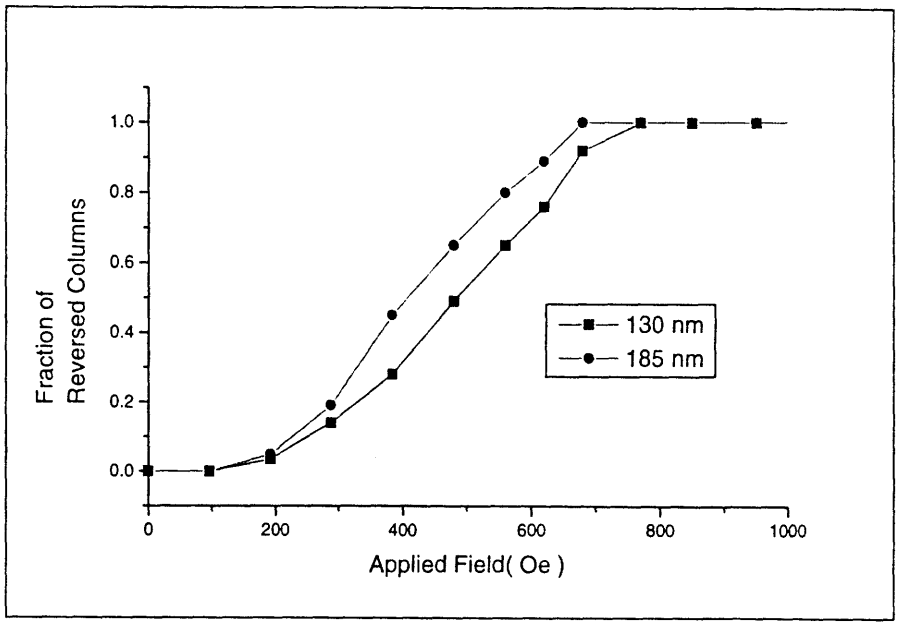

Figure 2-11 The switching field distributions of the arrays with different pillar heights

The relationship between the switching field and the shape of the particle is of much interest to the researchers in this field. Such a relationship can be used to engineer the properties of the magnetic media. Figure 2-11, however, indicates that such dependency is small for these pillars. The switching field decreases only slightly as the aspect ratio increases from 1.4 to 2. In fact, the difference is smaller than the standard deviation of the switching field variations.

2.4 Switching Mode

In this section, the investigations on the magnetization switching process of the single domain pillars were conducted by taking theoretical approach. Two classical switching

modes, coherent rotation or the Stoner-Wohlfarth mode and curling mode, were investigated. The switching process of the recording media was often studied by micromagnetic simulation in theoretical research. [55-59] In the simulation, the grain is the most fundamental element. The main assumptions of the simulation are that each magnetic grain is always uniformly magnetized such that, during the magnetization process, only its magnetization direction is changing. With this assumption, a magnetic object is considered as an assembly of interactive magnetic grains with inclusion of both long range magnetostatic interaction and nearest neighbor intergranular exchange coupling. The magnetization directions of the grains during a magnetization process are determined by solving coupled Landau-Liftshitz equations. In the simulation, crystal anisotropy easy axis of each grain can be oriented in any desired direction. Gadbois et al. performed the micromagnetic simulation on nano-scale Ni bars [40]. It was found that a magnetization switching process in these bars can be characterized by the formation of magnetization vortices at the beginning of the reversal, followed by vortex motion and the expansion of reversed regions, and ending with annihilations to the magnetization vortices.

For the pillars in Figure 2-7, the same simulation can be performed to determine the magnetization process and the switching properties. However, because the pillars have a very simple geometry, being close to the prolate spheroid and the size is considerably smaller than those Ni bars studied in ref [40], the classical switching model may well predict the switching behavior of the pillars.

2.4.1 Coherent Reversing Mechanism

The coherent mode assumes that the spins of all atoms in the particle remained parallel to one another during the rotation [32]. If the switching process is solely governed by the effect of the crystal anisotropy, the intrinsic coercivity of a particle, H_e is given by

$$H_c = 2K_1/M_s \tag{2.5}$$

The term, intrinsic coercivity, is defined as the external field that decreases the magnetization of the particle to zero. For a single domain particle, the intrinsic coercivity is the same as the switching field. In the equation, it is assumed that the external field is aligned with the easy axis and the effect of K_2 is small. According to the equation, the switching field, H_{swf}, of Ni pillars was as much as 185 Oe, where K_1 is -4.5×10^4 erg/cm^3 and M_s is 484 Oe[1]. However, electroplated Ni pillars are usually not a single crystal as assumed in this equation. This was evident in the X-ray diffraction measurements, which showed the easy axis, <111> direction for fcc structure, was not well defined. It was assumed in the following discussions that the effect of the crystal anisotropy was negligible in the switching process and only the shape anisotropy was considered.

When the shape anisotropy is dominant in the coherent rotation process, the switching field of the elongated magnetic particle is given by

$$H_{swf} = (N_a - N_c)M_s \tag{2.6}$$

where N_a is the demagnetizing factor along the short axis of the particle and N_c is along the long axis. Using Eq. (2.6), the switching field of the Ni pillar showed in Figure 2-7 was calculated. The resulting switching field was 1458 Oe. Here, N_a was 5.1927 and N_c was 2.1811.

The switching field calculated from Eq. (2.6) differs from the experimental value. In Section 2.3.5, the average switching field from the measurement was 420 Oe. This hints that the Ni pillars do not exactly follow the mechanism of coherent rotation.

The critical size below which the coherent rotation is favored can be calculated by

[1] Note, however, that M_s value can be different for number of cases. The 20-30% change of M_s was observed in the electroplated Ni pillar array.

using

$$D = 1.04 \times D_0 \tag{2.7}$$

where D_0 is the fundamental unit of length used in the calculation of exchange energy effect [2]. The definition and the calculation of D_0 are provided in the next section. The equation is obtained by equating the contribution of the magnetostatic energy and the exchange energy to the switching process. The exchange energy is the origin of the curling mode. If a particle is larger than the critical size, it will favor the curling mode. For Ni pillars, the critical diameter is calculated to be 46 nm, which is smaller than the actual diameter of the pillar in Figure 2-7. This confirms that the coherent mode is not the pillars' main rotation mechanism.

2.4.2 Curling Mode

Curling mode, studied by Frei et al. [33], assumes that the spins are always parallel to the surface during a curling reversal. As a result, no free poles are formed and, therefore, no magnetostatic energy is involved. The energy barrier to a curling reversal is then entirely the exchange energy, because the spins are not all parallel to one another during the reversal. In contrast, the coherent rotation produces free poles on the surface, and therefore, the magnetostatic energy plays a major role, excluding the effect of exchange energy. The equation of the pillar's switching field for the curling mode is given by

$$H_{ci} \geq N_c M_s - 2\pi M_s k/(2a/D_0)^2 \tag{2.8}$$

where k is the constant dependent on the aspect ratio given in ref. [54] and a is the semi-minor axis. D_0 is the characteristic length defined by the following equation,

$$D_0 = \frac{2A^{1/2}}{M_s} \tag{2.9}$$

where A is the exchange constant. In fact, the exchange constant, A, is the most uncertain parameter in calculations of switching fields. Here, we followed the derivation suggested in [2]. The exchange constant for Nickel, having an fcc structure can be represented as

$$A = \frac{4J_{ex}S^2}{a} \tag{2.10}$$

where S is the spin number, J_{ex} is the exchange integral, and a is the lattice number. For the pure spin of Ni atoms, J_{ex} is given by

$$J_{ex} = \frac{3K\theta}{2zs(s+1)} \tag{2.11}$$

where K is the Boltzman's constant, θ is the Curie temperature, and z is the coordination number of a crystal structure or the number of nearest neighbor atoms in the crystal lattice. Using Eqs. (2.9) – (2.11) and the material constants for Nickel given in Table 2.2, we can calculate Eq. (2.8) for Ni pillars. The result was

$$H_{swf} \geq 410 \text{ Oe} \tag{2.12}$$

The inequality sign in Eq. (2.12) means that the switching field is expected to be larger than 410 Oe. The switching field of the pillar, however, should be smaller than that of the infinite cylinder, for which the equation is given as

$$H_{swf} = 2\pi M_s \times 1.08/(2a/D_0)^2 \tag{2.13}$$

By using the values already obtained, Eq. (2.13) is calculated. The final solution for H_{swf} of Ni pillar was

$$410 \text{ Oe} \leq H_{swf} \leq 535 \text{ Oe} \tag{2.14}$$

The experimental data of the switching field, 420 Oe, is within the above range. The curling mode also suggests that the switching field of the pillar increases only slightly with higher aspect ratios of the pillar[1]. Eq. (2.14) indicates that the switching field of the pillar is some value between 410 Oe and 535 Oe and increases monotonically to 535 Oe as the aspect ratio of the pillar increases to infinity. This suggests that the increase of the aspect ratio from 1.4 to 3 as seen in the experiment, explained in Section 2.3.5, should not result in the visible change of the switching field. Such behavior, predicted by the curling mode, agrees well with the experimental results. The results indicate that the main reversing mechanism of the pillars is the curling mode.

Constant	Value	Constant	Value
K (Aharoni's constant) for the aspect ratio of 2	1.3	K (Boltzman Constant)	1.38×10^{-16} [erg/°K]
M_s (Saturation Magnetization)	484 [emu/cm^3]	θ (Currie Temperature)	658 [°K]
a (Lattice Number)	3.452×10^{-8}[cm]	z (Coordination number of crystal structure)	12
S (Spin Quantum Number)	1.5	a (semi-minor axis)	90 [nm]

Table 2.2 Physical constants used in the calculation of switching fields of the Nickel pillar

For Ni pillars, having a diameter smaller than the critical diameter, 46 nm, we may expect the coherent rotation mode to occur. The coherent rotation of the pillars is actually preferred in media applications, because the switching field is higher and it's possible to engineer the media properties easily by changing the aspect ratio of the pillars.

---

[1] Note that in coherent mode, the switching field increases dramatically with higher aspect ratios.

2.5 Switching Field Variations

Figure 2-12 shows the distributions of the switching fields of the Nickel pillars with nearly identical size, 90 nm in diameter and 180 nm in height. In the plot, the number of switched pillars was recorded at each increment of the external field along the direction of the pillar axis, perpendicular to the sample plane. The plot clearly shows that the switching fields of the pillars are distributed over a wide range, expanding nearly 500 Oe. Such irregularity of the switching fields may present serious limitations in recording applications. Figure 2-13 shows the diagram of the pillar array, observed in previous sections, with each pillar colored in a gray scale, representing the strength of the switching field of the pillar. The darker color represents the higher switching field and the brighter color indicates the lower switching field. The corresponding switching field range of each color is also shown in the diagram. Missing circles in the pillar array represent the pillars for which we couldn't

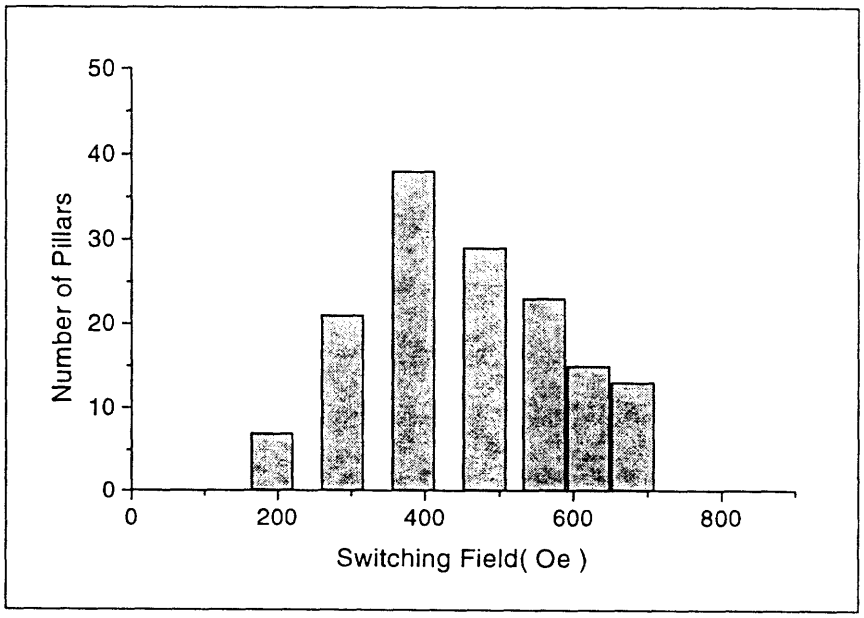

Figure 2-12 Switching field distribution of Ni pillars with identical size (90 nm × 180 nm), measured from 300 nm array

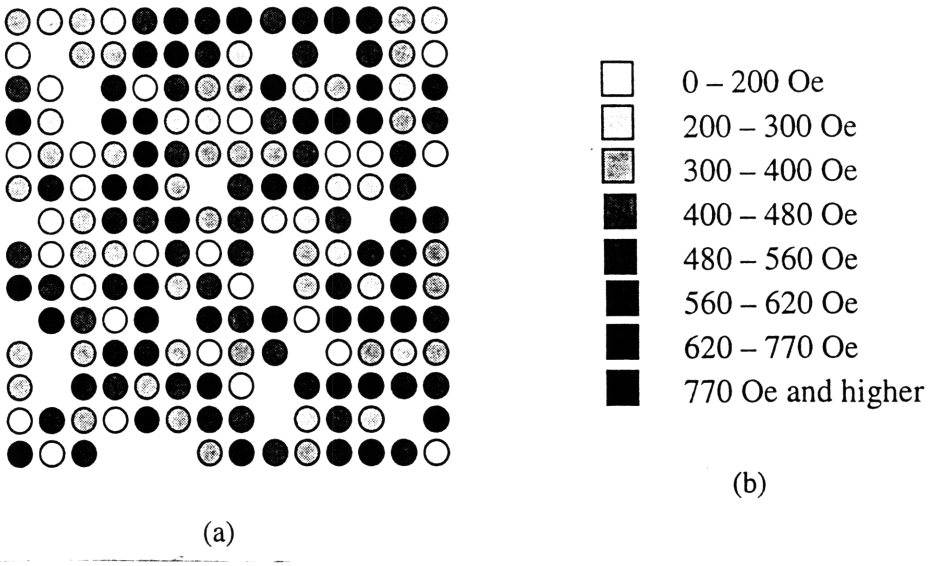

Figure 2-13 Switching field distributions (a) 300 nm pillar array (b) table for (color – switching field range)

determine the switching field due to the poor MFM image quality. An apparent indication of this figure is that the switching field of the pillars distributed randomly regardless of the pillar locations. A variation of the switching field as high as 500 Oe was observed in the pair of nearest pillars. This indicates that the variations are caused by the factors that are present in a very small scale, comparable to the pillar size.

An important contributing factor is the magnetic interactions between pillars. It is known in theory that the perpendicular recording media has higher interactions due to its vertical orientation of bits. If the strength of the interaction field felt by a pillar is comparable to that of the inherent switching field of the pillar, the switching field, experimentally obtained, will dependent on the states of the pillars near it and thus the variations will occur. This was evident in Figure 2-10 where the variation width depended on the distance between the pillars. The standard deviation of the switching field distribution was 100 Oe for 300 nm period array and increased to 142 Oe and 182 Oe for

250 nm and 200 nm period array respectively. This shows that interaction field contributes to the switching field variations to some degree. Chapter 4 presents a detailed analysis of the interaction fields between single domain pillars, performed by taking both the theoretical and experimental approaches. According to the analysis, the interaction field can vary the switching field of a pillar as much as 100 Oe for a spacing of 300 nm. This, however, is lower than the variation width observed in Figure 2-12.

The microstructure of the pillars can also cause the variations of the switching field. One important factor related to the microstructure is the number of grains inside the pillar. As a pillar becomes smaller in size, it contains fewer numbers of grains and there is less chance that the magnetocrystalline anisotropy of the grains averages out completely[1]. This may cause the pillars to have unpredictable net easy axes of magnetization and reversal characteristics. Such an aspect was studied by New et al., who performed calculations on single domain polycrystalline Cobalt bars of 200 nm × 100 nm × 20 nm in size and their grain of 10 nm in radius [20]. They showed that for such particles the randomly oriented magnetocrystalline anisotropy may dominate over shape anisotropy, leading to wide switching field variations. For Ni particles, the magnetocrystalline anisotropy constant is much smaller than that of Co. Therefore we can expect that the effect of crystal anisotropy is reduced and therefore the switching field variations are narrower in Ni pillar array. Also, it was observed that the micro-structures of electroplated Ni films were relatively finer than that of Co film. Larger number of grains in the pillar can also reduce the variation further. Indeed, it was found experimentally that the switching field variations of Co pillars were

[1] The most fundamental unit of the microstructure of the single domain polycrystalline magnetic particles is the grains. It is usually assumed that each grain has uniaxial crystalline anisotropy with easy axis oriented in random direction. If we assume that the crystals have a preferred orientation, called texture, then the particles will have a resultant anisotropy dictated by that of the individual crystals.

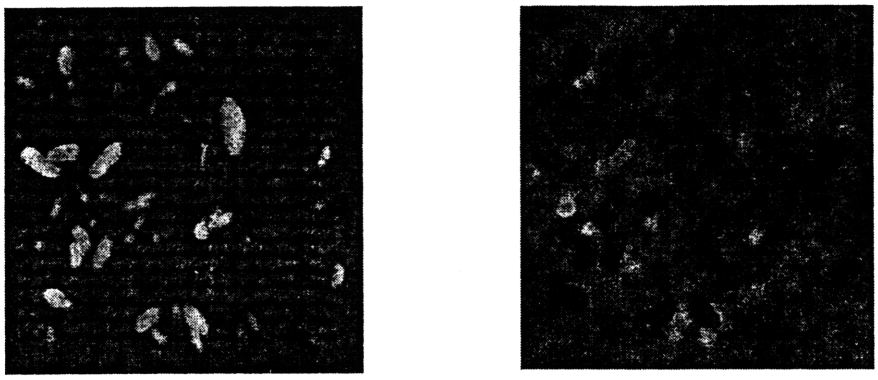

(a) Topography Image (AFM) (b) Magnetic Image (MFM)

Figure 2-14 Large crystals in Co pillar array with 200 nm spacing

much wider than those of Ni pillars.

Another factor related to wide switching field variations is the effect of various possible edge domain configurations at a saturation state. Such effect was studied in depth by J.G.Zhu et al. [40][60-61]. According to their micromagnetic simulations on a Ni bar, 1 μm in length, 30 nm in depth, and ranged from 40 nm to 400 nm in width, an edge roughness, 5 nm in amplitude, causes a variation in the switching field of the bar as much as 40%. It is shown that the magnetization vortices appear near these rough edges and propagate to the alternate upper or lower bar end. This propagation, not seen in smooth edge bars, facilitates the switching process. Their study also showed that the non-elliptical shape at the end of the bar has non-uniform end domains that can have significant impact on the switching process. Y. Zheng et al. compared two different end domain configurations in Co bars with aspect ratio of 2 and showed that the switching field varies nearly 16% [61]. The Co and Ni pillars in our test sample are observed to have randomly oriented sharp edged on the top, which may form well-defined end domains. Also, on top of the pillar arrays, randomly located large crystals were observed. These are shown in Figure 2-14. In

the figure, (a) is the AFM topography image of the Co pillar array and (b) is the MFM image of the same area. The magnetic patterns near the crystals indicate that these are magnetic in nature. It is likely that these large crystals have grown from the irregular edges on top of pillars.

In conclusion, to reduce the switching field variations, the following two suggestions should be considered. First, the aspect ratio of the pillars should be increased more to impart more shape anisotropy and reduce the effect of the magnetocrystalline anisotropy. This method becomes more effective if the pillar rotates in coherent switching mode. Second, the size of the grains inside the pillars should be reduced as much as possible. This will help averaging out the effect of magnetocrystalline anisotropy and also to smooth out rough edges of the pillars. Another approach to eliminating the crystal anisotropy in the pillar is to use amorphous materials like CoP.

2.6 Summary

In this chapter, switching properties of the single domain Ni pillars were studied. Ni pillars were fabricated by electroplating into the PMMA template. The electron beam lithography technique was used to produce 150 nm, 200 nm, and 300 nm array patterns. By performing MFM analysis, we observed that the cylindrical Ni pillars, 90 nm in diameter and 180 nm in height, behave closely as a single magnetic domain and reverse their magnetization at an average field of 400 Oe. Such data agreed well with curling mode rotation theory among other classical switching modes. The experiment performed on the pillars with identical size and shape showed wide variations in switching fields. A uniform switching field may be achieved by reducing the size of the grains inside the pillars and smoothing the surface of the pillars.

Chapter 3

Writing/Reading with Magnetic Force Microscopy

3.1 Introduction

Previous chapters introduced the concept of the patterned media consisting of single domain magnetic pillars and discussed their potential to become the high density recording media. The perpendicular patterned media with a recording density ranging from 7Gbit/in^2 to 30 Gbit /in^2 were fabricated. In this chapter, a possible read/write scheme for such patterned media is proposed and demonstrated. This scheme uses magnetic force microscopy and an *in situ* electromagnet. Writing on the perpendicular patterned media with a recording density as high as 16 Gbits/in^2 was demonstrated. The writing on the media with higher density wasn't possible due to the actively interacting pillars in those densities. However, this scheme can be still used in recording of much higher density if the size of pillars is small enough to eliminate any interactions between themselves.

Section 3.2 reviews the previous literatures on high density magnetic writing. In Section 3.3, the basic concept of the writing scheme used in this work is given. Section 3.4 presents the experimental demonstration of writing on the patterned media with a pillar to pillar spacing ranging from 200 nm to 300 nm. Also, this section introduces a useful scheme that measures the strength of an actual field applied to the pillar during the writing process. The scheme was extensively used in the interaction field measurements, presented in Chapter 4. The following section describes the procedures of the magnetic field simulations on the writing process described in section 3.3. The results were compared with

the experimental data, obtained in section 3.4.

3.2 Background

Many attempts have been made to write bits on magnetic media in ultra-high recording density. A recording demonstration of 11 Gbits /in^2 using a conventional hard disk drive (HDD) was reported recently by IBM. There were many other works in which the writing methods other than that of HDD was used to achieve high recording density. The most popular method is to use magnetic force microscopy, known for its ultra-high resolution. The writing with MFM was demonstrated in the pioneering work of Moreland et al. [62]. In this work, a triangular shaped iron foil, 5μm thick, attached to a permanent magnet, was used to change the local magnetization of a hard disk. A constant distance between the tip and the sample surface was maintained simultaneously by using the same tip in scanning tunneling microscope (STM) mode. A resolution of about 20 nm was achieved with this method. Ohkubo et al. [63-67] and Manalis et al. [68] explored the point magnetic recording (PMR) scheme. This scheme uses a sharp MFM tip and an electromagnet to concentrate a field that enables recording of small size bits. They have used this technique to write bits as small as 150 nm on the perpendicular thin film media. Writing demonstrations on the patterned media were performed. Kong et al. performed writing on the array of longitudinal bars with a recording density up to 7.5Gbit/in^2 [19]. In their work, an MFM tip thickly coated with Co, called a "write tip" was positioned near a bar end which was initially magnetized in the direction opposite to that of the write tip to switch the polarity of the bars. Then, an MFM tip with thinner coating, called a "read tip," was used to image the state of the bats without flipping the polarity of the bars. However, as the author also pointed out, this method uses just a stray field from the write tip so that the resulting writing field cannot be defined sharply, causing limitations in achieving higher recording

densities. The method also required the replacement of the tip when switching between reading and writing. The recording head consisting of separate read/write tips should be proposed if this method is to be implemented in real systems.

Other works of actively controlling the magnetic state of the bits were suggested. Watanuki et al. used an STM tip consisting of a magnetic amorphous wire wound with a coil as a writing head [69]. They have recorded a dot pattern of diameter 800 nm to 1000 nm in perpendicular double–layer media. By reversing the field from the coil, they were also able to erase the recorded patterns. Among these methods, PMR method is simple in design and allows a well-defined writing field both in shape and strength. Currently the smallest size of recorded bits has been reported with this technique.

3.3 Concept

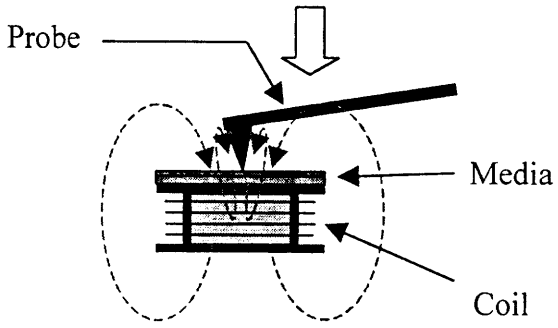

Figure 3-1 Scheme of writing with magnetic force microscope

The writing method used in this chapter resembles that of the point magnetic recording scheme. Figure 3-1 shows the basic scheme of the PMR. During this process, first, an MFM tip with nanometer scale sharpness is brought into contact with a targeted bit spot on the sample. A tip with a radius of curvature around 25-50 nm can contact the surface very lightly so that the actual contact area is extremely small. While the tip is in contact, a field

is applied to both the tip and the sample from the coil underneath, as shown in Figure 3-1. Here, the coil is used as an auxiliary pole used in perpendicular magnetic recording scheme. The purpose of an auxiliary pole in perpendicular recording is to modify the writing field from the read/write head and intensify it towards the perpendicular direction. This supports the writing in perpendicular direction. Because the MFM probe is extremely sharp, a very sharp concentrated field can be formed near the tip end with a coil field, taking a role as an auxiliary pole. Such a field is able to magnetize a small area on the media. The most important factor that determines the resolution of such writing method is the properties of the MFM tip. The tip is required to have a small radius of curvature and yet produce a uniform and well-focused magnetic field with enough field strength to magnetize bits and generate high contrast images.

The coil is an active element in the PMR writing process. First, the coil field programmable by input current controls the strength of the writing field. As the coil field is increased, the field near the tip is increased as well. However, the field outside the tip also increases to a limit where the bits other than the target bit can be affected by it. The coil can be considered just as a small pick up coil in read/write head used in a commercial hard disk. Secondly, the coil changes the direction of the writing field. When performed with the MFM tip that has a low coercivity, the tip is always magnetized along the direction of the coil field and therefore the same writing field is generated in both directions.

The small bits were written on the perpendicular patterned media using this scheme. An MFM tip was chosen so that the tip field is not strong enough to change the pillar's magnetization. A range of tip fields can be obtained by coating the tip with different thicknesses. The writing was performed by contacting the tip on top center of target pillar and applying a field from the coil in the direction opposite to the pillar magnetization. Here, the coil field was not increased up to a limit that influenced the states of all other pillars in the sample. Only the concentrated field applied to the selected pillar should be higher

than the switching field of the pillar. Using the right combination of an MFM tip and coil field was important in this writing technique.

3.4 Writing Experiments

3.4.1 Experimental Setup and Procedures

For the writing experiments, the same setup shown in Figure 2-4 was used but the procedure was different. The setup includes the coil and a commercial AFM/MFM, D3500 from Digital Instruments. The coil was attached under the sample to apply a field vertical to the sample plane. The coil was fixed firmly by a vacuum chuck of D3500 together with the sample on top of the coil. It was verified that the sample was firmly attached to the coil by running a topographic scan on the sample with a factory recommended resolution. For a writing tip, standard mode tips supplied by the manufacturer were used. In the previous switching field measurements, low moment tips were used. Such tip had a very thin magnetic coating and therefore the pillars were less affected by the tip field during the normal imaging. However, these tips did not generate a writing field strong enough to perform writing and thus the standard mode tips with a thicker coating were used in the PMR experiments. The standard tip provided enough field to play a role in the writing process, but too strong for some pillars so that it switched their magnetizations during normal imaging. The same coil described in Table 2.1 was used in this setup for writing experiments. This coil together with a programmable power amplifier can generate a field pulse with amplitude as large as 1000 Oe and duration as small as 3 msec.

During PMR experiments, several extra features of D3500, not used in standard scanning modes, are implemented. Signal access module (SAM) is used to monitor the scanning parameters in real time. These parameters are not usually shown on the main

computer screen. SAM is a signal break up circuit that has BNC connectors of both input and output ports for the signals going back and forth between the SPM head and its controller. The SPM head includes all the hardware components such as the piezo actuators, photodetector, sample stage, closed loop sensors, etc. The important signals that can be monitored by SAM include the photo-detector output, control input for the piezo actuators, the outputs from the closed loop sensors, etc. Another non-standard feature is Nanoscript software, which has a library of script commands that runs D3500 system in a user-defined operation sequence. Some operations that such software allows are not included in the standard D3500 operation software. The library includes the functions, for example, that position the tip in a user-specified location, and scan the tip following user-specified paths with or without turning the constant tip-sample gap control. Note that Nanoscript is a high level programming language and therefore low level operation schemes requiring a high computation speed cannot be performed with it.

The experimental procedures are summarized in the following.

1. Magnetization of the tip and the sample

The sample is first magnetized with a strong permanent magnet. The tip is magnetized in the direction opposite to that of the sample so that it aligns with the writing field, describe in step 4.

2. Initial imaging of the pillar arrays including the target pillar

Next, the region that includes the target pillars and its neighboring pillars is imaged with the MFM and the magnetic states of the pillars are determined. A 3 × 3 pillar array with the target pillar at the center is chosen for the scan area. In the MFM image, some pillars may have switched their magnetization due to the influence of the tip field. In the MFM phase image, these pillars will appear as black dots, meaning that the pillars' magnetization is aligned with the direction of the tip magnetization. We exclude the possibility of tip

magnetization reversed under the influence of the field from the pillars. If the target pillar appears black in the MFM image, one should choose another pillar to perform writing.

3. Contact of the tip to the center of the target pillar

The scan area is zoomed several times so that the image barely contains the target pillar and the area is centered on the pillar. Then, the size of the scan area is reduced to zero. This will fix the probe to the center of the scan area and therefore to the center of the target pillar. The closed loop control feature of D3500 facilitates positioning of the tip to the pillar center. The piezoelectric actuator usually suffers a large hysteresis. Such nonlinear behavior of the piezo affects the motion of the tip and makes it very difficult for the users to zoom in and out without losing the imaging features on the sample. In D3500, the extra sensors in x, y, and z directions are used to move the tip accurately regardless of any hysteresis effect and keep an error down to 1nm.

In order to lower the tip until it contacts the pillar just lightly, a new operating scheme for D3500 is written with Nanoscript. In this scheme, first, the control unit for the constant tip-sample separations is turned off, making the tip free to move in the vertical direction. This is performed by using *LithoFeedback()* among the Nanoscript functions. Then, the oscillation of the cantilever is halted by using the function. *SetDriveFreq()* with its input frequency equal to 0. Finally, the tip is moved towards the sample surface by using *LithoMoveZ()*. This function programs the system to move the tip in vertical direction with the distance specified by the user. The tip is then kept in for 4-5 seconds and moved up to the original position by using *LithoPause0* and *LithoMoveZ()*. Each time the tip is moved to the lowest point, we confirmed that the tip was in real contact with the pillar by monitoring the deflection of the cantilever through SAM. The deflection is measured by the photodector of D3500. When the tip is pulled down, the voltage signal from the photodetector increases and when it is pushed up, the voltage decreases. The following

describes the change of voltage when the tip is near the surface.

First, the voltage increases slightly near the sample surface. This is probably due to the effect of van der Waals force, pulling the tip towards the sample. Further movement of the tip towards the sample eventually drops the voltage. From this point, the voltage drops proportionately with the tip motion towards the surface. The decrease of the photodetectors' output voltage means that the tip is pushed up by the sample and therefore the tip is in contact with the sample.

4. Application of the field from the coil

At the instant that the voltage from photodetector starts to drop, a field pulse is applied to the sample using the coil. The duration of the field pulse is about 3 msec.

5. Rescanning of the Target Area

Again, *LithoMoveZ0* is used to pull up the tip to the original position and other functions to return to the standard scanning mode. The same area selected in step 2 is imaged and the result of the above writing is evaluated. If the target pillar isn't switched, steps 2 through step 5 are repeated with an increased field of the coil. In our experiments, the field was raised with increments of approximately 20 Oe starting from 100 Oe to 200 Oe depending on the previously measured switching field of the pillar. The repeated application of current pulse above 5 A should be avoided; otherwise the coil will be heated up significantly.

3.4.2 Experimental Results

We were successful in writing bits onto the perpendicular patterned media with a period as small as 200 nm, following the procedure described in the previous section. We again stress that demonstration of higher recording density is possible if such samples are provided. We expect that bits with a size comparable to the radius of curvature of the magnetic tip,

currently 25-50 nm, can be written with this method.

There were two issues that concern the PMR experiments. First, it was observed that at the instant a field, larger than 500 Oe, was applied, the tip crashed deeply into the sample surface. Such motion of the tip could be speculated form a sudden drop of the photodetector output voltage. It is most likely that the coil field pulled the nearest magnetic parts of the MFM system towards itself and therefore towards the sample. Such an accidental motion of the tip caused by the coil field will result in a major destruction of the sample. When the crash happened, both the tip and the pillar were damaged. The higher the applied field, the more severe was the damage and with the coil field around 700 Oe, the pillar was completely destroyed. To avoid damages to the pillars, an alternative method of contacting the tip was used. In this method, a field was applied to the pillar while the tip was oscillating and tapping the top center of the pillar. The tip-sample separation was maintained constant during this process. Such operation was performed in the tapping mode. In this mode, the tip hits the sample surface about 10,000 times per second. Because the feedback was always tuned on in this mode, it recovered quickly to the previous gap distance when the tip was pulled towards the surface and therefore greatly lessened the damage from the crash. During a field pulse of 3 msec, the tip contacts the pillar as frequent as 1000 times. Note also that the magnetizing speed was very fast, usually in a nano-second range.

The second issue is that it was difficult to find a 3 × 3 Ni pillar array in which the magnetizations of all pillars were not switched by the tip field during the initial imaging in step 2. As shown in Chapter 2, our sample had a very wide distribution of the switching field, ranging from 200 Oe to 700 Oe. The pillars with low switching fields in the range of 100 Oe-300 Oe were observed to flip due to the field of the standard tip. In Figure 2-13, we have seen that the switching field was distributed evenly over the whole pillar array.

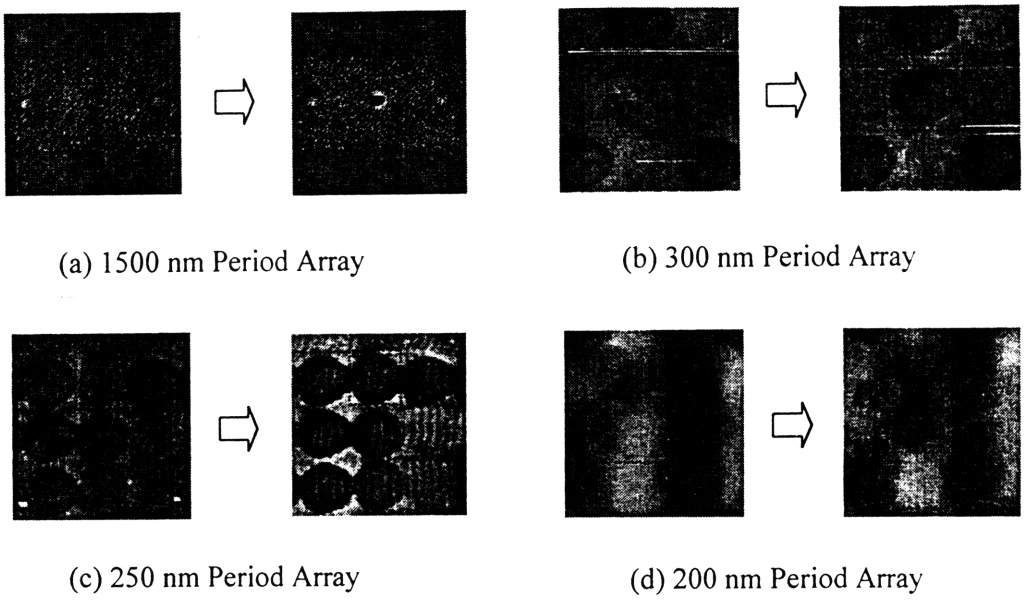

(a) 1500 nm Period Array (b) 300 nm Period Array

(c) 250 nm Period Array (d) 200 nm Period Array

Figure 3-2 MFM images of 6 × 6 Ni pillar arrays of various spacing before and after PMR writing. The pillar in the dotted box is the target pillar.

This trend made it difficult to find a 3×3 pillar matrix with the switching field of all pillars higher than 300 Oe.

The result of writing onto the pillar arrays with various spacings is shown in Figure 3-2. A pillar in the dashed box is the target pillar. The figure shows the MFM image of the 3 × 3 pillar array taken before and after the writing was performed. As one can see by comparing the two images, only the target pillar reversed its magnetization. Such a process did not switch the adjacent pillars. One exception was the pillar on the left hand side of the target pillar in the 200 nm period array. The behavior of this pillar is given an explanation later in the section, but for now we assume that the state of the pillar is not changed due to the writing process. Note that the states of several pillars in the array were already switched after the initial imaging. If the pillar array with uniform switching fields is available, a better demonstration of PMR writing will be possible.

For the 200 nm period array, the state of the target pillar switched when the field between 200 Oe and 240 Oe was applied. In the process, the images of smaller scan areas like the dotted square in Fig 4.2(d) were taken to ensure that the center of the scan area matched well with the center of the pillar. The offset command in the system's main software was used to center the scan area. When the tip was tapping on the top center of the pillar, a field was applied to the direction of the tip magnetization and increased with an increment of 30 Oe till the magnetic pattern of the pillar was reversed.

In Fig 3-2(d), one can notice that the pillar on the left side of the dotted square changed form black to white, opposite that of the target pillar, when the writing was performed. The polarity change of that pillar was against the direction of the writing field. From the following three points, it can be deduced that the magnetization of this pillar switched after the target pillar and it was originated from the interaction between the pillars. First, the center pillar was switched to the state that increases the interaction field in the direction against the pillar's initial magnetization state. Second, the switching field of the pillar was the lowest of the pillars in the array. This makes the pillars have the highest chance to be influenced by the external field. Third, the spacing between the pillars relative to the size of the pillars was small enough to cause an active interaction between the pillars as proven by the theory and experiments conducted in the next chapter.

3.4.3 Experimental Determination of Writing Field Strength

One must know the exact amount of the field applied to a pillar during the writing process for many reasons. However, the measurement of the field is a challenging task because the total flux available for the sensor is very small and the region of the field is too small for the sensors to access. Here, we propose a method that can measure the writing field during PMR process regardless of these limitations. This method makes use of the pillar arrays

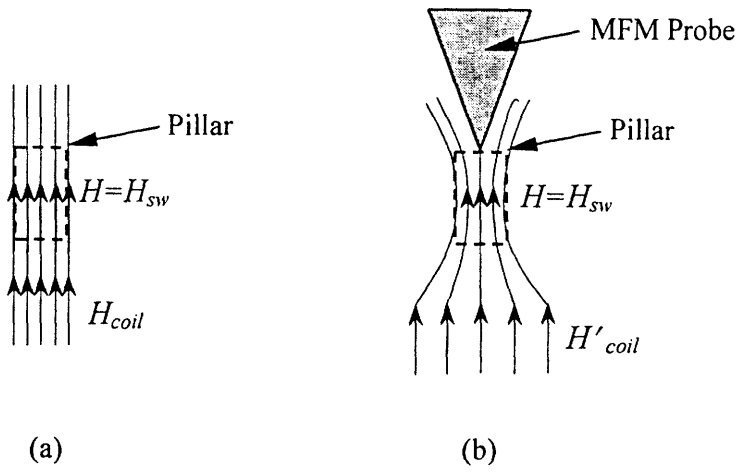

Figure 3-3 Schematic of writing field measurement (a) Coil field (H_{coil}) applied t the pillar when the switching occurs without MFM probe near the pillar (b) wit MFM probe contacting the top center of the pillar

with known switching fields.

Figure 3-3 shows the schematic of the proposed method. During the PMR process, the tip contacts the pillar and the coil field, represented as H'_{coil} in Figure 3-3(b), is applied. Using this method, we want to find out the field applied to a pillar, defined as H in Figure 3-3(b), when H'_{coil} is known. In this method, first, the switching field of a pillar is measured by following the procedure described in Section 2.3.3. This process is depicted in Figure 3-3(a). Here, the MFM probe plays no role in magnetizing the pillar. The coil field, H_{coil}, which reverses the state of the pillar, is the actual field, H, applied to the pillar and therefore it can be considered as the switching field, H_{sw}. Next, the state of the same pillar is reversed using PMR process as depicted in Figure 3-3(b). Because we know that the field applied to the pillar is concentrated due to the effect of the magnetic tip, we can predict that the coil field, H'_{coil}, which switches the pillar magnetization, is lower than the H_{coil}, previously measured in Figure 3-3(a). However, we know that the switching field of the pillar is the same regardless of the measurement method and therefore the same field equal

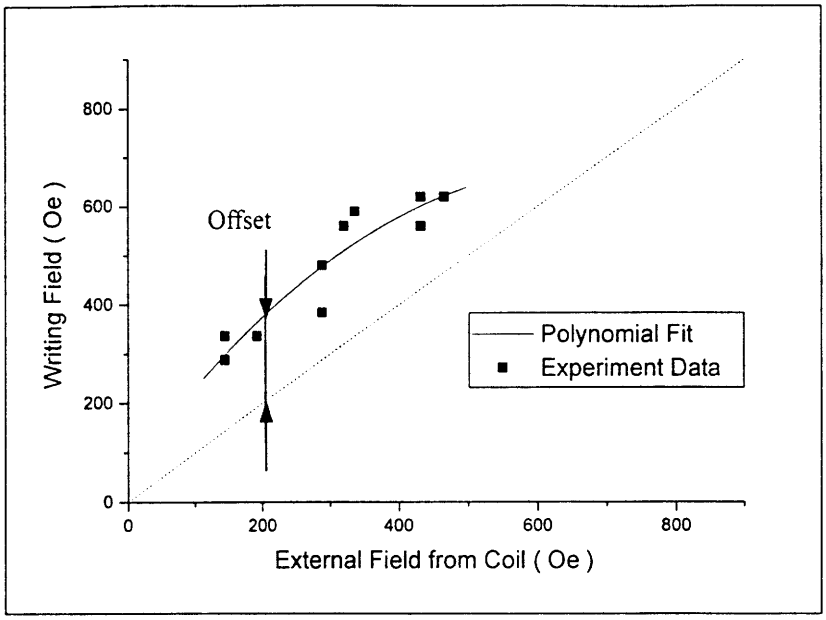

Figure 3-4 Strength of the writing field near the tip asa function of external fiel from coil

to H_{sw} is applied to the pillar at this instant in both measurements. Therefore, we can obtain one data point that relates the coil field to the writing field applied to the pillar during the PMR process. By taking the data points from the pillars that have a different switching field, we can now draw a plot as shown in Figure 3-4. In the graph, the horizontal axis is the coil field and the vertical axis is the writing field of PMR. The wide distribution of the switching fields in our pillar array actually facilitated taking many data points. In the measurement, the pillar array with a spacing of 300 nm was chosen so to ensure that interaction effect was very small.

Figure 3-4 shows a second order polynomial fit on these data points. This is represented by the black solid line that passes through the data points. The dashed line represents the case when the field at the tip is the same as the field from the coil. It can be easily predicted that the data points are always above this dashed line. Otherwise, it means that the concentrated field near the tip has lover value than the external field from the coil.

In the Figure, the polynomial fit has a slope similar to that of the dashed line. It indicates that the concentrated field near the tip is always larger than the coil field by a constant offset value. The offset was roughly 200 Oe. This offset is expected to be higher with the stronger tip field. The experiment with the low coercivity tip showed that the offset is much less than that shown in Figure 3-4.

4.5 Simulation of PMR Field

A simulation on the point magnetic recording process was performed using commercial field analysis software, Maxwell® from Ansoft Corp. The simulation focused on the analysis of the writing field during the point magnetic recording process. First, the writing field as a function of both the coil field and the strength of the tip field was obtained and compared with the experimental data. Also, the field distribution around the tip at the instant the coil field was applied was simulated and analyzed. The simulation was performed in 2 dimensional space from the assumption that the magnetic field was symmetric around the center axis. We found some useful simulation data that agreed well with experimental data and explained the fundamental mechanism behind the writing process. The results were also useful for the design of writing device, choosing the right tip and coil field for a given pillar array. Section 3.4.1 describes the various inputs to the simulation and their assumptions. In Section 3.4.2, the fundamental theories behind the simulation are reviewed. Finally, in Section 3.4.3, the results are discussed.

3.5.1 Inputs

The simulation software requires two important inputs. First, the geometry of all the magnetic objects that are to be simulated should be provided to the software. Because the

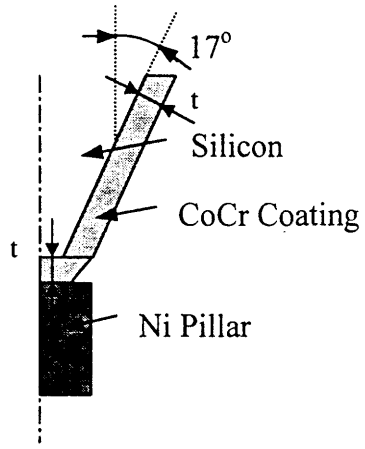

Figure 3-5 Geometry of the pillar input to the simulation software

simulation was performed in 2 dimensions, the software needed only the input of half plane geometry of the objects. Figure 3-5 shows the geometry used in the simulation of the writing field. In the figure, the main objects are a Co coated MFM tip and a Ni pillar. Although the exact geometry of the tip was not known, it was inferred from the manufacturer's specifications, which included the tip angle and the radius of curvature. According to the specifications, the tip angle was $17^0 \pm 2^0$ for the MFM tip used in the writing. For the tip radius of curvature, a relatively wide range, 25-50 nm, was given. Also, the thickness of the Co coating was given to be 15 –45 nm. From these specs, first we defined the tip angle to be 17^0. Also, the shape at the end of the tip was represented with the straight lines for the convenience of the software implementations. The variable, t, in the figure indicates the thickness of the magnetic coating. We left the thickness as a variable because in the simulation, several different coating thicknesses were used to study the effect of the tip field on the writing field. Note that the thickness of the coating on the tip is closely related to the strength of the tip field.

Secondly, the magnetic properties of the MFM probe have to be input to the software. The software requires the input to be in the form of a hysteresis curve. Figure 3-6

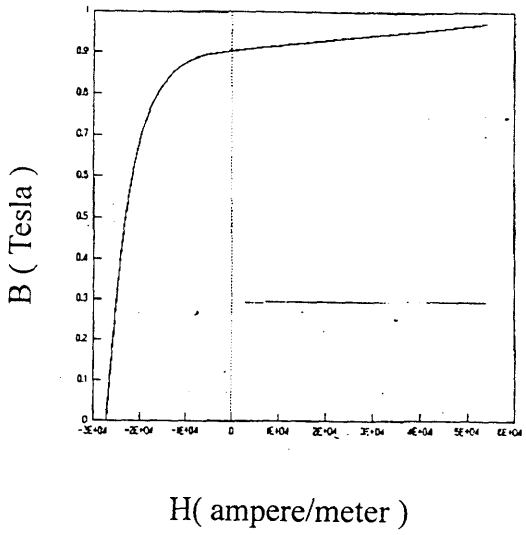

Figure 3-6 Hysteresis loop of the MFM probe input to the simulation software

shows the hysteresis loop of the magnetic tip that we used in the simulation. The manufacturer's data for the tip hysteresis are not usually available due to the difficulty in the field measurement. In this simulation, the hysteresis loop of the tip was estimated using the data of other tips reported in the literature. The hysteresis loop obtained by Babcock et al. [70] was used. In their work, the coercivity of CoCr pyramidal tip was given as 340 Oe. The thickness of CoCr film was 40 nm. For the value of saturation magnetization, M_s, the data obtained by Proksch et al. were used [71]. It was 720 emu/cm^3.

3.5.2 Simulation Engine

The Maxwell® simulator performs static magnetic field analysis. The source of the static field can be the current density in conductor, an external magnetic field represented through boundary conditions or a permanent magnet. In the simulation of the PMR process, the external field generated form the coil was used as a source of the static field. This was defined through the boundary conditions. The simulator solves for the magnetic field, H,

and the magnetic flux density, B, is automatically computed from H based on the given properties of the magnetic objects.

The simulator computes the magnetic field using Ampere's Law and Maxwell's equation describing the continuity of flux. The equations for those laws are given by

$$\nabla \times \mathbf{H} = \mathbf{J} \tag{3.1}$$

$$\nabla \bullet \mathbf{B} = 0 \tag{3.2}$$

respectively, where **H**(x,y) is the magnetic field and **J**(x,y) is the current density field. In our case, **J** was O since no current was involved in the simulation. Note that the external field from the coil was input to the simulation through the boundary conditions. **B**(x,y) is the magnetic flux density. The magnetic flux density is computed using the relationship:

$$\mathbf{B} = \mu_r \mu_o \mathbf{H} \tag{3.3}$$

Where μ_r is the relative permeability and μ_o is the permeability of free space which is equal to $4\pi \times 10^{-7}$ H/m. In computing Eqs. (3.1) and (3.2), the simulator uses the external magnetic fields defined by the user.

The simulated area is divided into small elements with the shape of triangle. The simulator computes the magnetic field H at the vertices and midpoints of the edges of each triangle in the finite element mesh. If nonlinear materials are present, it computes the field using the Newton-Raphson method, which uses the slope of the BH curve to compute a linear approximation of the nonlinear solution. This approximation is then substituted into the nonlinear solution for H. The software writes the completed solution to a file and performs an error analysis. In an adaptive analysis, it refines the triangles with the highest

error, and continues solving until the stopping criterion is met.

3.5.3 Results

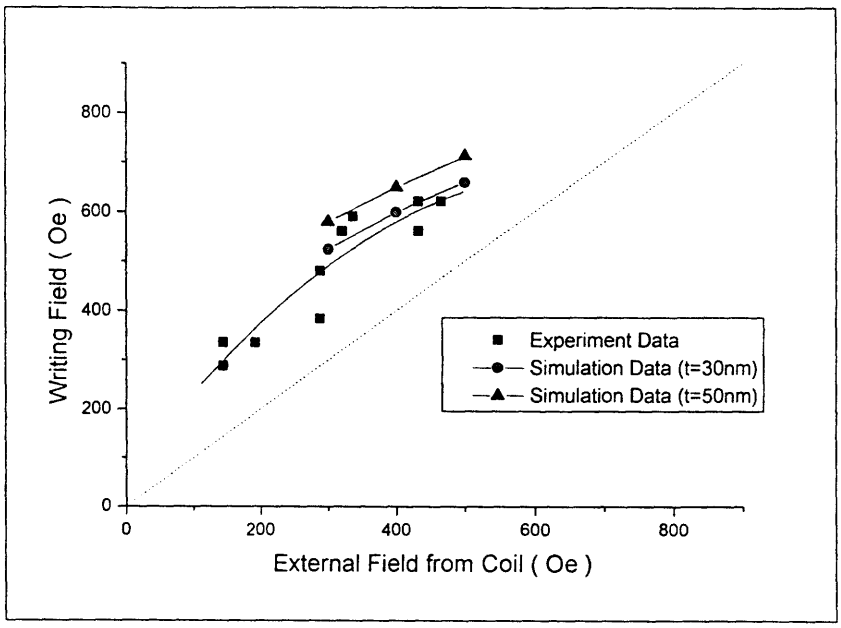

Figure 3-7 Simulation results of writing field during PMR process

In the simulation, the effects of the coil field and the thickness of Co film, t, on the writing field formed near the tip were observed. The resulting graph from the simulation is drawn in Figure 3-7. In the figure, x axis is the coil field applied to the pillar during the writing and the y axis is the resulting field formed near the magnetic tip. The values of the y axis were obtained by taking the volumetric average of the magnetic field in the space of the pillar, shown in Figure 3-5. The figure also shows two curves, each with different thickness of magnetic coating on the tip. The curve with circular dots represents the data for the coating thickness of 30 nm and the other curve with the triangular dots represents the data for the thickness of 50 nm. In the figure, the experimental data are also drawn for

comparison. At the coil field between 300 Oe and 500 Oe, both simulation curves are nearly parallel to that of the experimental curve. There is, however, a slight discrepancy in the y axis with the amount different for each coating thickness. An offset in Figure 3-7 represents the difference between the writing field and the coil field. The simulation curve with a larger thickness seems to have a larger offset. We stress less the exact match of the curve because we suspect that the hysteresis loop of the tip input to the simulation, described in Section 3.4.1, is not perfectly accurate. Note that the thickness of the magnetic coating determines the strength of the tip stray field. Therefore, we can conclude that the tip field is the dominant factor that determines the difference between the writing field near the tip and the coil field and that the writing field increases at nearly the same rate as that of the

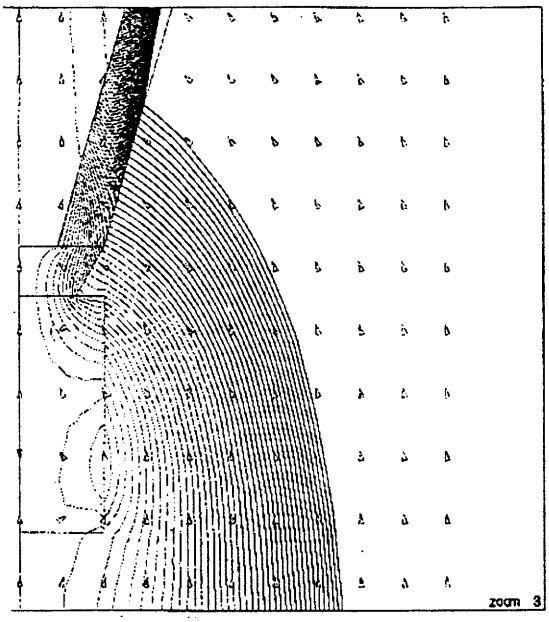

Figure 3-8 Magnetic field distributions around the tip

coil field. Figure 3-8 shows the field distribution around the pillar at the external field of 300 Oe. In the figure, the writing field is much concentrated near the tip as predicted. The maximum field at the tip was roughly 8 times the field applied outside.

3.6 Summary

In this Chapter, a basic concept of the high resolution writing technique using magnetic force microscope was introduced. This scheme was used in writing bits onto the perpendicular patterned media. The actual field applied to the pillar during the PMR writing was experimentally determined and represented as a function of an external field. Finally, these data were compared with the simulation results obtained form Maxwell® mangetostatic field analysis software. It was found that both data were in good agreements.

Chapter 4
Interactions

4.1 Introduction

In Chapter 2, the fundamental media property, the switching field, was discussed. In the switching field distribution plot presented in Section 2.3.5, we saw that the distribution width increased as the spacing was reduced from 300nm to 200nm. One can easily think that the interaction between pillars, which depends heavily on the spacing, plays a role. The interaction field is a long range magnetostatic field, resulting from the magnetization of each pillars and therefore the state of the neighboring pillars are important in interaction field calculation. As we will see in the next sections, the interaction field can become significantly high as the pillars (bits) in patterned media are packed densely together. In the extreme case, the interaction field applied to a pillar becomes higher than the switching field of that pillar so the pillar reverses its magnetization. This phenomenon is fatal in data storage applications.

In this chapter, we will provide an experimental way of measuring the interaction fields between the pillars with a period as small as 200 nm. This is the first time that the interaction field is directly measured from the individual pillars in perpendicular patterned media. We will also provide a theoretical model that can validate the experimental data. The model was found to be in good agreements with the experimental results. The model will support the determination of the crucial dimensions such as the pillar size and the spacing in design of high density patterned media. Up to this point, the interaction field

study was mostly performed using the 'delta-M' or Henkel technique based on the measurement data obtained from vibrating sample magnetometer (VSM). This is a macroscopic analysis based on the simultaneous measurements from the whole pillar array, and the average value of the interaction fields can be obtained. However, in the data storage applications, the behavior of individual pillars is more important in that the actual data writing is performed on each single unit of data at a time. The scheme, discussed in this chapter, can directly measure the interaction field through accessing, manipulation, and observing each pillar, at a recording density as high as 16 Gbit/in^2.

Section 4.2 reviews the previous literatures. Section 4.3 provides the definitions of the terms that are used in the later sections and presents the fundamental concept of the interaction fields in perpendicular patterned media. The measurement procedures of the interaction fields and the results are provided in the next section. In Section 4.4, a theoretical model based on the magnetostatic field theory are described and compared to the experimental data. In the last section, we will discuss general implications of the model regarding the design of patterned media.

4.2 Background

The 'delta-M' or Henkel technique is used to determine the nature of magnetic interactions between the single domain particles from the collective behavior of the particles measured by AGFM or VSM. This indicates whether the interactions are positive (magnetizing) or negative (demagnetizing) [72-74]. The measurement of the interaction fields directly from individual single domain particles was performed by Pardavi-Horvath et al. [75][76]. They used a two-dimensional array of single domain garnet particles with the easy axis vertical to the film. The size of these square particles was 42 μm × 42 μm × 3 μm and the particles were separated by 12 μm wide grooves. The states of the particles were observed

magnetooptically with a polarizing microscope. Under an increasing external field, the state of a particle was monitored till the magnetization was switched. The switching fields of the pillar both in position and negative direction were measured and the total net interaction field applied to the pillar was calculated. Such measurement was possible because the size of the particle was large enough for the instruments to apply a known field to the individual particles and also to monitor the state of the particles. In the recording media, however, each bit has the size of at least several hundred nanometers, nearly two orders of magnitude smaller than those particles.

Numerical models have been developed to simulate the switching of assemblies of interacting single domain particles. For example, models based on uniformly magnetized magnetic grains with a certain distribution of easy axes were developed. Refer to Section 2.4. These models, initially for the study of thin film media, have not been applied in detail to investigate the behavior of assemblies of interacting magnetic particles because of the computational difficulty. On the other hand, the arrays of single domain particles with perpendicular magnetizations can be treated relatively simply as arrays of interacting dipoles with an easy axis vertical to the sample plane. In [76], the demagnetizing tensor for an individual non-ellipsoidal particle was computed and the interaction field acting on the center pixel from its neighbors was calculated both by the dipole approximation and exact calculation of the surface integrals.

4.3 Concept

The basic configuration for the interaction fields between the pillars in the perpendicular patterned media is shown in Figure 4-1. $H_{A\rightarrow B}$ is defined as the interaction field from Pillar A applied to Pillar B. $H_{A\rightarrow B}$ is a long range magnetostatic field that is determined by Pillar

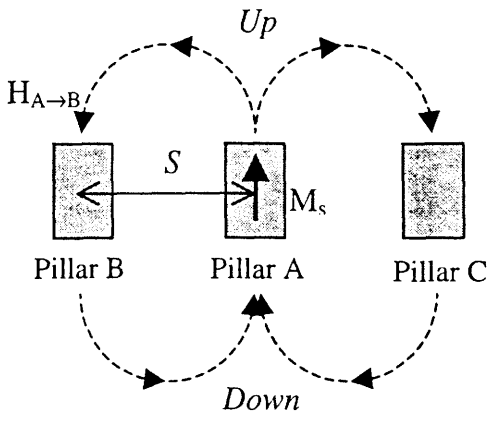

Figure 4-1 Schematic of interaction field between the pillars

A's geometry and magnetization state and the distance between Pillar A and Pillar B. We have seen in Chapter 2 that, due to a strong shape anisotropy, the magnetization of each single domain pillars was forced to align with the out of plane axis, having two possible magnetization states, equal in magnitude but opposite in direction. Although, for some pillars under observation, the magnetization was not exactly on the vertical axis, the deviation angle was small enough to be ignored and we assume that all pillars have easy axis exactly along the vertical axis. Such an assumption greatly simplifies the interaction field calculations. Figure 4-1 shows the effect of Pillar A's field on the neighbor pillars, Pillar B and Pillar C. In the figure, the magnetization of Pillar A is set to point *Up* between the two possible states. The resulting interaction field, acting on Pillar B and Pillar C, will be pointing downward following a field distribution of a simple permanent magnet. Because the exact vertical magnetization of pillar A is assumed, at the center of Pillar B and Pillar C, there will be only the vertical component of the interaction field. As a result, the interaction field in Figure 4-1 becomes a much simpler one-dimensional problem. This will facilitate the calculation process that will be discussed in Section 4.4.

Suppose that a strong external field magnetized Pillars A, B, and C in upward direction, which we define as +Z. As we discussed above, the interaction field due to

Pillar A, applied to Pillars B and C will be pointing downward, defined as –Z. Think now that a field in –Z direction is applied to the pillars and, this time, slowly increased from zero. The interaction field due to Pillar A will aid the applied field in –Z direction and Pillar B and Pillar C will reverse its magnetization at the earlier field than when there is no Pillar A present. This will result in a lower switching field. The higher switching field would be obtained if the magnetization of Pillar A were in –Z direction. This argument applies well to the test samples. The switching field of a pillar measured in Chapter 2 is not a 'true' switching field but the sum that includes the net interaction field from the neighbor pillars. This may have contributed to the non-uniformity of the switching fields as observed in Figure 2-12. Random sets of neighboring pillar states will produce an unpredictable switching field of the pillar. We should therefore find out how strong the interaction field is to affect the measurement of the switching field.

Let us think about the limiting case when the interaction field becomes too large. It would be when the total interaction field from the neighbor pillars alone is strong enough to switch the state of a pillar. The worst case of the neighbor pillars' states is when the pillars including the target pillar are all magnetized in the same direction. The interaction field from all the neighbors will be against the pillar's magnetization. We can now define a useful parameter in design of patterned media, called critical spacing, S_c. S_c is defined as a spacing between pillars when the net interaction field for the worst set of the adjacent pillars' state is equal to the switching field of the pillar. If the spacing becomes smaller than S_c, the pillars will have chance to reverse their magnetizations without any fields applied from outside the pillar array. This poses a fatal limitation on the data storage applications. This parameter is useful in calculating the possible recording density when pillar geometry is given, usually limited by the fabrication technology.

4.4 Interaction Field Measurement

As mentioned before, the measurement method that will be provided in this section is microscopic in a sense that the probe directly accesses each pillar during the analysis. The media with a recording density of 16 Gbits/in^2 or more have been studied with this method. We also expect that the measurement of higher density patterned media is possible if the test samples with the smaller diameters of the pillars can be provided.

Section 4.4.1 introduces the basic concepts implemented in the measurement and provides the definition of the experimental parameters. In Section 4.4.2, the detailed description of the measurement procedure is provided. And finally in Section 4.4.3, the measurement results are presented and discussed.

4.4.1 Measurement Principle

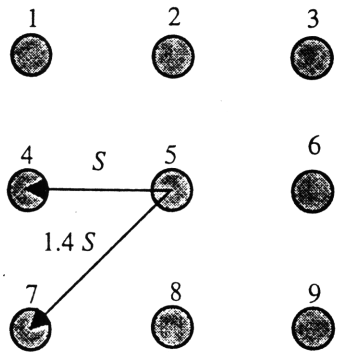

Figure 4-2 3 × 3 pillar array with spacing S where the interaction field is applie to Pillar 5 by the surrounding eight pillar.

Figure 4-2 shows the nine pillars, numbered from 1 through 9 and regularly spaced in a grid format. We will take into consideration only the eight neighbor pillars surrounding the center pillar for the sources of the interaction field. As we will see later, the effect of the

pillars outside these eight pillars is small enough to be disregarded. H_{ji} is defined as the interaction field due to Pillar j, applied to Pillar i. H_{15}, therefore, is the interaction field due to Pillar 1, applied to Pillar 5. According to the argument in Section 4.2, the sign of H_{15} will be always opposite to that of Pillar 1's magnetization. We chose the sign to be minus when the direction of a field or magnetization is towards the back of the page and positive for the opposite case. The net interaction field, H_{net}, due to the eight surrounding pillars, applied to Pillar 5 can be expressed in the equation as

$$H_{net} = H_{15} + H_{25} + H_{35} + H_{45} + H_{65} + H_{75} + H_{85} + H_{95} \tag{4.1}$$

In the equation, all variables are scalar quality since it is assumed that only the vertical component of the field exists. Also note that the pillars with the even numbers, 2, 4, and 6, are closest to the center pillar while the odd numbered pillars are square root of 2 times the spacing, S, away from the center. We can quickly figure out that $H_{15} = H_{35} = H_{75} = H_{95}$ and $H_{25} = H_{45} = H_{65} = H_{85}$ if the same magnetizations of the pillars are assumed.

We can experimentally obtain the net interaction field, H_{net} in Eq. (5.1), by measuring two parameters, *Up* (+Z) switching field and *Down* (-Z) switching field. Up switching field is defined as an external field needed to switch the pillar in +Z direction and down switching field is defined as the opposite. Up switching field has the relationship given by

$$H_{sw}^{up} = H_{sw}^{true} - H_{net} \tag{4.2}$$

where the H_{sw}^{true} is an intrinsic switching field that can be measured only when there are no pillars surrounding the target pillar. Down switching field has the same relationship but with the opposite sign for H_{net}, given by

$$H_{sw}^{down} = H_{sw}^{true} + H_{net} \tag{4.3}$$

If we subtract Eq. (5.2) from Eq. (4.3) and divide the result by two, we can obtain the following equation for the net interaction field.

$$H_{net} = (-1) \cdot \frac{H_{sw}^{up} - H_{sw}^{down}}{2} \tag{4.4}$$

Therefore, by measuring the H_{sw}^{up} and H_{sw}^{down}, we can obtain the net interaction field from the equation above. The resulting value, H_{net}, is the true interaction field contributed by all the neighboring pillars. This is different from H_{net} in Eq. (4.1) where only the effect of the pillars in the 3 × 3 array is considered.

There are several important issues that concern the experimental measurement of H_{sw}^{up} and H_{sw}^{down} at a high pillar density. First, during the measurement, a known testing field should be applied only to the specified pillar. In the previous switching field measurement, described in Section 2.3.5, an external magnetic field is applied to the pillar and increased at a certain step until it reverses its magnetization state. An electromagnet is used to apply the field to the pillars. This method can never guarantee that the neighbor pillars are kept in the same magnetization state when all the pillars are under the influence of the same external field. At the instant the neighbor pillars switch, the net interaction field applied to the target pillar will change to a new value. Secondly, it's difficult to quantify the field applied to these small size pillars during the measurements. The magnetic flux needed to switch the pillars is very small in size and it's not straightforward how the fields applied to the pillars should be measured. Lastly, if the net interaction field is to be measured by using Eq. (4.1), the state of the neighbor pillars has to be kept constant from the measurement of H_{sw}^{up} to H_{sw}^{down}. For the measurement of each switching field, the opposite field is applied the pillar. If some neighbor pillars reverse the magnetization state, then only the interaction field contributed by unchanged neighbor pillars can be obtained.

This is implied in Eq. (4.4). The writing technique described in Chapter 3 is the key technology in these aspects.

4.4.2 Procedures for Interaction Field Measurement

The same experimental setup, described in Section 2.3.5 was used in the measurement of the interaction field. The main components were the magnetic force microscope and the coil which can apply a field up to 1000 Oe.

1. Initial magnetization of the sample and the tip

First, a large field was applied to the sample and the pillars were magnetized in–Z direction, shown in Figure 4-1. The tip was also magnetized, but in the opposite direction, +Z, in order not to be affected by the coil field intended for the pillar switching. Note that the standard tip has the coercivity, usually around 400 Oe, comparable to that of the pillar.

2. Initial imaging of the target area

Next, an array of 3 × 3 pillars was selected and the magnetization states were observed by running MFM mode. This study investigates the interaction field applied to the center pillar resulting from the magnetization states of the surrounding eight pillars. From the resulting magnetic image of the pillars, it was found out whether the states of the pillars switched due to the effect of the tip field. Because the tip and the pillar were magnetized in the opposite directions, the actual contact of the tip to the pillar during the tapping scan mode may cause the pillars with small switching fields to flip their magnetizations. In the MFM phase image, these pillars appeared as black dots, meaning that the pillars were magnetized in the same direction as the tip. If the target pillar appeared black, it was discarded and a new 3 × 3 array was chosen.

3. Measurement of H_{sw}^{up} with PMR technique

The writing scheme described in Section 3.4.1 was used to measure H_{sw}^{up} of the target pillar. First, the magnetic tip was brought into contact with the target pillar. Here, the actual contact of the tip to the surface was verified by monitoring the change of the cantilever deflection through the photodector signal. Then, while the tip was in contact, a field was applied from the coil to the direction opposite the pillars' magnetization. This process was repeated with increasing coil fields until the state of the target pillar was reversed. The resulting coil field was converted to the actual field applied to the pillar using the empirically determined relationship between coil fields and writing fields shown in Figure 3-3. Throughout the measurement of H_{sw}^{up}, the state of any neighboring pillars should stay the same. In case switching occured in those pillars, a new set of pillars was selected for the interaction field measurement.

4. The tip re-magnetization and MFM imaging

For the measurement of H_{sw}^{down}, the tip was magnetized again in the reversed direction, -Z, and the same pillar assembly was scanned. It's likely that the pillars that are shown to switch due to the tip field last time will switch this time as well. If such pillars exist, it will result in the H_{sw}^{up} and H_{sw}^{down}, measured at different neighbor states[1]. From this measurement, it is important to verify that the target pillar is not affected by the tip field during this scan.

5. Measurement of H_{sw}^{down} with PMR technique

The same procedures were taken to measure H_{sw}^{down} with the coil field applied to the opposite direction, -Z. Then, the resulting field was recorded and converted.

---

[1] Still a useful analysis is possible in such a case. Actually it was the case in our measurements. Refer to the result section for more details.

6. Calculation of the net Interaction field

Eq. (4.4) was used to calculate the resulting interaction field, H_{net}.

4.4.3 Measurement Results

The interaction fields for the three different periods of the pillar array have been measured. In the test structure, the Ni pillars with a diameter of 90nm and the height of 180nm, in a 20 × 20 array were spaced at 300nm, 250nm, 200nm, and 150nm. The measurement at 150nm period array was not possible, because it was observed that the pillars switched rather randomly at a given external field, possibly due to the high interaction field. In this section, the results obtained from the 300nm, 250nm, and 200nm period arrays are presented. In the experiment, we observed that significant numbers of pillars were switched due to the magnetic tip. No 3 × 3 array in which the entire pillars were not affected by the tip could be found in the test sample. Therefore, H_{net} in Eq. (4.4) couldn't be obtained. In this section, a different approach was taken to draw a useful conclusion from the test sample.

1. 300nm period array

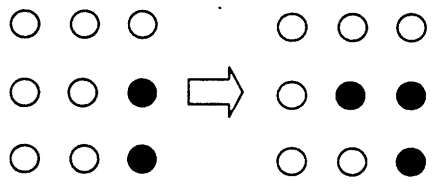

Figure 4-3 The target pillar was switched at the coil current of I_c = 0.4 A. Refe to Appendix A for real MFM images.

On the left side of the arrow in Figure 4-3, the initial magnetization state of 3 × 3 pillars after the first scan in step 2 is shown. In the figure, it can be seen that the states of Pillars 6

and 9 flipped due to the effect of the tip field. From Eq. (4.1), the resulting net interaction field can be expressed as

$$H_{net}^{+} = H_{15} + H_{25} + H_{35} + H_{45} - H_{65} + H_{75} + H_{85} - H_{95} \quad (4.5)$$

Here, a parameter, H_{net}^{+}, is used instead of H_{net}. This is to represent that the neighboring pillars were in different states when H_{sw}^{up} and H_{sw}^{down} were measured. In this case, H_{net}'s in Eq. (4.2) and Eq. (4.3) are not identical. Next, the switching field of Pillar 5 was measured by following step 3 described in Section 4.3.2. During the measurement, no states of neighbor pillars were flipped until the state of the center target pillar was reversed. This is shown on the right hand side of Figure 4-3. The state of Pillar 5 switched when the current between 0.3 A and 0.5 A was applied to the coil. Here, we select the median value, 0.4 A, as an approximated value. The corresponding value for the field generated in the coil is 40 Oe. This was from the previous measurement of the coil field. Refer to Appendix B. As mentioned in Section 4.3.2, this is different from the actual field applied to the pillar. From Figure 3-3, the coil field of 40 Oe is converted to the field applied to the pillar of 180 Oe. Therefore, the resulting up switching field of the target pillar is H_{sw}^{up} = 180 Oe.

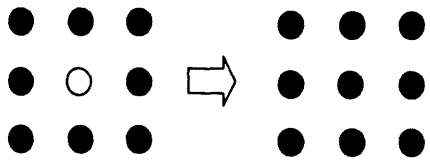

Figure 4-4 The target pillar was switched at I_c = 2.2 A

Figure 4-4 shows the MFM images of the pillars after the tip magnetization has been reversed. The pillars with the same magnetization state are now shown in the opposite color. As expected, Pillars 6 and 9 appear in black again. This shows that these pillars are

flipped by the tip field. The equation for H_{net}, for this case is

$$H_{net}^{-} = H_{15} + H_{25} + H_{35} + H_{45} + H_{65} + H_{75} + H_{85} + H_{95} \quad (4.6)$$

Following the same process used to derive H_{sw}^{up}, H_{sw}^{down} was found to be 350 Oe. Note that H_{sw}^{up} is lower than H_{sw}^{down}. By comparing Figure 4-3 and Figure 4-4, we can easily see that the state of the neighboring pillars in Figure 4-3 is more in favor of Pillar 5's switching. Therefore a much lower switching field should be obtained for H_{sw}^{up}. This argument agrees well with the measurement results.

The measured values of both H_{sw}^{up} and H_{sw}^{down} can be used to calculate the interaction field H_{net}. However, because the state of the neighbor pillars has been changed for the measurement of H_{sw}^{up} and H_{sw}^{down}, the resulting H_{net} from Eq. (4.4) has now a different meaning. If we substitute H_{net}^{+} for H_{net} in Eq. (4.2) and H_{net}^{-} for H_{net} in Eq. (4.3) and calculate the Eq. (4.4), then we get

$$H'_{net} = (-1)\cdot\frac{H_{sw}^{up} - H_{sw}^{down}}{2} = H_{15} + H_{25} + H_{35} + H_{45} + H_{75} + H_{85} \quad (4.7)$$

The net interaction field, H'_{net}, as seen in Eq. (4.7), omits the effects of Pillar 6 and Pillar 9. Those pillars are the ones that were flipped by the tip field. We can now see that the total interaction field contributed by entire adjacent pillars cannot be obtained if the state of the pillar changes under the influence of the tip field. An assembly of 3 × 3 pillars that are not affected by the tip field wasn't available in our test structure as was evident in Figure 2-11. From the measured H_{sw}^{up} and H_{sw}^{down}, H'_{net} of 85 Oe was obtained from Eq. (4.7). H'_{net} represents the interaction field applied to the center pillar by Pillars 1, 2, 3, 4, 7, and 8.

2. 250 nm period array

From Figure 4-5 (a), the resulting interaction field, H_{net}^{+}, from Eq. (4.1) is

$$H_{net}^{+} = H_{15} - H_{25} + H_{35} + H_{45} - H_{65} + H_{75} - H_{85} + H_{95} \quad (4.8)$$

The state of the center pillar was reversed when I_c was approximately 2.2 A. The corresponding H_{sw}^{up} is 360 Oe. MFM image of the same pillars taken with the reversed tip is shown in Figure 4-5 (b). The resulting H_{net}^{-} is

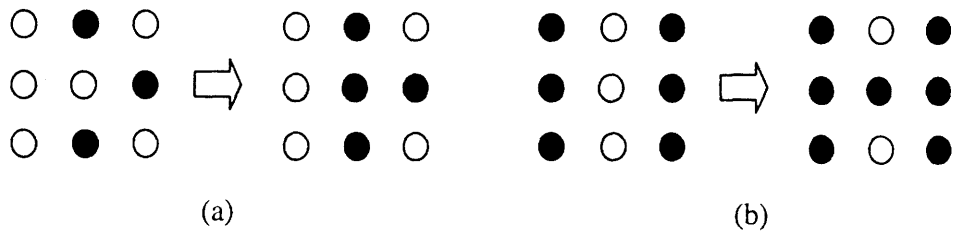

Figure 4-5 Magnetic state of the pillars in 250 nm period array before and after th writing field was applied. (a) The state of the center pillar was switched at I_c = 2.2 A. (b The switching occurred at I_c = 2.7 A. Here, the tip was magnetized in the opposit direction.

$$H_{net}^{-} = H_{15} - H_{25} + H_{35} + H_{45} + H_{65} + H_{75} - H_{85} + H_{95} \quad (4.9)$$

H_{sw}^{down} was measured to be 400 Oe. Following the same procedure, we get

$$H'_{net} = H_{15} - H_{25} + H_{35} + H_{45} + H_{75} - H_{85} + H_{95} \quad (4.10)$$

From the measured H_{sw}^{up} and H_{sw}^{down}, H'_{net} = 20 Oe. H'_{net} represents the interaction field applied to the center pillar by Pillar 1, 2, 3, 4, 7, 8, and 9.

3. 200 nm period array

From Figure 5-7,

$$H_{net}^{+} = - H_{15} + H_{25} + H_{35} - H_{45} - H_{65} + H_{75} - H_{85} + H_{95} \quad (4.11)$$

H_{sw}^{up} was measured to be 380 Oe. With the reversed tip, the MFM image shown in Figure 4-8 was obtained. The equation for the resulting H_{net}^{-} is

$$H_{net}^{-} = - H_{15} + H_{25} + H_{35} + H_{45} + H_{65} + H_{75} - H_{85} + H_{95} \quad (4.12)$$

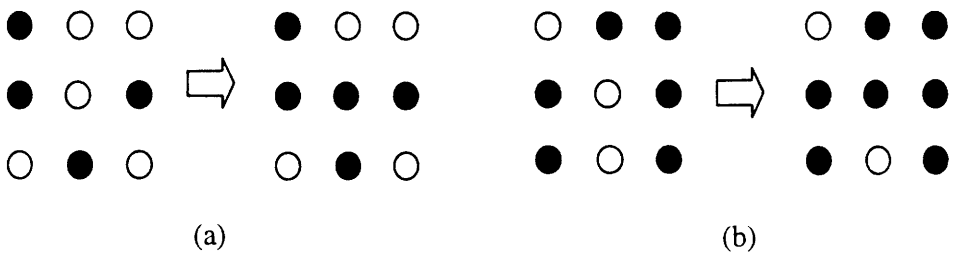

Figure 4-6 Magnetic state of the pillars in 200 nm period array before and after the writing field was applied. (a) The state of the center pillar was switched at I_c = 2.4 A. (b) The switching occurred at I_c = 3.4 A. Here, the tip was magnetized in the opposite direction.

H_{sw}^{down} was measured to be 530 Oe. By following the same procedure, we get

$$H'_{net} = - H_{15} + H_{25} + H_{35} + H_{75} - H_{85} + H_{95} \tag{4.13}$$

and from H_{sw}^{up} and H_{sw}^{down}, H'_{net} = 75 Oe, including the effect of Pillar 1, 2, 3, 7, 8, and 9.

4.5 Interaction Field Model

In this section, an interaction field model based on the magnetostatic theory is provided. The appropriate assumptions have been made to simplify the model. The exact calculations or modeling of the interaction field using a numerical method like finite difference method is not discussed in this thesis. In Section 4.5.1, the interaction field equation is derived from the magnetostatic field theory. A well-known dipole approximation in the magnetic potential problem was used in the derivation of the integrand in the resulting interaction equation. In the next section, the model was further simplified by using the configuration of our perpendicular patterned media. In the last section, the data from the model were compared to those from the experiments described in Section 4.4. The result showed that the model and the experimental data were in a very good agreement.

4.5.1 Fundamental Theory

We consider the interaction field between the two single domain magnetic elements of identical shape. Specifically, the case when Element i is applying a field to Element j will be considered. This is similar to the problem of calculating the demagnetizing field inside the arbitrary shape magnetic body. The magnetization in Element i creates a scalar magnetic potential on each part of Element j, given by

$$\Psi_i = \frac{1}{4\pi}\int_{V_j} dV_j \mathbf{M}_j \bullet \nabla_j \left(\frac{1}{r_{ji}}\right) \tag{4.14}$$

where $\mathbf{M}_j$ is the magnetization vector in Element j and r_{ji} is the distance between the center of Element j and the small portion of Element i for the above integral. [77] ∇_j is defined by

$$\nabla_i = \hat{x}\frac{\partial}{\partial x_j} + \hat{y}\frac{\partial}{\partial y_j} + \hat{z}\frac{\partial}{\partial z_j} \tag{4.15}$$

Using some vector theorems, Eq. (4.14) can be rewritten as

$$\Psi_i = \frac{1}{4\pi}\left(\oint_{S_j} \frac{dS_j \cdot \mathbf{M}_j}{r_{ji}} - \int_{V_j} dV_j \frac{\nabla_j \cdot \mathbf{M}_j}{r_{ji}}\right) \tag{4.16}$$

From the assumption that the magnetization in Element j is uniform. $\nabla_j \bullet \mathbf{M}_j = 0$ and Eq. (4.16) becomes

$$\Psi_i = \frac{1}{4\pi}\oint_{S_j} \frac{dS_j \cdot \mathbf{M}_j}{r_{ji}} \tag{4.17}$$

The magnetic field on Element i due to Element j is given by

$$\mathbf{H}_{ji} = -\nabla_i \Psi_i \tag{4.18}$$

$$\Psi_i = -\frac{1}{4\pi}\nabla_i \oint_{S_j} \frac{dS_j \cdot \mathbf{M}_j}{r_{ji}} \tag{4.19}$$

$$\Psi_i = \frac{1}{4\pi} \nabla_j \oint_{S_j} \frac{dS_j \cdot \mathbf{M}_j}{r_{ji}} \tag{4.20}$$

$-\nabla_i$ equals ∇_j due to the reciprocity of the two coordinates for Element i and j. Eq. (4.20) can be represented by the product of the vector M_j and the demagnetizing tensor matrix, D_{ij}, as given by

$$\begin{bmatrix} H_x \\ H_y \\ H_z \end{bmatrix}_{ji} = \begin{bmatrix} D_{xx} & D_{xy} & D_{xz} \\ D_{yx} & D_{yy} & D_{yz} \\ D_{zx} & D_{zy} & D_{zz} \end{bmatrix} \cdot \begin{bmatrix} M_x \\ M_y \\ M_z \end{bmatrix}_j \tag{4.21}$$

Each element in the matrix can be calculated by solving the integrand in Eq. (4.20). Exact calculation of the surface integral of Eq. (4.20) is possible through a long derivation of the Maxwell equation [75][76]. A simpler way of performing the calculation is to use the dipole approximation in which $1/r_{ij}$ in Eq. (4.20) is expanded into Taylor series and the first term is taken. Physically, this approximates Element j as a magnetic dipole. This, however, assumes that the $1/r_{ij}$ is small. If the distance between two elements is within 3 diameters of the element, it will generate an error as high as 20%. Note that the magnetic dipole moment is not dependent on the origin of the body coordinate of Element j, and it can be thought of as being a point dipole located at that origin. Therefore, $r_j = 0$ and $r_{ij} = r$. Finally, the equation becomes

$$\mathbf{H}_{ji} = \frac{3(\mathbf{m} \cdot \mathbf{r})\mathbf{r} - \mathbf{m}}{4\pi r^3} \tag{4.22}$$

where **m** is the magnetic dipole moment of Element j. $\mathbf{m} = \mathbf{M} \times$ (Volume of Element) for a uniformly magnetized element.

4.5.2 Interaction Field Model

Here, Eq. (4.22) is further simplified and used to describe the interaction field between

pillars in perpendicular patterned media. As discussed in Section 4.2, the interaction field has only a vertical component near the center of the pillar as the vertical magnetization of the pillars is assumed. If we take out z component of $\mathbf{H}_{ji}$ in Eq. (4.22), we get

$$H_z = D_{zz} \cdot M_z \tag{4.23}$$

$$= \frac{3z^2/r^2 - 1}{4\pi r^3} \times M_z \times (\text{Volume of Element}) \tag{4.24}$$

Because it's assumed that the pillars are in x-y plane, parallel to each other, z becomes 0. Also, M_z for single domain pillar is 4π times the saturation magnetization, a constant value for each type of material. If we plug in the volume of a cylindrical pillar for (volume of Element) in Eq. (4.24), Eq. (4.22) becomes

$$H_{ij} = -\frac{d^2 h}{16 r^3} \times 4\pi M_s \tag{4.25}$$

where d is the diameter and h is the height of a pillar. The pillar in our test sample has the diameter of 90 nm and the height of 180 nm. If we substitute the saturation magnetization of Ni for M_s, we get the equation for the interaction field between two single domain pillars as a function of the distance between the pillars, given by

$$H_{ij} = -\frac{5.54 \times 10^8}{r^3} \text{ Oe} \tag{4.26}$$

where the dimension of r is [nm].

4.5.3 Discussion

Eq. (4.26) can be used to calculate $\mathbf{H'}_{net}$ in Eqs. (4.7), (4.10), and (4.13). These values can be readily compared to the experimentally acquired $\mathbf{H'}_{net}$'s in Section 4.4.3. Here, we will take a different approach to compare the data obtained from the experiment and the theory.

$\mathbf{H'}_{net}$'s that are measured from 300 nm, 250 nm, and 200 nm period arrays will be converted to $\mathbf{H}_{ij}$ which is defined as the interaction field between the two nearest pillars. This conversion is made possible by using the theoretical relationship described in the previous section. From the pillar array diagram, shown in Figure 4-2, the distance between the second nearest pillar is the square root of 2 times the distance between the nearest pillars. We then have the following relationship regarding the interaction field between the nearest pillars, $\mathbf{H}_{nearest}$, and the interaction field between the second nearest pillars, $\mathbf{H}_{2ndnearest}$, from Eq. (4.26)

$$H_{2ndnearest} = \frac{1}{2\sqrt{2}} \times H_{nearest} \tag{4.27}$$

In Figure 4-2, Pillar 2, Pillar 4, and Pillar 6, and Pillar 8 are the nearest pillars to the center pillar and Pillar 1, Pillar3, Pillar 7, and Pillar 9 are the 2nd nearest pillars to the center pillar. By substituting $\mathbf{H}_{2ndnearest}$ in Eqs. (4.7), (4.10), and (4.13) with the right hand side of Eq. (4.27), we can obtain $\mathbf{H'}_{net}$ as a function of $\mathbf{H}_{nearest}$ as in Eqs. (4.28), (4.29) and (4.30) for each array respectively.

$$H'_{net} = (3 + 3/2\sqrt{2}) \times H_{nearest} \tag{4.28}$$

$$H'_{net} = (-1 + 4/2\sqrt{2}) \times H_{nearest} \tag{4.29}$$

$$H'_{net} = 2/2\sqrt{2} \times H_{nearest} \tag{4.30}$$

By using the experimentally determined $\mathbf{H}_{net}$'s in Section 4.4.3, $\mathbf{H}_{nearest}$ can be calculated for each pillar array. In Table 4.1, these values are compared to the interaction field between two Ni pillars calculated from Eq. (4.26). In the table, the term, $\mathbf{H}_{ij}$ is the same value as $\mathbf{H}_{nearest}$. The result shows that $\mathbf{H}_{ij}$'s from the experiment are in good agreement with $\mathbf{H}_{ij}$'s from the theory. This proves that the experimental data obtained in Section 4.3.3 are

	$\mathbf{H}_{ij}$ from Experiment	$\mathbf{H}_{ij}$ from Theory
300 nm Array	21 Oe	21 Oe
250 nm Array	48 Oe	35 Oe
200 nm Array	106 Oe	70 Oe

Table 4.1 Interaction field, $\mathbf{H}_{ij}$, from the experiment and theory

accurate. One can notice that the error of the model increases as the spacing is reduced. This may be due to error of the dipole approximation assumed in Eq. (4.22). The approximation produces more error as r decreases because the ignored higher terms in the Taylor expansion get larger. The errors may also be due to the calculations based on only eight nearest pillars. Figure 4-7 shows the interaction field, $\mathbf{H}_{ij}$, as a function of the distance between the two Ni pillars, as predicted in theory. In the plot, several experimental data

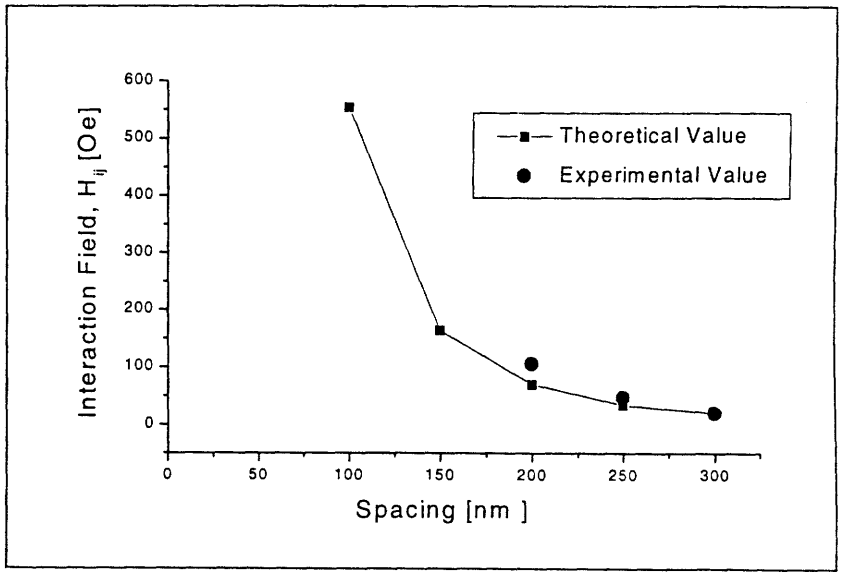

Figure 4-7 The experimental and simulation data of interaction field between two pillar as a function of distance between the pillars

points are drawn in small circles. One can see that the experimental data are in good agreement with the theoretical curve. Note that the interaction field increases exponentially as the spacing is reduced. A serious interaction field effect is expected for the smaller spacing.

4.6 Media Design

In Section 4.2, we learned that the net interaction field applied to a pillar is highest when all the adjacent pillars are magnetized in the same direction as the magnetization of the pillar. By using Eq. (4.1) and following the same procedure in the previous section, we can obtain the net interaction field for such a case as follows.

$$(H_{net})_{max} = 4 \times H_{nearest} + 4 \times H_{2ndnearest} \tag{4.31}$$

Using the relationship stated in Eq. (4.27), we get

$$(H_{net})_{\max} = \left(4 + \frac{4}{2\sqrt{2}}\right) \cdot H_{ji} \tag{4.32}$$

$$= 5.41 \times H_{ji} \tag{4.33}$$

Here, $(H_{net})_{max}$ is defined as the highest possible interaction field that can be applied to a pillar. The experimental values for H_{ji} that are provided in Table 4.1 are used in Eq. (4.33) to calculate the maximum interaction fields for the spacing of 300nm, 250nm, and 200nm and compared with the average switching field of the pillars, experimentally obtained in Section 2.3.5. Those are

$$300nm\ Period\ Array: (H_{net})_{max} = 114\ Oe \quad < 420\ Oe$$

$$250nm\ Period\ Array: (H_{net})_{max} = 260\ Oe \quad < 420\ Oe$$

200nm Period Array: $(H_{net})_{max} = 573\ Oe \quad > 420\ Oe$

Therefore, we can predict that some pillars in the 200nm period array reverse their magnetization without any external fields present. On the other hand, in the 300nm period array, such behavior of the pillars should not be seen. The switching field distribution of the pillars in 300 nm array is shown in Figure 2-8. In the figure, there are almost no pillars that have a switching lower than 114 Oe.

The critical spacing, S_c, is the spacing in the pillar array when the maximum possible interaction field applied to a pillar is equal to the switching field of that pillar. At a spacing smaller than S_c, the pillars with a given geometry may switch themselves without any fields from the outside. S_c can be calculated from the theories discussed in the previous sections. The maximum net interaction field, $(H_{net})_{max}$, can be calculated by using Eq. (4.25) to substitute for H_{ji} in Eq. (4.33). The resulting $(H_{net})_{max}$ is

$$(H_{net})_{max} = 5.41 \times -\frac{d^2 h}{16 r^3} \times 4\pi M_s \tag{4.34}$$

By equating the interaction field, $(H_{net})_{max}$, in Eq. (4.34) and the pillar switching field, H_{sw}, S_c is the function of the pillar properties including H_{sw} given by

$$S_c = \sqrt[3]{4.25 \times \frac{d^2 h M_s}{H_{sw}}} \tag{4.35}$$

Eq. (4.35) shows that the critical spacing, S_c, can be calculated if the pillar geometry and the magnetic properties are given. For the pillars in our test sample, the diameter was 90nm and the height was 180nm. Also, the measured switching field was 420 Oe. The critical spacing, S_c, is then calculated to be 193nm from Eq. (4.35). Taking in to account the 20% safety factor, we should expect the critical spacing to be about 230nm. Both the 200nm period array and the 150nm period array in the test sample have a smaller spacing than S_c. Therefore we can expect that the interaction effect may appear in these arrays. In fact, the automatic switching of the pillars was observed in these arrays during the experiments. For

example, in Section 3.4.2, we observed that one of the pillars in the 200 nm period array reversed its magnetization in the direction opposite that of the external field.

Previously, a 200 nm period array of Ni pillars was fabricated by using the interferometric lithography in the Nano-Structure Laboratory. The pillars in that sample had the diameter of 140 nm and the height of 320 nm. The maximum net interaction field for this pillar array calculated from Eq. (4.34) is roughly 1600 Oe, which is much higher than the expected switching field of the pillars. This indicates that the pillars in the sample will behave more like a continuous thin film. In actual MFM imaging of the sample, we found no evidence that the pillars can be independently magnetized.

If the pillars are smaller than the critical size discussed in Section 2.4.1, we can expect that the pillars reverse the magnetization by coherent mode described in Section 2.4.1. The switching field in coherent mode can be calculated by Eq. (2.6). By substituting H_{sw} in Eq. (4.34) with the right hand side of Eq. (2.6), we get the relationship between the pillar geometry and the critical spacing, expressed as

$$S_c = \sqrt[3]{4.25 \times \frac{r}{N_a - N_c}} \times d \tag{4.36}$$

Eq. (4.36) is useful when one wants to find out the maximum allowed pillar diameter, d, for a given recording density of the patterned media, indicated in spacing, S_c. For example, using the equation, we can calculate the required pillar diameter of the 100 nm period array. If we assume that the pillars can have an aspect ratio (r) of 2 and the safety factor of 20%, the maximum diameter of the pillar is 50 nm according to Eq. (4.36). This indicates that the diameter of the pillars in 100 nm period array should be smaller than 50 nm to avoid the serious interaction effect. The result was nearly the same for the aspect ratio of the pillars between 2 and 5.

Note that Co has M_s value about 3 times higher than that of Ni. Eq. (4.25) indicates that the interaction intensity is also three times that of Ni. Much tighter dimensions are

required for the Co pillar array.

4.7 Summary

In this chapter, we introduced a new scheme for the interaction field measurement using magnetic force microscope. The experimental measurement at such high recording density was performed for the first time. The measured values are in good agreement with numerical solution obtained from the dipole approximation of the demagnetizing tensor element. The result indicates that the strength of the interaction field is highly dependent on the diameter of the pillars as well as the distance between the pillars.

Chapter 5

Data Storage Based on Magnetic Force Microscopy

5.1 Introduction

In Chapter 3, we have presented the read/write method based on the magnetic force microscopy. The method was used in the read/write demonstrations on high density perpendicular patterned media. In Chapter 4, this method was also used in quantitative characterizations of the interactions between individual pillars. It is evident that the magnetic force microscopy has potential for a data storage at extremely high recording density. However, one of the key difficulties is its inherently slow scanning speeds. Also, the restricted scan area can limit the total data capacity of the potential data storage system. In current hard disk drives the data rate is roughly 10 Mbits/sec, several orders of magnitude higher than that of the SPM based system. One approach to closing such a big gap in data rate is to use parallel operation of multiple heads. In a parallel processing system, the data rate is increased in direct proportion to the number of probes in an array. In this chapter, we investigate the speed and other system level issues of data storage based on magnetic force microscopy. Various system design issues indicate the need for the parallel operation of many recording heads. We focus on the design of the parallel system that meets the performance requirements of today's HDD products.

Section 5.2 discusses the performance requirements of the MFM based data storage system by reviewing the specifications of current hard disk drives. The discussions are based on a few figures of merits used to describe the performance of a recording system.

Section 5.3 investigates four key design components that determine the speed of the MFM based data storage system. The limited performance of each component of current MFM is compared to that of HDD, and possible design optimizations and modifications are discussed. In Section 5.4, we discuss the sensing speed of MFM, thought to be the major limiting factor among the key components. Based on these foundations, Section 5.5 presents the design of a multiple head system operated in parallel. The performance of the proposed system in each category defined in Section 5.2 is discussed and the number of heads that meet the requirements is estimated. This section also focuses on the design of each single head, consisting of the cantilever with the magnetic tip and the integrated piezoelectric thin film actuator. The resulting design is evaluated with FEM analysis. Finally, in Section 5.6, we discuss a noble tracking method to center the tip on top of the pillar prior to the actual reading/writing process.

5.2 Performance Requirements

The performance of a recording system is usually described by a few performance parameters, namely capacity, access time, data rate and error rate. In the following section, the definition of each parameter is provided and the performance of the current HDD system is evaluated in each category.

5.2.2 Capacity

The data capacity of the recording system is defined as the amount of data immediately accessible to the drive from one media unit. It is usually specified in units of kbytes, Mbytes or Gbytes. The capacity of a media unit is simply the product of its recording area and areal data density. In HDD, the data are stored in circular tracks of the recording

magnetic disk. The areal data density is then given by the linear bit density along the in-track direction multiplied by the track density in the radial direction of the disk. In a magnetic recording system, the linear bit density is represented by the unit of bit per inch (BPI) while the track density uses the unit of track per pitch (TPI), representing the number of concentric tracks packed in one radial inch. Recently, the demonstration of a recording density of 11 Gbit/in^2 was reported by IBM[1]. The system has the linear bit density of nearly 360,000 BPI and the track density of about 30,000 TPI. In other words, a bit is stored in the area of 70 nm × 850 nm. Note that the track density is much smaller than the linear bit density. Such small track density is due to the inherent design of the mechanical structure of the hard disk drive. In HDD, the recording head slides on top of the rapidly rotating recording disk with a gap of 30 to 40 nm. To maintain such a small gap between the head and the disk, the mechanical arm that holds the head and the slider are designed in a limited range of stiffness. This results in the reduction of total bandwidth of the tracking servo and therefore the track density. In the optical recording system, the track density is comparable to the linear bit density because the head operates at a relatively large distance from the media.

5.2.2 Access Time

The access time is defined as the average time required to move the recording head from one data location to another and to begin reading or writing data. The access time is a combination of various drive motions and delays, as represented in the equation given by

$$t_{\text{access}} = t_{\text{seek}} + t_{\text{settling}} + t_{\text{latency}} + ... \tag{5.1}$$

Seek is the motion of the recording head in the radial direction of the disk to reach a new

[1] See their website at http://www.almaden.ibm.com.

data track. The seek time, t_{seek} in Eq. (5.1), is not simply proportional to the distance between an old track and a new track. Especially with high performance actuators, the head is being accelerated and decelerated during most of a seek motion. Furthermore, the seek process may not be a simple jump from one track to another. If many tracks should be passed in high speed, the tracking system may fail to keep a precise count of the tracks crossed by the recording head. After the simple jumping process, the tracking system reads the actual track address and performs zero or more fine seeks to reach the destination track. The delay for these fine seeks takes an important portion of the total seek time.

Settling is the delay time while transient tracking errors die down. The current servo bandwidths for the hard disk drive (HDD) fall in a range between 600 Hz and 750 Hz. The settling time then ranges from 1.3 to 1.7 msec. This is a significant portion of the access time for most drives. For Maxtor's Diamondmax 2880 drive, this amount explains a 15-20% of total access time. Currently, the research is conducted on silicon micro-machined actuators for higher bandwidth and precision of the tracking servo [78][79].

At the instant the correct track has been accessed and the servos have settled, the magnetic recording head could be located anywhere on the track. Latency is the delay time taken to rotate the correct sector into the location of the head. It depends only on the spindle speed of the drive. On average, half a rotation period, T/2, will pass before the desired sector comes around. For example, the Diamondmax 2880 drive has a spindle speed of 5,400 rpm. The average latency for this system is roughly 5 msec, which takes significant portion of the reported access time of the drive, 9 msec. Recently, the drives with higher spindle speeds, such as 10,000 rpm by Seagate Corp. And 12,000 rpm by Hitachi, have been introduced [80].

5.2.3. Data Rate

The data rate refers to the average speed at which bits on information are written on or read from the media. The data rate is different at each time the recording head finds a new track and begins reading or writing. With the constant spindle speed, the data rate is proportional to the radial distance between the current track and the disk center. For current commercial hard disk drives with a linear bit density of 240,000 BPI and a relative speed between the head and the disk of 30 m/s, the data rate is about 10 Mbits/s, nearly the speed of 10 X CD-ROM.

Data capacity, data rate and access time are actually closely linked. An increased spin speed may be desired if the access time is to be reduced. In such a case, the data rate must be increased proportionately in order to preserve the data capacity. Likewise, the data capacity may be increased by increasing the in-track density. Then the data rate must also be increased in order to keep access time constant.

5.2.4 Error Rate

The BER, or raw bit error rate, is defined as the fraction of bits in error. The BER of a hard disk drive can be measured by using some digital channel, usually referring to the drive's recording and reading channel without any special error correction system. The rate for the errors that slip through the error detection and correction (EDAC) system is called net error rate. Most commercial systems are designed to achieve a very low net error rate, usually lower than 10^{-13}. Such a high performance requirement indicates that the reliability will be one of the key concerns in SPM based data storage systems. It is, however, too early to discuss this issue in depth at a current stage of research and this parameter is not covered further in the chapter.

5.3 Speed Considerations

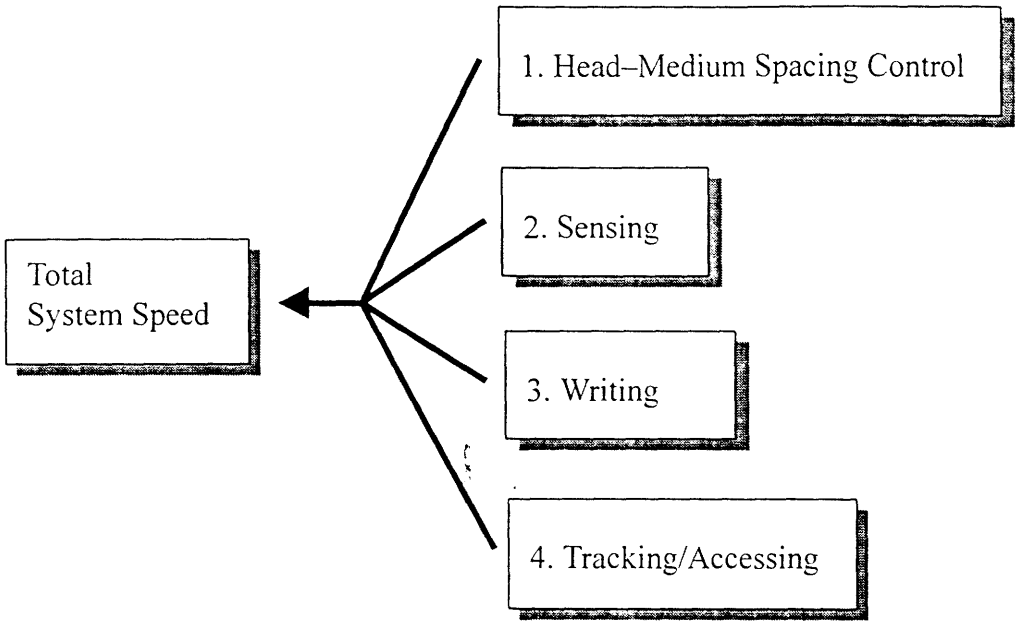

Figure 5-1 Four key design components that determine the overall speed of MFM based data storage system

In this section, we discuss the key design points of the data storage system based on magnetic force microscopy. There are four components that determine the speed of SPM data storage system. Those are, namely, the head-medium spacing control, sensing, writing, and track/accessing as shown in Figure 5-1.

5.3.1 Head-Medium Spacing Control

In data storage applications, a small gap between the probe and the sample should be maintained at a high relative speed, several orders of magnitude higher than the normal scanning speed of MFM. In a hard disk drive, the recording head is mounted on a small

ceramic slider. When the disk spins rapidly, the air bearing is generated by the air flow between the disk and the head. Current design of air bearing can provide a spacing between head and media of 30-40 nm at a relative speed of 30 m/s. The air film developed at the operating conditions must be thick enough to mitigate any asperity contacts, yet it must be thin enough to give a large read back signal. Note that the signal loss as a result of spacing can be decreased exponentially by reducing the separation between the head and the media. The key design point is the optimization of the disk roughness and lubrication scheme to avoid wear and minimize static (stiction) and dynamic friction. Zone laser textured disk is used to provide a durable, low stiction region for start and stop operation.

MFM needs a delicate gap servo mechanism because a sharp MFM tip can have a critical damage to both the medium and the tip when it accidentally contacts the surface. In MFM, a piezoelectric actuator is used to control the separation between the tip and the sample based on the topography information previously measured. This actuator usually has 7 to 8 kHz of resonant frequency and an actuation range of 5 to 8 μm. The gap is controlled within 50-150 nm above the topography. The MFM mode also requires a separate topographic scan that reduces the data rate by half. To avoid this, several methods can be considered.

- Pre-mapping: The complete topographic information of the medium is stored in a memory.
- One scan technique: This method runs in non-contact mode and uses the amplitude data as topographic data and the phase data as magnetic data. A good result is reportedly obtained[1].
- Extremely flat medium: It requires no or almost no topographic information to control the spacing between the head and the medium.

---

[1] See the application notes for magnetic force microscopy from Park Scientific Instruments.

- Separate sensor for topographic measurement: This method adds an extra sensor for the simultaneous topographic measurement during the magnetic scan mode.

Although it's difficult to say which method best suits the gap servo at this stage, these methods require a common technology to be improved. It is the speed of the actuator, controlling the spacing. The acquisition speed of the topographic data is in direct proportion to the speed of such an actuator. Currently a piezoelectric tube, responsible for the spacing control, has a resonant frequency of only about 7-8 kHz.

5.3.2 Sensing

The sensing component is responsible for picking up data signals from the storage media. In an HDD, a small inductive coil senses the flux change from the media. Recently, a much more sensitive head, called the magnetoresistive head, was introduced. The response speed of these heads is in the order of several nanoseconds, currently posing no limitation to the data rate of the hard disk. The sensing part of MFM consists of a small cantilever and a sharp magnetic tip attached at the end. The MFM measurement is usually performed in AC detection mode to achieve a high signal to noise ratio. Because this method is based on the mechanical motion of the cantilever, the sensing speed is much slower in nature. Recently, a cantilever with a resonant frequency of 1.3 MHz was reported [81].

5.3.3 Writing

A writing module records the binary data onto the media. A writing head in HDD consists of a coil mounted on the slider. The coil applies the field higher than the local coercivity of the media and therefore magnetizes the area along the preferred axis of the media. The speed of writing is comparable to that of reading in order of several nanoseconds.

There are a few approaches to writing bits using MFM technology. The most popular technique is to use a writing tip with a strong magnetic field and to place it near the bit location. For the reading, the tip with weaker field is used. This method requires the tip to be replaced every time the head switches the operation from reading to writing or vice versa. The method presented in Chapter 4 uses a coil to adjust the concentrated writing field near the tip. The current is applied to the coil at the instant the tip contacts the selected pillar in the patterned media and consequently the writing field magnetizes the pillar without affecting the states of other adjacent pillars. One scheme of writing a data stream on the media is to operate the magnetic probe in contact mode along a tack and send a short pulse to the coil at times the tip reaches the top center of target pillars. The speed of this writing method will be comparable to the speed of the topographic scan.

5.3.4 Tracking/Accessing

The tracking/accessing component is responsible for positioning of the head on the bit location before the head starts reading or writing. In HDD, a disk shaped medium with concentric tracks is rotated by a spindle motor while the recording head is positioned on the specified track by using the voice coil motor (VCM) to move the head in the radial direction. The tracking is performed based on the tracking data written on the media. The spindle motor used in current HDD can provide a rotation speed, up to 10,000 rpm and therefore the maximum relative speed between head and media is as high as 47 m/s at the outermost track. The bandwidth of a current commercial HDD tracking servo is between 600 Hz and 750 Hz with an average track density of 7,000 TPI. It's been reported that servo bandwidths greater than 2kHz is required to support a track density higher than 25,000 TPI [82]. Adding a second stage micro actuator with a much higher bandwidth was suggested to increase the bandwidth significantly.

MFM uses the piezoelectric actuator to move the probe in x, y and z directions. The piezoelectric material is used because of its known high resolution. The typical actuators used in commercial SPM provides a bandwidth of 1-2 kHz in in-plane direction, higher than that of HDD. However, their range is only about 100 μm by 100 μm in x and y directions and smaller than 10 μm in z direction. Note that in HDD, a single head covers the whole 3.5 inch media. Increasing the range by raising the actuation voltage to several hundred volts is ultimately limited by the breakdown voltage of the piezo actuator. In order to cover the required amount of data using MFM, a simultaneous operation of multiple probes should be considered [83-89].

5.4 Sensing Speed of MFM

Magnetic force microscopy is, most of the time, operated in AC detection mode to provide a high signal to noise ratio. AC mode senses the presence of a force gradient by detecting the resonance frequency shift of an oscillating cantilever. The cantilever, mounted on a piezoelectric actuator, is usually vibrated near its resonant frequency. The variations of the frequency are observed by measuring the change in the oscillation amplitude. Here, the sensitivity of the amplitude measurement has the following relationship with the force gradient, denoted as F′ [90].

$$\Delta A = \frac{2A_0 Q}{3\sqrt{3}k} F' \tag{5.2}$$

where A_0 is the original cantilever oscillation amplitude, Q is the quality factor, and k is the spring constant of the cantilever. In the equation, ΔA, defined as the variation of the oscillation amplitude, determines the sensitivity of the MFM. Note that ΔA increases with higher quality factor and lower spring constant of the cantilever.

If we model MFM as a simple second order lumped system, the response speed of

MFM depends on the resonant frequency and the damping ratio of the cantilever[1]. The settling time for the second order system is given by

$$t_x = \frac{4}{\xi \omega_r} \tag{5.3}$$

The equation indicates that the key to increasing the MFM speed is to develop a cantilever with higher resonant frequency. The resonant frequency of the cantilever can be increased by reducing the mass or by increasing the stiffness as indicated in the equation for the resonant frequency of the cantilever, given by

$$f_0 \approx \frac{1.03}{2\pi}\sqrt{\frac{E}{\rho}}\frac{t}{l^2} \tag{5.4}$$

where ρ is the density, E is Young's modulus, t is the thickness of the cantilever, and l is the length [91]. However, the stiffness of the cantilever should be kept constant because of the wear and the signal to noise ratio. Thus, the primary way to improve the performance is to reduce the cantilever mass. This can be performed by reducing the size of the cantilever. The spring constant of the cantilever and be kept constant even for small size cantilevers. This is indicated in the equation for the spring constant of the cantilever, given by

$$k = \frac{E\omega}{4}\left(\frac{t}{l}\right)^3 \tag{5.5}$$

where w is the width of the cantilever. With proper combination of the parameter, t, l, and w, the dimension for small cantilevers can be obtained. Many researchers worked on the fabrication of small cantilevers. A cantilever with a resonant frequency of 1.3 MHz and a spring constant of 3 N/m was fabricated [81][92]. Further reduction of the size was limited because the motion of smaller cantilevers was difficult to detect by optical means. Also, it was reported that the spring constant and the Q factor of these small cantilevers were

[1] This models the MFM operated in DC mode where the deflection of the cantilever, a direct measure of the force, is monitored.

difficult to control. They have a large effect on the reliability and the sensitivity of the magnetic imaging.

5.5 Design of Multiple Probe System

In this section, we discuss the design of a data storage system based on the multiple MFM heads operated in parallel. The performance requirements discussed in previous sections are used to determine the important design parameters such as the number of heads.

5.5.1 Concept of Proposed System

The proposed system has a PZT thin film unimorph actuator, represented as a micro-actuator in Figure 5-2 (a), responsible for the vertical motion of the tip. The actuator can provide a range of 7-8 μm and a resonant frequency of several hundred kHz. The deflection is monitored by the piezoresistive sensor. The horizontal motion relative to the media is

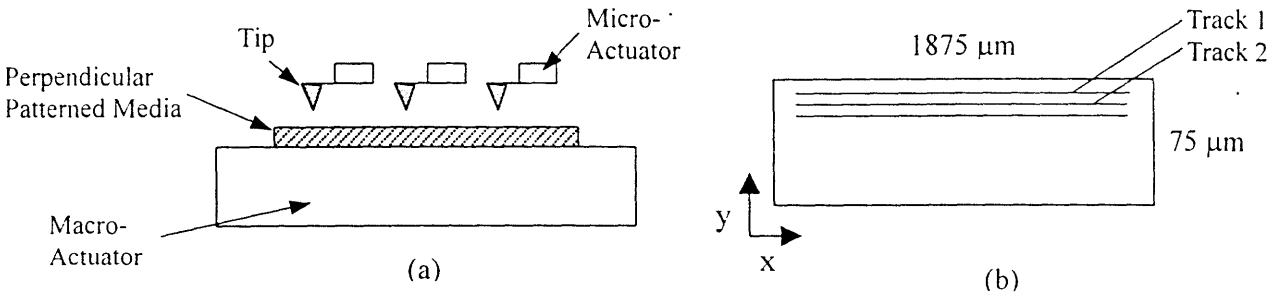

Figure 5-2 (a) Multiple tips with micro actuator for vertical motion and macro actuator for tracking and accessing motion. (b) The area covered by one single recording head.

provided with the macro-actuator consisting of piezoelectric stacks with flexures and closed loop sensors[1]. This actuator can provide a maximum scan area of 75 μm × 75 μm and the resonant frequency of 2 kHz. The resolution is reportedly 1 nm using a capacitive type sensor for the closed loop control. As a result, the hysteresis and other non-linearities are eliminated. The maximum applied voltage needed for this actuator is 150 Volt. The flexure is designed to provide the motion in x (in-track) direction with less damping effect so that it has a large amplitude at the resonant frequency. The bending amplitude of the flexure at resonance exceeds the normal amplitude at lower frequency inputs by the quality factor, Q, which can be as large as 1000. This would allow very large amplitudes even with the moderate Q value but the fracture limit restricts the maximum strain in the flexure to 10^{-3} to 10^{-2}. We chose the multiplying factor of 15. Therefore the actuator has a range of 75 μm in the direction perpendicular to the track (y) and 1,125 μm in the direction parallel to the track (x), as shown in Figure 5-2 (b).

During the reading operation, first, the topography of a track is measured by running contact mode. Then, along the same track, the deflection of the cantilever is recorded as the tip is made to follow the topography, being lifted 20-30 nm from the sample. The deflection is in direct relation to the magnetic force from the recorded bits and therefore the binary information stored in each pillar is read. The AC detection mode has a slow speed and complex detection circuits and therefore it is excluded from the design. Writing is performed by applying a field using the coil underneath the media while the tip is in contact with the pillar. During the writing process, the tip follows a track, operated in contact mode, and when it hits the top center of the pillar, the field is applied form the coil underneath the media.

Operation of an entire array of recording heads will require highly precise micromechanical manufacturing. The recent prototype of a micro-mirror display module

---

[1] We use the design and the specification of the piezoelectric actuator used in D3500 from DI.

developed by Daewoo Electronics Co., is noteworthy in this respect [93-95]. This module has a micro-fabricated 300,000 mirror array in which each mirror is actuated by a PZT unimorph actuator. Refer to Chapter 6 for further discussions on this technology.

5.5.2 Calculation of Data Rate and Number of Heads

In the following, the number of heads in an SPM based storage system is calculated to satisfy each of the three requirements discussed in Section 5.2.

1. Capacity (Goal: 10 Gbytes)

In the perpendicular patterned media with an areal density of 258 Gbits/in^2, there are 1,500 tracks with 22,500 bits per track inside the 1,125 μm × 75 um area covered by each recording head. To achieve the total storage capacity of 10 Gbytes, there should be 13 × 189 (***total 2457 heads***) heads in the system. The total storage area is then 1.46 cm × 1.42 cm.

2. Data Rate (Goal: 10 Mbits/sec)

The data rate of the parallel system with 2457 recording heads can be calculated as follows. First, the normal relative speed between the head and the media, represented as v_r is obtained by

$$v_r = l \times 2 \times f_{in} \rightarrow 4.5\,\text{msec} \tag{5.6}$$

where l is track length (1.125×10^{-3}) and f_{in} is the resonant frequency of the actuator in in-track direction (2 kHz). The resulting speed, shown on the right hand side of Eq. (5.6) is just slightly lower than that of the current hard disk drive. For the bit size of 50 nm, the data rate for each single head is then 90 Mbits/sec. Because the total number of heads is 2457, the total data rate is then ***221 Gbits/sec***, three orders of magnitude higher than the current

data rate.

According to the above results, the individual probe needs to read the data at a rate of 90 Mbits/sec. This requires the resonant frequency of the cantilever to have at least 90 MHz, which is practically difficult with current technology[1]. Note that a commercial MFM cantilever has a resonant frequency of 100 kHz, nearly three orders of magnitude smaller. A different approach can be taken to increase the range without having to run at resonant frequency. The increase in static motion range[2] of the macro-actuator in in-track direction can be achieved by reducing the resonant frequency. The resolution in this direction is not important as long as the relative speed from beginning to end is maintained constant to ensure the timing issues. With the cantilever having a resonant frequency of 100 kHz, the system can achieve 11.1 Gbits/sec, still much faster than current data rate. Because an extra topographic scan is needed for each MFM scan, we should divide the resulting data rate by two and therefore the final data rate is 5.5 Gbits/sec.

3. Access time (Goal: 5 msec)

According to the design of the macro-actuator, the resonant frequency in y direction is 2 kHz. Therefore, the seek time and the settling time in Eq. (5.1) can be calculated using Eq. (5.3). The total of the two is 450 μsec. Latency time depends on the in-track speed. If 2 kHz of the actuator resonant frequency is assumed, the time it takes to travel one track is 250 μsec. The average latency time is then 125 μsec. The total access time for a single recording head is therefore 575 μsec. The average access time for the parallel system with 2457 heads can be estimated to be ***0.23 μsec***, which by far surpasses the access time of current HDD. If we have reduced the resonant frequency to 10 Hz for the purpose of increasing the range, then the latency time of single head is increased to 25 msec. But, again, the total access time is only about 5.27 μsec.

---

[1] Refer to Section 5.4.
[2] it indicates the DC gain in frequency response plot.

5.3.3 Design of Single Head

In the previous chapter, we learned that the response speed of each recording head is the key element in the multiple probe system design. In this section, the design of the single head, consisting of a cantilever with integrated actuator and sensor is discussed. Typically, the actuator used in commercial AFM/MFM products consists of a tube or stack, which exhibits relatively low resonant frequencies around 7-8 kHz in vertical direction, limiting the scanning speed. The speed can be increased considerably by integrating a thin layer of piezoelectric material on the base of the cantilever. Quate et al. fabricated a cantilever, containing integrated actuator and sensor with a bandwidth of 20 kHz. A thin layer of ZnO is deposited on the base of a piezoresistive Si cantilever. The maximum deflection of this cantilever was 2 μm reportedly [85]. Xu et al. used electrostatic forces in a comblike structure for three dimensional motion of the tip [96]. Watanabe et al. used lead zirconate titanate (PZT) films deposited on single cantilevers in conjunction with an optical sensor for the deflection measurement [97]. ZnO is one type of piezoelectric material that can be readily incorporated into a microfabrication because it doesn't require a high temperature process. Also, it shows less hysteresis behavior than other piezo materials. However, because of its low piezoelectric constant, it does not have enough motion range to become practical. PZT, on the other hand, has a larger motion range. However, integrating PZT thin film into the cantilever is a challenging task because it requires high temperature processes and is very sensitive to the chemical environments.

Each head in the proposed system consists of a triangular piezoresistive cantilever with a magnetic tip at the end and an integrated PZT thin film actuator on the dual leg rectangular beams. During the topographic scan, the PZT actuator deflects the cantilever to maintain the constant force on the sample and thus to follow the sample topography. The contact mode is the preferred scanning method to other AC mode detection modes since the

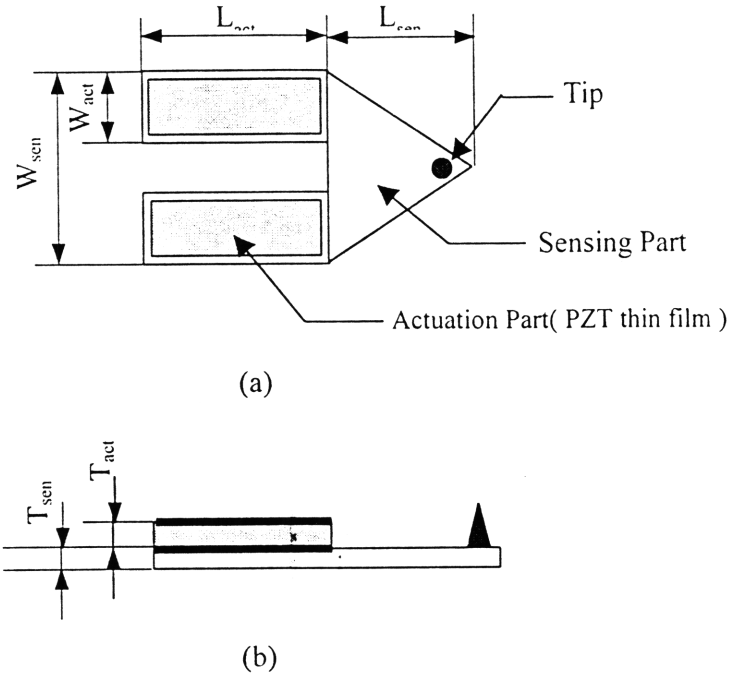

Figure 5-3 Schematic of the cantilever with integrated sensor and actuator (a) Top view (b) Side view

loading force on the tip can increase the response speed of the tip by a significant amount and therefore allow a higher data rate. The force between the tip and the sample deflects the sensor part of the cantilever and the deflection is monitored by measuring resistance changes in the piezoresistor layer. This type of sensor is preferred to the optical levers because it simplifies the design and the operations, necessary in the parallel system. Adding and aligning a laser sensor for each of 3,000 probes is practically impossible. In the next scan along the same track, the tip is lifted 20-50 nm above the sample surface and the deflection of the cantilever is monitored. This time, the long range magnetic force acts on the magnetic tip and deflects the cantilever. The deflection is the direct measure of the magnetic force and thus the magnetization state of the bits are read.

The maximum scan rate is determined by the performance of both the sensing and the actuation part of the cantilever. The bandwidth of the PZT thin film actuator should be

raised to maximum while the deflection range of 7-8μm is maintained to accommodate the roughness and possible mis-orientation of the sample. The spring constant of the actuation part should be high enough to eliminate the effect of the sample force. On the other hand, the sensor part of the cantilever should have a spring constant, lower than 1, to reduce the wear of the tip and to prevent possible damages on the tip and the sample during the contact. When the magnetic field is to be measured, the spring constant of the sensor part should be carefully chosen so that no other forces near the sample such as van der Waals force have effect on the cantilever deflection.

We have tried a few geometries of the cantilever shown in Figure 5-2 to find out the design that best meets the requirements above, first using the design formula and then proving it with finite element method (FEM) simulations. The actuator part of the probe consists of Si rectangular cantilever and a thin film PZT actuator sandwiched by two metal layers as electrodes. The sensing element of the probe is the triangular part of the cantilever shown in Figure 5-2, consisting of the Si layer and the tip at the end. Because each part of the cantilever requires different specifications, two are designed separately. The following is the formula used in the design.

- Resonant frequency as a function of the cantilever length and thickness, represented in Eq. (5.4)
- Spring constant as a function of the cantilever width, thickness and length, represented in Eq. (5.5)
- Deflection as a function of the cross section geometry of the cantilever and length: Here, we used the experimental data obtained from the test structure consisting of poly-Si cantilever with integrated PZT thin film actuator. In the cantilever, the PZT film actuator had a thickness of 0.4 μm, a length of 75 μm and a width of 25 μm. The poly-Si layer had the same dimensions. The maximum deflection of these cantilevers were

measured to be 10 μm when 15 Volts was applied to the piezo[1]. Based on these data, we could estimate the deflections of the cantilevers with a different geometry. For example, when the length of the cantilever, both the Si and PZT layer, is increased, we can predict that the deflection increases by its square. Also, when the cross section geometry of the Si layer changes, the deflection change is proportional to the bending moment of inertia.

From the above formula, we used the following strategy to design a high speed MFM cantilever. To raise the resonant frequency of the cantilever, starting from the dimension of the test structure, we decreased the length of the cantilever. This is because it is known that the resonant frequency of the cantilever is most sensitive to the length. To compensate for the deflection loss, the thickness of the cantilever was decreased. The width of the cantilever is in no relation to the resonant frequency of the cantilever and therefore has a less important role in the design process. This results in the reduction of the overall size of the cantilever. However, the size couldn't be reduced smaller than the fabrication limit and the minimum area for the sensor detection. The resulting design has the dimension of L_{act}=30 μm, W_{act} = 25 μm, T_{act} = 0.4 μm, L_{sen} = 40 μm, W_{sen} = 58 μm and T_{sen} = 0.3 μm in Figure 5-3.

The finite element method analysis was performed on the design. The material constants used in the simulation were E = 170 Gpa, ρ = 2330 kg/m^3, and ν = 0.25 for Si and E = 45 Gpa, ρ = 2330 kg/m^3, and ν = 0.25 for PZT. We modeled first only the actuation part of the cantilever as shown in Figure 5-4 (a) and found that the first mode resonant frequency was 475 kHz, an order of magnitude higher than previously reported numbers. For the same model, the length of the cantilever was varied and the resonant frequency was obtained. As expected, the first mode resonant frequency varied in proportion to the square

[1] This work was done in the TMA (Thin film Mirror Array-actuated) research center at Daewoo Electronics Corp.

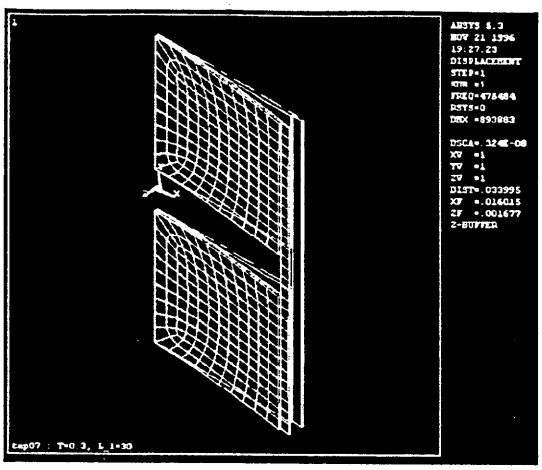

(a)

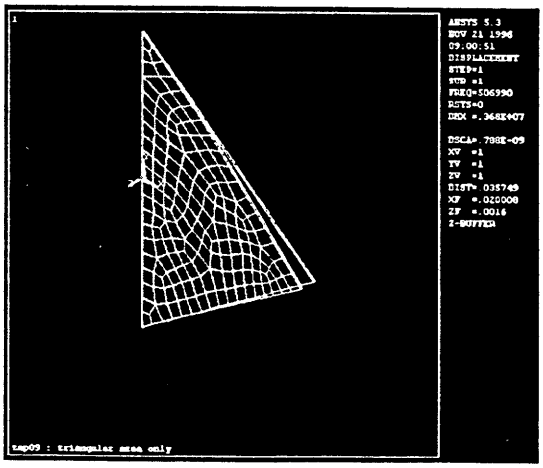

(b)

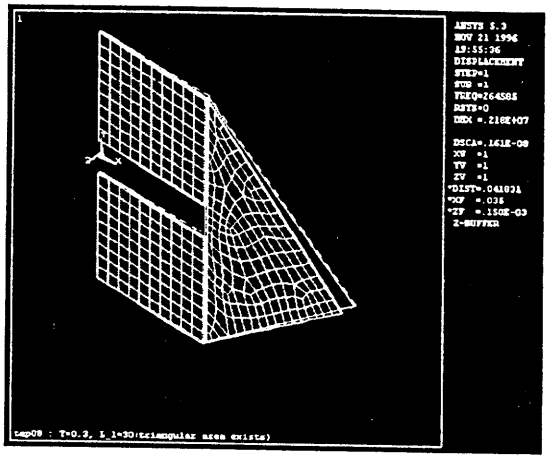

(c)

Figure 5-4 (a) The FEM model of the actuation part of the cantilever; number of nodes: 3834, number of elements: 948, 1st mode natural frequency: 475 kHz, 2nd mode natural frequency: 671 kHz (b) The sensing part of the cantilever; number of nodes: 1223 number of elements: 310, 1st mode natural frequency: 507 kHz, 2nd mode natural frequency: 1.76 MHz (c) The whole cantilever; number of nodes 3433 number of elements: 852, 1st mode natural frequency: 265 kHz, 2nd mode natural frequency: 622 kHz

of the cantilever length. The model for the sensing part of the cantilever is shown in Figure 5-4 (b). The first mode resonant frequency was 507 kHz and the spring constant was 0.8, which meets the requirement for the sensing part. Figure 5-4 (c) shows the model of the whole cantilever when the two parts of the cantilever are attached to each other. As predicted, the resonant frequency dropped to 265 kHz. However, the number is still significantly higher than that of the piezo tube or stack.

As mentioned before, the fabrication of these probes, especially in an array, is challenging because of the difficulties in integrating PZT materials into the process. However, the recent progress in TMA research, currently underway at Daewoo Electronics, shows the good potential of this technology. The fabrication of the above model is currently being conducted.

5.6 Single Bit Tracking

5.6.1 Introduction

One of the important advantages of patterned media is that each bit is stored in a precisely located single magnetic domain particle. During the writing process, the read/write head moves to the bit and simply flips the polarity of the particles. The errors due to the head misalignment or the previous written marks that are not completely erased, found in thin

film media, don't exist in the patterned media. Also, in the patterned media, each bit is separated from the neighboring bits by a non-magnetic material. This provides a physical boundary between the pillars. The read/write head can detect the boundary and find out the precise location of the bit without separate tracking data.

When writing with PMR technique or any other techniques, the user should be able to move the head to the specified bit and keep it centered on top of the bit while the writing field is applied. In the following work, a tracking algorithm that best exploits the advantages of the patterned media is proposed. A demonstration of a single bit tracking based on this algorithm is performed by the simulation.

Section 5.6.2 presents a tracking algorithm that can be implemented in MFM based data storage. By using this method, the MFM probe can be positioned onto the top center of the bit at a fast rate. A computing mechanism of this tracking method is provided for the future implementation in a digital controller. In Section 5.6.3, a theoretical model of the interaction force between the MFM probe and the pillar is presented. The model is used to simulate a response of the reading head to the magnetic fields from the pillars on the media. Section 5.6.4 discusses the simulation results of the tracking algorithm proposed in Section 5.6.2. The simulation was performed using Matlab software. In the simulation, the optimal operating conditions were found by running the simulations with various operating parameters.

5.6.2 Tracking Algorithm

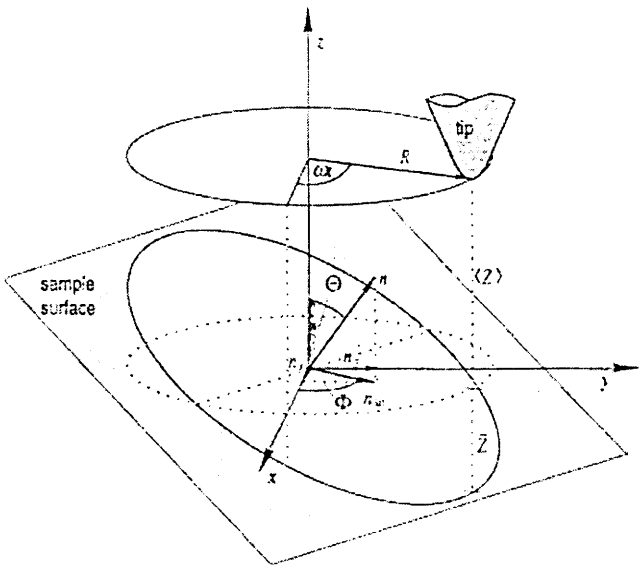

Figure 5-5 The Tracking Motion of the Tip with Respect to the Sample Surface

The tracking algorithm is based on the tracking mode theory described by Pohl et al. [98]. Previously, such an algorithm was used in tracking the topographic features in two-dimensional grating with the scanning tunneling microscope. In their method, a sinusoidal offset voltage is applied to the x and y signals of the scanning tube with a phase shift of 90 degrees causing a circular motion of the tip. Such a motion of the tip results in a variation of the sample-tip separation Z around its average value <Z>, shown in Figure 5-5. If the sample surface is assumed to be flat, a sinusoidal output will be obtained from Z. The change in distance with respect to <Z> denoted as $\tilde{Z}$, can be calculated from the following equation

$$\tilde{Z} = Z - \langle Z \rangle = R \cdot \cos(\omega \cdot t - \Phi) \cdot \tan\Theta \tag{5.7}$$

Each of the parameters used in Eq. (5.7), R, ω, t, Φ and Θ, are defined in Figure 5-5. Φ and Θ are the unknown parameters that should be computed from the measured $\tilde{Z}$ and other given parameters. Φ and Θ are calculated by using the following numerical method. First, the area inside the circular path of the tip is divided into four quadrants and, in each quadrant, the integral of $\tilde{Z}$ is performed. These integrals can be simplified as follows.

$$\int_0^{t_1} \tilde{Z}dt = R \cdot \tan\Theta \int_0^{t_1} \cos(\omega \cdot t - \Phi)dt \tag{5.8}$$

$$= R \cdot \tan\Theta \int_0^{t_1} \{\cos(\omega \cdot t)\cos\Phi + \sin(\omega \cdot t) \cdot \sin\Phi\}dt$$

$$= R \cdot \tan\Theta \left\{\cos\Phi \int_0^{t_1} \cos(\omega \cdot t)dt + \sin\Phi \int_0^{t_1} \sin(\omega \cdot t)dt\right.$$

$$= R \cdot \tan\Theta \left\{\cos\Phi\left(\frac{1}{\omega} \cdot \sin(\omega \cdot t)\right)\Big|_{t_0}^{t_1} - \sin\Phi\left(\frac{1}{\omega} \cdot \cos(\omega \cdot t)\right)\Big|_{t_0}^{t_1}\right\} \tag{5.9}$$

From Eq. (5.9), we can calculate the integrals in each quadrant as follows.

$$\tilde{Z}_1 = \int_0^{\frac{\pi}{2}\omega} \tilde{Z}dt = R \cdot \tan\Theta \left\{\cos\Phi\left(\frac{1}{\omega} \cdot \sin(\omega \cdot t)\right)\Big|_0^{\frac{\pi}{2}\omega} - \sin\Phi\left(\frac{1}{\omega} \cdot \cos(\omega \cdot t)\right)\Big|_0^{\frac{\pi}{2}\omega}\right\} \tag{5.10}$$

$$= R \cdot \tan\Theta \left\{\cos\Phi \cdot \frac{1}{\omega} \cdot \left(\sin\left(\frac{\pi}{2}\right) - \sin(0)\right) - \sin\Phi \cdot \frac{1}{\omega} \cdot \left(\cos\left(\frac{\pi}{2}\right) - \cos(0)\right)\right\}$$

$$= \frac{R\tan\Theta}{\omega}\{\cos\Phi + \sin\Phi\} \tag{5.11}$$

$$\tilde{Z}_2 = \frac{R\tan\Theta}{\omega}\{-\cos\Phi + \sin\Phi\} \tag{5.12}$$

$$\tilde{Z}_3 = \frac{R\tan\Theta}{\omega}\{-\cos\Phi - \sin\Phi\} \tag{5.13}$$

$$\tilde{Z}_4 = \frac{R\tan\Theta}{\omega}\{\cos\Phi - \sin\Phi\} \tag{5.14}$$

By adding Eq. (5.11) and Eq. (5.12) and subtracting Eq. (5.13) from Eq. (5.14), we get

$$\tilde{Z}_1 + \tilde{Z}_2 = \frac{2 \cdot R \tan\Theta}{\omega} \cdot \sin\Phi \tag{5.15}$$

$$-\tilde{Z}_3 + \tilde{Z}_4 = \frac{2 \cdot R \tan\Theta}{\omega} \cdot \cos\Phi \tag{5.16}$$

By dividing Eq. (5.15) by Eq. (5.16), we get the following equation for Φ.

$$\Phi = \arctan\left(\frac{\tilde{Z}_1 + \tilde{Z}_2}{-\tilde{Z}_3 + \tilde{Z}_4}\right) \tag{5.17}$$

Also, Θ can be calculated from Eq. (5.15).

$$\Theta = \arctan\left(\left(\tilde{Z}_1 + \tilde{Z}_2\right)\frac{\omega}{2R} \cdot \frac{1}{\sin\Phi}\right) \tag{5.18}$$

where, $\tilde{Z}_1$, $\tilde{Z}_2$, $\tilde{Z}_3$ and $\tilde{Z}_4$ are the integrals of $\tilde{Z}$ with respect to time in each of the four quadrants in the scanning area. Angle Θ indicates the orientation of the sample surface with respect to the xyz coordinates, shown in Figure 5-5. On the other hand, the angle Φ represents the direction of the steepest slope on the sample plane. The n_{lat} in Figure 5-5 denotes the vector, pointing in this direction with respect to xyz coordinates. The basic algorithm of this tracking method is to move the tip in the direction of n_{lat} until the angle Θ is reduced to 0. When Θ becomes 0, the center of the tip rotation is exactly on the top of the local maximum. Also, moving the tip in the direction opposite to n_{lat} will lead to the local minimum.

Although Pohl et al. used this algorithm to track topographic features of the sample, the same method can be applied to a tracking of magnetic features. The MFM images taken by others show that the magnetic field from a single domain pillar forms a local maximum or minimum near the center of the pillar, although the measurement noise obscures the patterns in these pictures. In the simulation, we also introduced the noise factor to the reading image and studied the dependence of the tracking performance on the

noise level.

5.6.3 Modeling of Magnetic Force Microscope

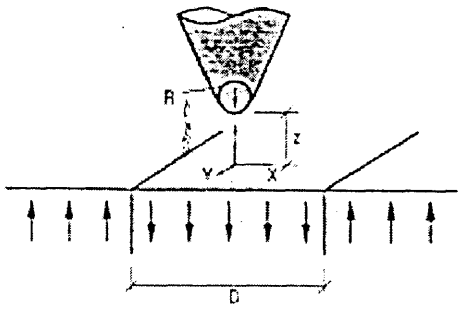

Figure 5-6 MFM Tip and the Sample

In the proposed system, the tracking is performed based on the signals from a magnetic force microscope. In order to simulate the response of MFM to the pillar fields, a model similar to one suggested by Saenz et al. [99][100] is used. Figure 5-6 shows the schematic of a MFM model used by Saenz et al. In their model, the magnetic forces were estimated by assuming a direct dipolar interaction between the permanent magnetic moments, M_1 and M_2 per unit volume of the tip and sample, respectively. For an isolated strip-like domain as seen in Figure 5-6, this force is given by

$$F \cong F_0 \cdot \left(\frac{(x+d/2)}{(x+d/2)^2+(z+1)^2} - \frac{(x-d/2)}{(x-d/2)^2+(z+1)^2} \right) \tag{5.19}$$

where

$$F_0 = \frac{16\pi}{3} \cdot M_1 \cdot M_2 \cdot R^2 \tag{5.20}$$

And the dimensional parameters are defined as

$$\begin{aligned} x &= X / R \\ d &= D / R \\ z &= Z / R \end{aligned} \tag{5.21}$$

It can be assumed that D is the diameter of the pillar in patterned media. Because the MFM are based on the detection of the phase change of the vibrating cantilever, proportional to the force gradient of the sample, the equation is obtained by differentiating Eq. (5.19) with respect to z. The result is

$$\frac{dF}{dz} \cong \frac{F_0}{R} \cdot \left(\frac{-2 \cdot (z+1)(x+d/2)}{\left((x+d/2)^2 + (z+1)^2\right)^2} - \frac{-2 \cdot (z+1)(x-d/2)}{\left((x-d/2)^2 + (z+1)^2\right)^2} \right) \tag{5.22}$$

In Figure 5-7, the force gradient as a function of the distance x is shown. This is a signal one would expect from the typical MFM data on top of a pillar. In the plot, the tip radius was 25 nm and the distance between the sample and the tip was 35 nm. Also, the pillar diameter was 100 nm.

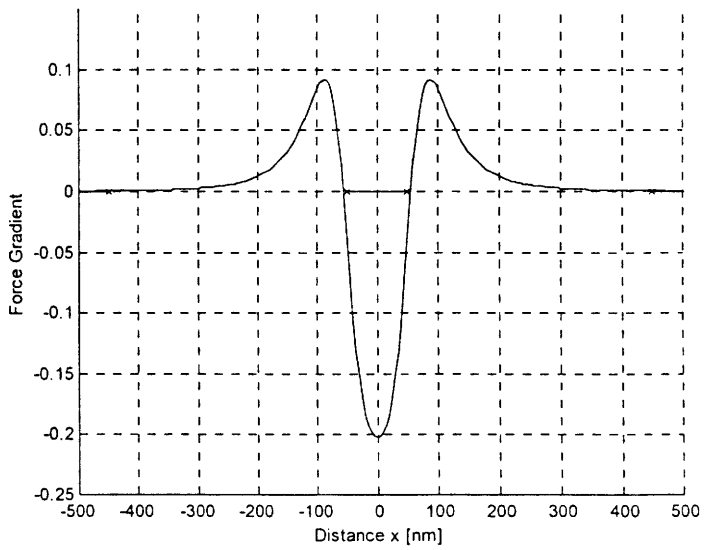

Figure 5-7 Force Gradient vs. Distance $_X$

As predicted, the plot shows a local minimum of the force gradient at the center of the pillar. Also, we can observe two local maxima on both sides the bit. If looking at the pillar from the top, these maxima form a band around the pillar. This type of pattern was observed in the MFM images.

5.6.4 Simulation of Single Bit Tracking

The tracking simulation is performed on a two-dimensional pillar array. Eq. (5.22) is expanded to a two-dimensional model by introducing a y component of the force gradient. The resulting equation is expressed as

$$\frac{dF}{dz} \cong \frac{F_0}{R} \cdot \left(\frac{(z+1)^2 - \left(\sqrt{x^2+y^2} + d/2\right)}{\left(\left(\sqrt{x^2+y^2} + d/2\right)^2 + (z+1)^2\right)^2} - \frac{(z+1)^2 - \left(\sqrt{x^2+y^2} - d/2\right)}{\left(\left(\sqrt{x^2+y^2} - d/2\right)^2 + (z+1)^2\right)^2} \right) \quad (5.23)$$

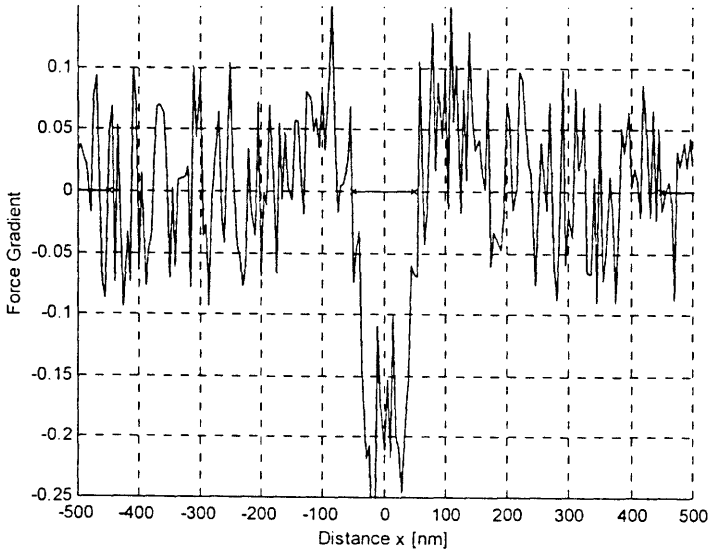

Figure 5-8 Force Gradient Curve with Added Noise

In a typical MFM image, one can find the effect of the noise, depending much on the environment, and therefore the images as clean as those shown in Figure 5-7 are difficult to obtain. To simulate the real MFM data more precisely, we introduced a noise factor into the model by implementing a random number generation feature of Matlab software. An example of force gradient data with the added noise is shown in Figure 5-8.

The simulation of the proposed tracking mode was performed based on these equations. In the simulation, the important tracking parameters were the radius of a circular path followed by the tip, the size of the step taken by the tip at each rotation, and the frequency ratio, S_f, which indicates how fast the tip rotates. The above simulation was performed using the Matlab software.

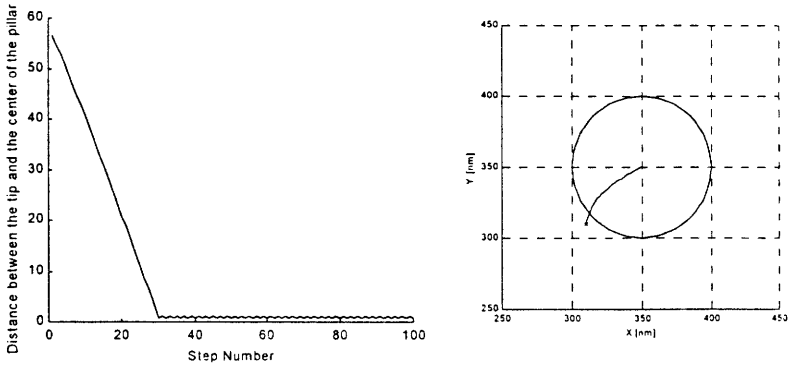

(a) Noise Level : 0 %

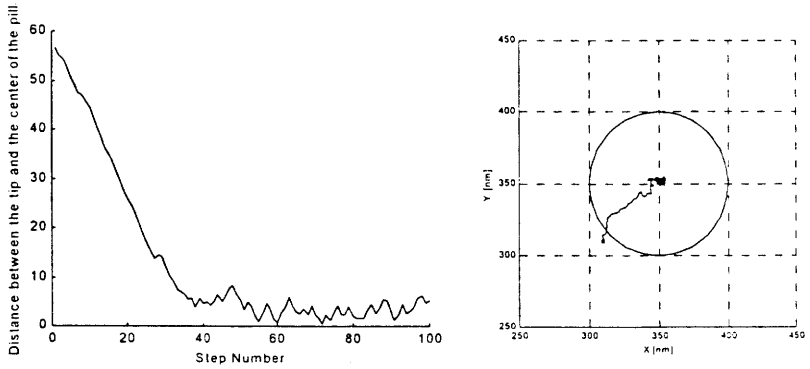

(b) Noise Level : 200 %

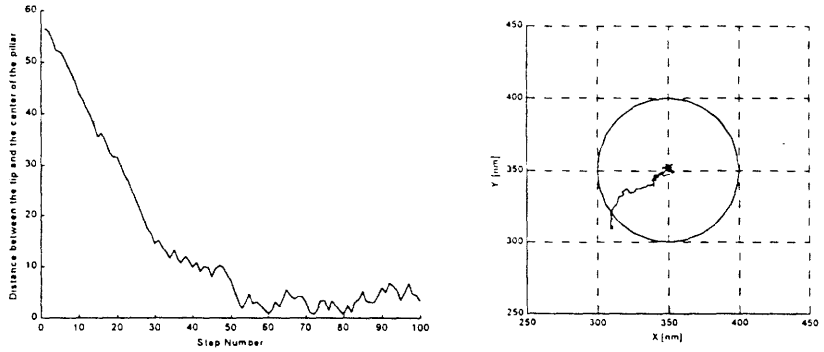

(c) Noise Level : 300 %

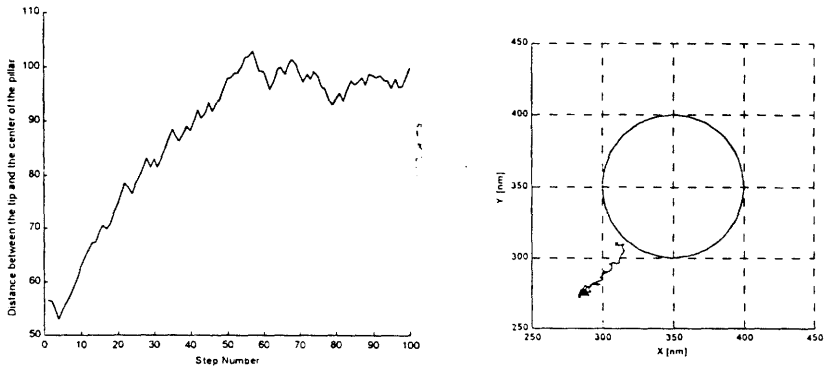

(d) Noise Level : 400 %

Figure 5-9 Effect of Noise

- Effect of Noise

The tracking performance was observed under an increasing level of noise. In the simulation, it is given that R = 50 nm, n_{step} = 2 and s_f = 50. The resulting graphs of the tracking simulation are shown in Figure 5-9. In the figure, the two types of diagram are depicted to show the effect of the noise. The figures on the right column show the motion of the tip on the sample plane during the tracking. As one can see in the right picture of Fig. 5-9 (a), the tip starts from the initial position, marked as x in the figure, and moves towards the center of the pillar, depicted as a circle. The figures in the first column of Figure 5-9 show the distance between the tip and the center of the pillar as a function of the step number, representing the tracking time. As the noise level increases, the time for the tip to reach the 0 distance from the center increases and, eventually, with a noise level higher than

400%, the tip cannot find the center of the pillar, as seen in Figure 5-9 (d). Also, with an increasing noise, the larger oscillations of the tip were observed after it reached the center of the pillar. However, they were not very significant till the noise level reached 400%. For a noise level of 300%, the tip reached the pillar center after 50 steps and tracked the center within 10 nm, which is still sufficient to ensure a successful writing process.

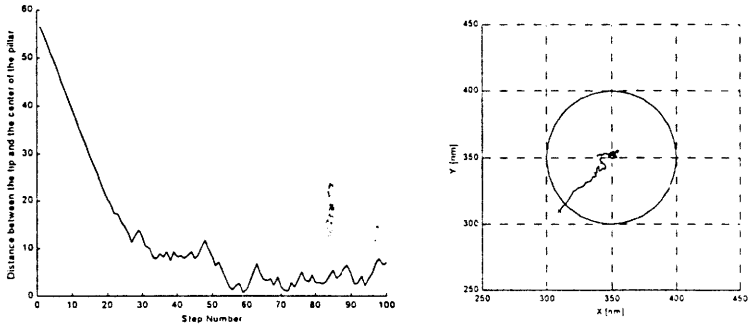

(a) Radius of the Tip Motion: R = 10 [nm]

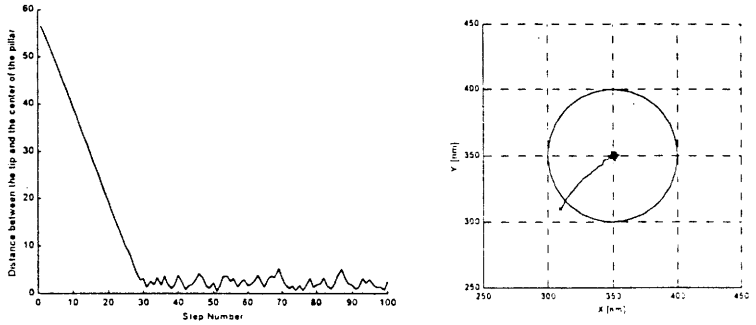

(b) Radius of the Tip Motion: R = 30 [nm]

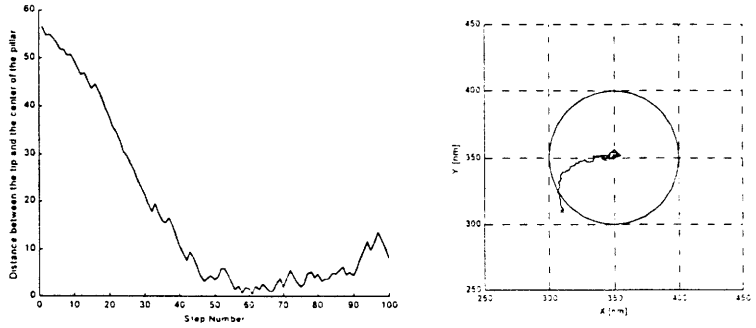

(b) Radius of the Tip Motion: R = 80 [nm]

Figure 5-10 Effect of the Radius of Tip Motion

- Radius of Circular Tip Motion (R)

Here, the effect of the radius of the tip rotation on the tracking performance was examined. In Figure 5-10, the plots with similar format were shown, for three different radiuses, 10 nm, 30 nm, and 80 nm. The best result was obtained with the radius between 30 nm and 50 nm. As shown in Figure 5-10 (b), the tip takes a near straight route to the center and stays centered within 5 nm. On the other hand, with a smaller radius of 10 nm, a small detour of the tip towards the center was observed. A deviation of more than 10 nm was observed, probably because the variations of the magnetic field, $\widetilde{Z}$, at this radius was comparable to the noise level and therefore the tracking were much sensitive to the noise. Similar results were obtained at the radius of 80 nm as shown in Figure 5-10. In the figure, the tip finds rather a long path towards the center of the pillar, probably because the fields from several bits are measured due to the large radius of the tip motion. The result indicates that the optimum size of the radius is close to the size of the pillar.

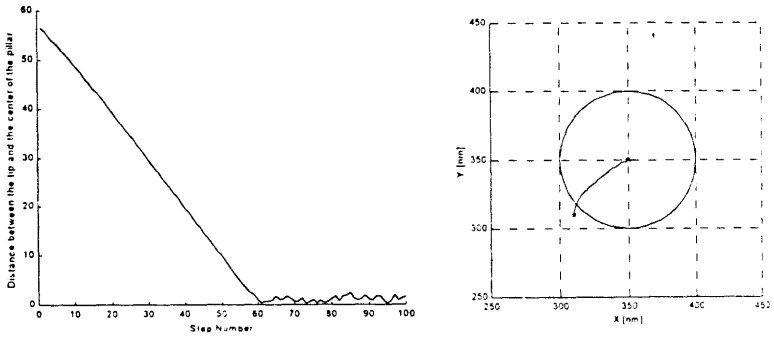

(a) step size n_{step}=1

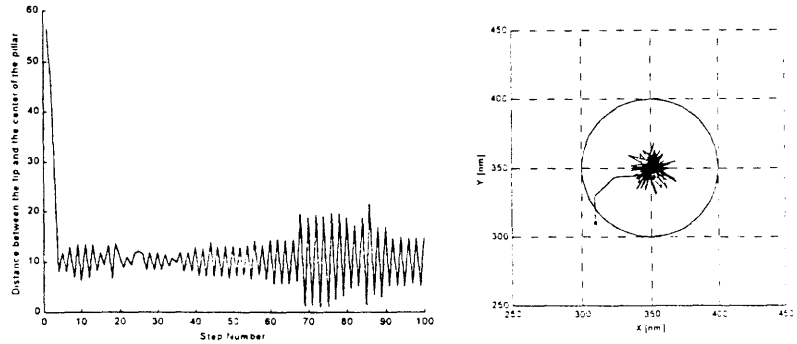

(b) step size n_{step}=20

Figure 5-11 Effect of Step Size

- Step Size (l_{step})

l_{step} defines the step size, taken after each circular motion of the tip. The effect of different l_{step} on the tracking behavior was observed in Figure 5-11. The effect of the step size is apparent in Figure 5-11 (a) and (b). With a small step size, the time for the tip to reach the pillar center was much increased, but the deviation from the center, after the tip found the pillar, was reduced. On the other hand, a large step size resulted in the fast approach to the center. However, the tip was not well kept centered to the pillar as shown in Figure 5-11 (b). More efficient method such as the control of the l_{step} adaptively at each stage of the tracking should be implemented in order to optimize the tracking performance.

- Frequency Ratio (S_f)

S_f is defined as the frequency ratio between the sampling frequency and the rotation frequency of the probe. Larger S_f means that more data points have been taken for each

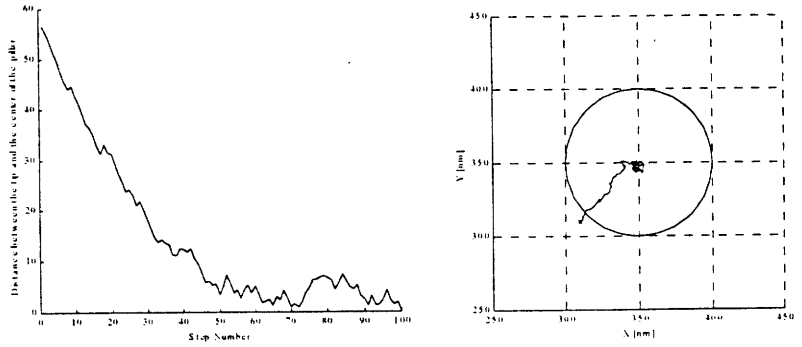

(a) S_f=5

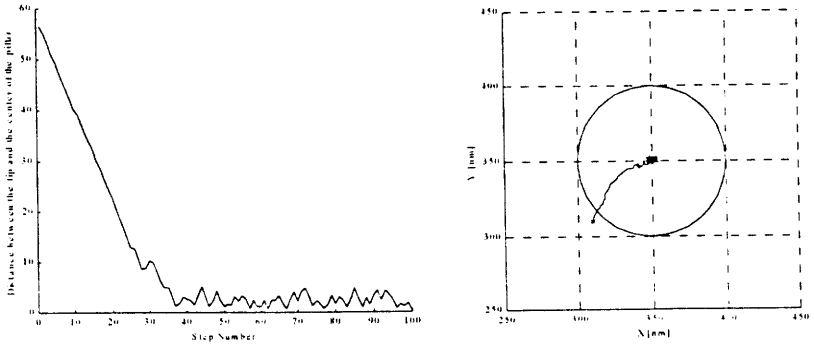

(b) S_f=50

Figure 5-12 Effect of Frequency Ratio

rotation of the probe. Figure 5-12 shows the effect of the frequency ratio, S_f, on the tracking performance. With a lower frequency ratio, it is apparent that the deviation of the probe from the center is increased. The higher magnitude of the oscillations at the center of the pillar is visible in Figure 5-12 (a). For the higher S_f, shown in Figure 5-12 (b), the tracking performance was much improved. This is because more data were used to average out the noise effect and therefore the accuracy of the tracking increased.

In the following paragraph, the implications of this method in multiple bit tracking are discussed. We begin by introducing the factor of the sampling frequency because it has an important implication on the performance of a digital controller, probably implemented in the proposed tracking system. In order to meet the current data rate of the hard disk, around 10 Mbits/sec, the tracking of each single bit should be performed in 100 nanoseconds. In Figure 5-12 (b), we have seen that the probe reached the center of the pillar in approximately 30 steps with an optimum set of tracking parameters. Consequently, the required frequency of the tip rotation is 300 MHz. From the simulation, the smallest frequency ratio that guarantees a good tracking performance was around 10. Therefore, the resulting required sampling frequency is 3 GHz. Currently, the A/D converter with such sampling rate is not available. For the proposed method to be implemented in multiple bit tracking, the algorithm should be modified so that the positions of multiple bits or a track of bits are found in one cycle of the tip motion.

5.7 Summary

In this chapter, we discussed the practical issues of implementing SPM/MFM technology in data storage systems. First, the performance requirements were reviewed based on the survey of current specifications of HDD products. Four key issues regarding the design of a high speed SPM system were presented and possible solutions were discussed. One of the

solutions to increasing of a SPM detection speed was to design a small cantilever with integrated actuator and sensor and to build a multiple head system, operated in parallel. According to the calculations, provided in this chapter, a total of 2457 heads were needed to meet the performance requirements. Lastly, we have proposed a tracking method of the individual bits of perpendicular patterned media and performed simulations to study the effect of various tracking parameters. The result was useful in demonstrating the advantages of the patterned media and potentials to be implemented in real systems.

Chapter 6
Conclusions

By using a point magnetic recording process, we were able to record the bits at a recording density of 16 Gbits/in^2 on perpendicular patterned media, consisting of Nickel pillars with a diameter of roughly 90 nm and an aspect ratio of 2. Recording of smaller bits is expected to be possible if the sample with proper pillar geometry can be provided.

In this thesis, we also found out that the read/write process using the bias field of the coil and the stray field of the tip possesses a good potential not only in high density data storage but also in the characterizations of media properties. By using this method, we could obtain the quantitative data for the interaction field between the pillars with a spacing as small as 200 nm. There are two key factors that made the measurement possible. One is that a field could be applied to the target bit without affecting the adjacent bits. The other is that the exact writing field applied to the pillar could be measured.

The results of the switching field measurement in Chapter 2 indicate that the Ni pillars are mostly single domains and follow closely the behavior to the curling mode switching. We showed that the average switching field from the measurement is within the range predicted by the curling mode theory. This is confirmed by the discussions in Section 2.3.5 where we observed that the aspect ratio of the pillar does not affect the switching field. The measurement results showed a non-uniformity of the switching field in the pillar array , up to a level that is fatal to the high density data storage application. An improved fabrication method should be proposed.

The interaction field model in Chapter 4 implies that the interaction can be a serious problem in high density perpendicular patterned media. For a 100 nm period array,

when the pillar diameter is larger than 50 nm, serious interactions between pillars are expected to occur. We provided a simple equation to estimate the maximum possible pillar diameter for a given spacing.

In order to increase the data rate of the proposed read/write scheme, one has to deal with four factors described in Chapter 5. The requirements on those factors indicated that the system should be designed in the form of multiple read/write heads operated in parallel. This system is based on magnetic force microscopy. We found that almost 2,500 heads are needed to achieve the data capacity of 10 Gbytes. However, we found that the data rate and the access speed for this system are much faster because of the large number of heads. The next step that follows this thesis work is the actual fabrication of the multi-probe system. The fabrication of a single cantilever with an integrated PZT actuator and sensor is currently underway at Daewoo Electronics Co. Prior to this research, a prototype of thin film mirror array (TMA) module was developed at Daewoo. This module consists of 300,000 small mirrors of 97 μm by 97 μm in size. Each mirror is tilted with a maximum angle of 4° by unimorph piezoelectric actuator, just like in the design proposed in this thesis. The current fabrication technology for such mirror array allows every single one of the 300,000 mirrors in the module to tilt accurately, following its own input signal. If the fine tip replaces the mirrors, the system would readily transform into a MFM data storage device with 300,000 heads.

Appendix A

MFM Images

A.1 Interaction Field Measurements

Following MFM images were taken during the interaction field measurement described in section 4.4.3. Figures 4-3 to 4-6 represent the magnetic state of the 3 × 3 Ni pillar array after a certain field is applied. Following MFM images corresponds to each of the diagram. These images were corrected with only 'Flatten' graphic function in Nanoscope III software.

A.1.1 300 nm Period Array

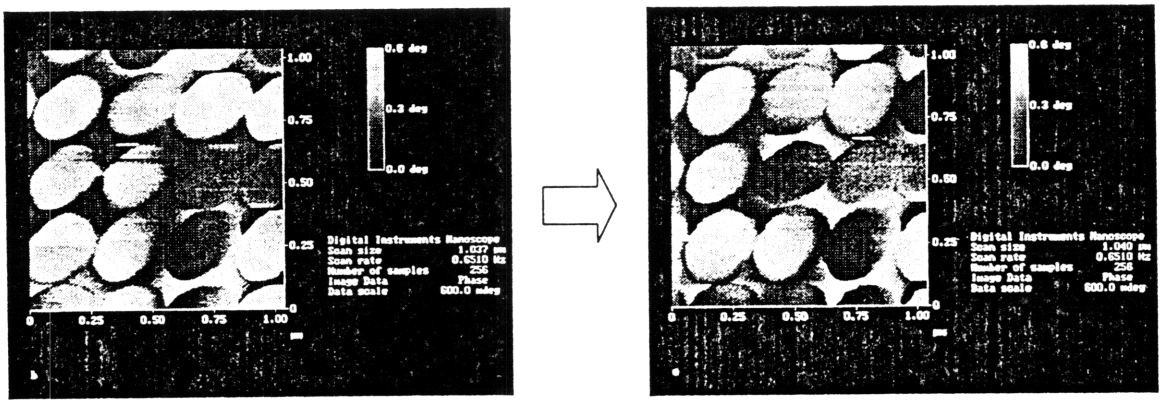

Figure A-1 This figure corresponds to Figure 4-3.

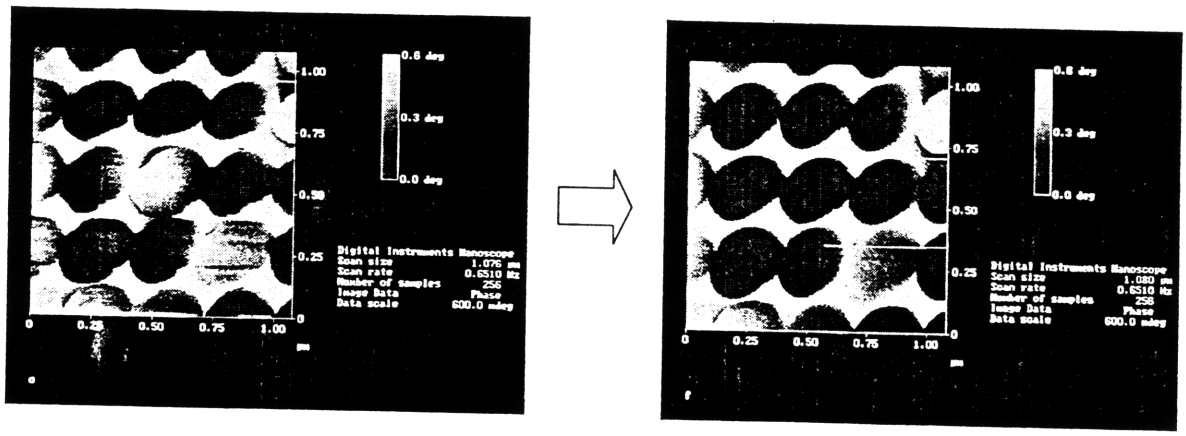

Figure A-2 This figure corresponds to Figure 4-4.

A.1.2 250 nm Period Array

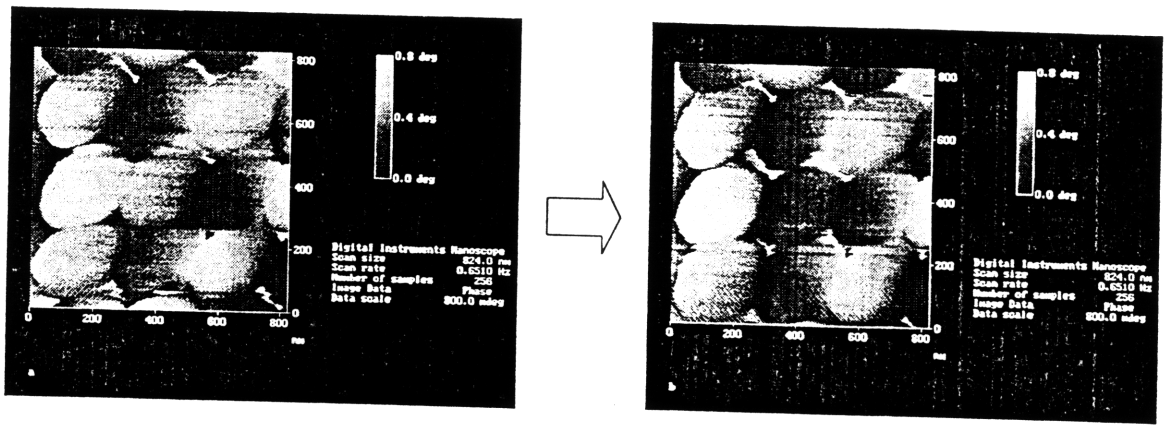

Figure A-3 This figure corresponds to Figure 4-5 (a).

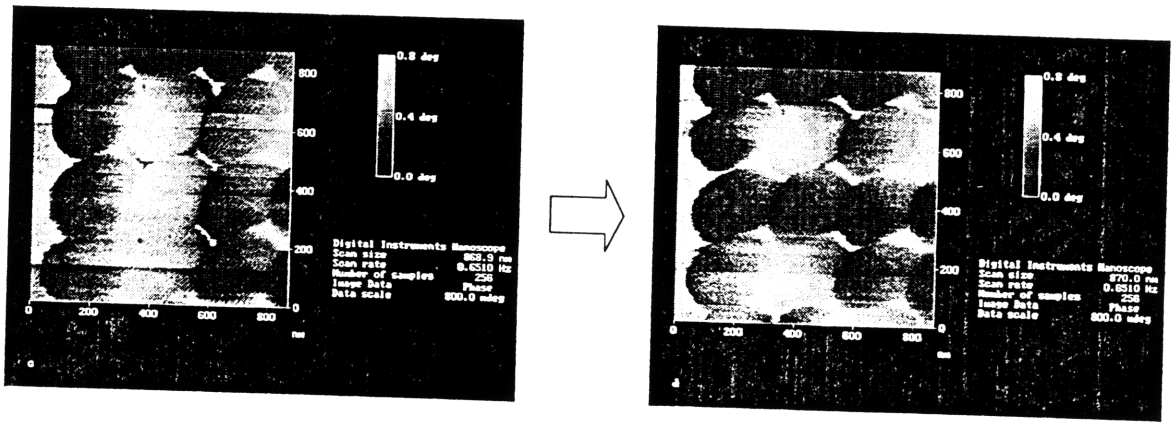

Figure A-4 This figure corresponds to Figure 4-5 (b).

A.1.3 200 nm Period Array

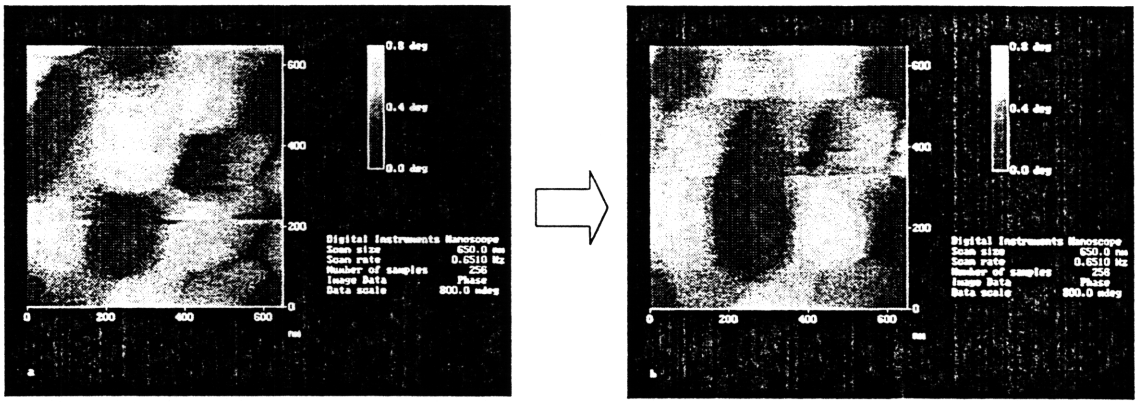

Figure A-5 This figure corresponds to Figure 4-6 (a).

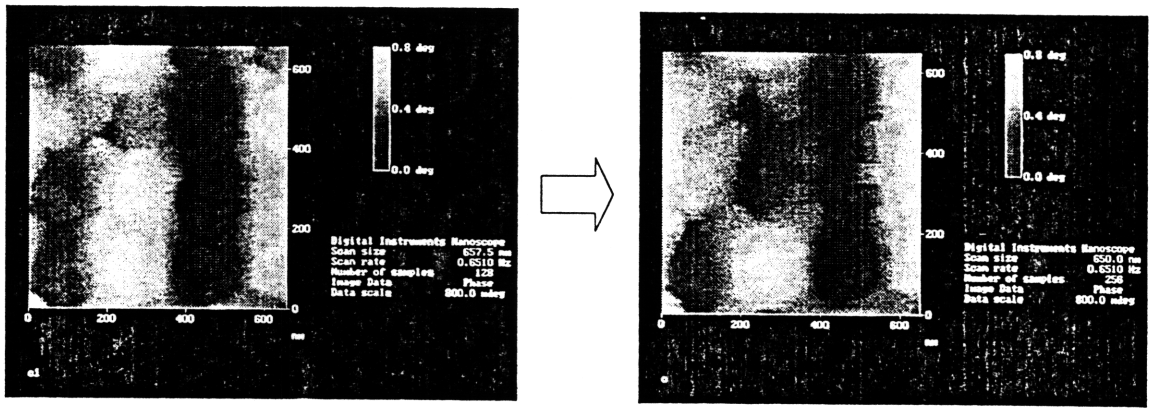

Figure A-6 This figure corresponds to Figure 4-6 (b).

Appendix B

Coil Design

B.1 Introduction

One of the key parts in the PMR setup is the coil which works as an auxiliary pole during writing process. In building a coil, following design requirements should be considered.

1. The range of magnetic field should be at least –1000 Oe to 1000 Oe.
2. The short rise time in the order of milisecond should be achieved.
3. The size of the coil should be small enough to fit into the space between the MFM probe and the sample stage. The maximum space, D3500 could provide, was around 2 cm.

The magnetic wires with AWG ranging from 24 to 32 are supplied by REA Magnetic Wire Corp. Bobbins in three different sizes (2.7, 4.3, and 7.3 mm in radius; 3.3, 6, and 11.6 mm in height) were used to wind the coils around.

B.1 Coil Formula and Calculations

1. Magnetic flux density in the coil

$$B = \sum_{i=1}^{n} \frac{\mu_0 \cdot I \cdot r_i^2}{2\left(r_i^2 + x_i^2\right)^{3/2}} \tag{B.1}$$

where $\mu_0 = 4\pi \times 10^{-7}$ Henry/m, I is current, r is radius of current loop, and x is the distance between point P and center of current loop i. Eq. (B.1) is derived from the law of Biot and

Savart[1]. With this equation, one can calculate the magnetic flux density at any point P on the center axis of the coil with given coil geometry and current.

2. Power generated from the coil

$$P_{coil} = R_{wire} \cdot I^2 \tag{B.2}$$

where R_{wire} is the resistance of the coil. The power, P_{coil}, indicates the minimum power that the current amplifier should provide and the amount of heat generated from the coil.

3. Time constant of coil

$$I = \frac{V}{R}\left(1 - e^{-Rt/L}\right) \tag{B.3}$$

$$L = n \times \Phi / I \tag{B.4}$$

where L is the inductance of the coil, Φ is the magnetic flux, A is the cross-section area of the coil, and V is the input voltage. Eq. (B.3) determines the response speed of the coil to the input signal. The response speed can be represented by the time constant, τ_L, defined as L/R.

[1] See Halliday and Resnick, "Fundamentals of Physics, 4th edition, Wiley (1993)

3. Calculated coil specifications

Coil Number	1	2	3	4
Parameters				
Radius of Bobbin [mm]	2.7	4.3	4.3	4.3
Height of Bobbin [mm]	3.3	6	6	6
Number of Turns	66	270	150	150
Wire AWG Size	30	32	29	27
Diameter of Wire [in]	0.01	0.0088	0.0133	0.0161
Resistance of Wire [Ω/1000 ft.]	103.71	162.00	81.22	51.433
Applied Current [A]	1	1	1	1
Coil				
Magnetic Flux Density [G]	86	204	116	111
Number of Layers	6	11	9	11
Outer Radius [mm]	4.2	6.7	7.3	8.8
Length of Wire [m]	1.44	9.39	5.56	6.20
Resistance [Ω]	0.49	5.00	1.48	1.05
Inductance [H]	1.31×10^{-5}	3.21×10^{-4}	1.01×10^{-4}	9.66×10^{-5}
Time constant [μs]	26.6	64	68	92
Maximum current by Amplifier [A]	12	7.20	12	12
Maximum Magnetic Flux Density[G]	1032	1468	1392	1332

Table B.1 Calculated Coil Specifications

Coil Number	5	6	7	8
Parameters				
Radius of Bobbin [mm]	4.3	7.3	7.3	7.3
Height of Bobbin [mm]	6	11.6	11.6	11.6
Number of Turns	112	360	200	200
Wire AWG Size	26	28	26	24
Diameter of Wire [in]	0.0178	0.0144	0.0178	0.0223
Resistance of Wire [Ω/1000 ft.]	41.023	65.325	41.023	25.67
Applied Current [A]	1	1	1	1
Coil				
Magnetic Flux Density [G]	83	154	88	95
Number of Layers	9	12	8	12
Outer Radius [mm]	8.3	11.6	10.9	13.1
Length of Wire [m]	4.48	21.6	11.67	12.33
Resistance [Ω]	0.6	4.63	1.57	1.03
Inductance [H]	5.46×10^{-5}	9.29×10^{-4}	2.95×10^{-4}	2.41×10^{-4}
Time constant [μs]	91	200	188	232
Maximum current by Amplifier [A]	12	7.77	12	12
Maximum Magnetic Flux Density[G]	996	1196	1056	1140

Table B.2 Calculated Coil Specifications

Based on the provided equation, the properties of the eight coils built in our laboratory are calculated and the results are shown in Table B.1 and Table B.2. For the driving amplifier BOP 36-12M by Kepco, Inc. is used. Its maximum power output is 400 Watt (maximum current: 12 A, maximum voltage: 36 V).

B.3 Experiments

B.3.1 Setup/Procedure

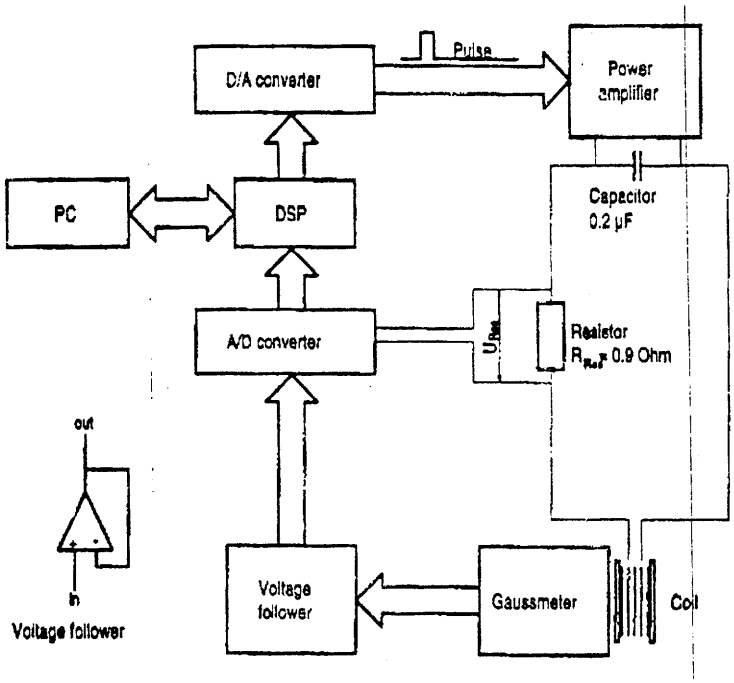

Figure B-1 Experiment setup for coil field measurement

In order to determine the exact field generated from the coil with a given current input, the experimental setup shown in Figure B-1 is used. BOP 36-12M model supports the programming input. This feaure enables the user to input a voltage signal between +5 V and –5 V to output the current between +12 A and –12 A. In our setup, the digital signal processing (DSP) board sends the voltage signal to the amplifier. The user defines the shape

of the current pulse and downloads the information to the DSP board. Then, DSP creates the appropriate signal and sends it to the amplifier. The field generated from the coil is measured by the gaussmeter. The gaussmeter has the analog output port that can be directly connected to the DSP board. DSP stores the field data in the board memory and later PC uploads the data from it. The resulting data is plotted on the PC screen.

B.3.2 Results

In the following pages, the data sheet for the eight coils specified in Table B.1 and Table B.2 are provided. There are two types of figure in the data sheet. One is the plot that shows the magnetic field generated from the coil as function of the input current. This issued in the experiments in Chapter 2 and Chapter 4 to convert the current input into the actual field generated from the coil. The other is the plots that show the shape of the field pulse at a various current pulse amplitudes. The Coil 4 is damaged by accident and therefore couldn't be included in the data sheets.

Coil 1 Data Sheet

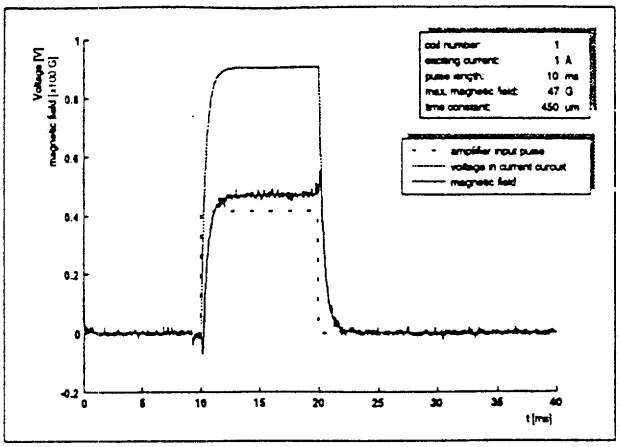

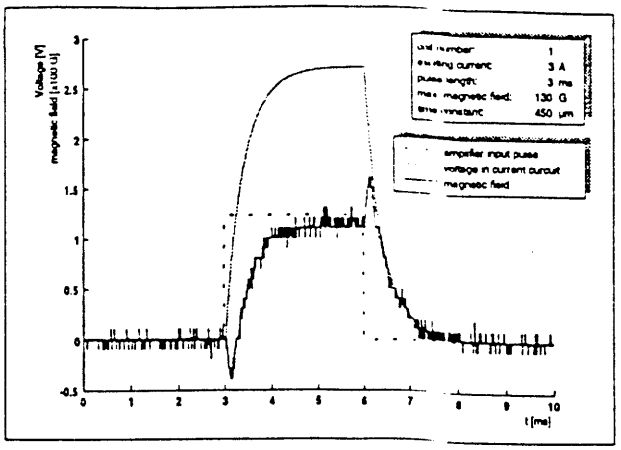

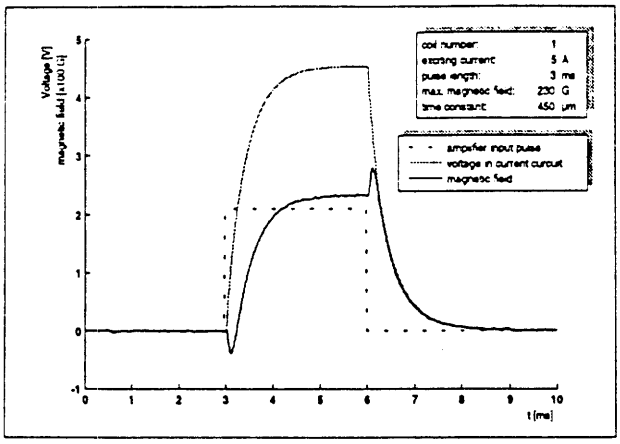

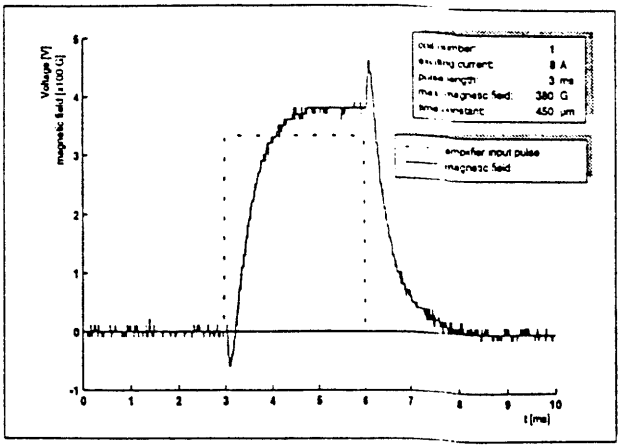

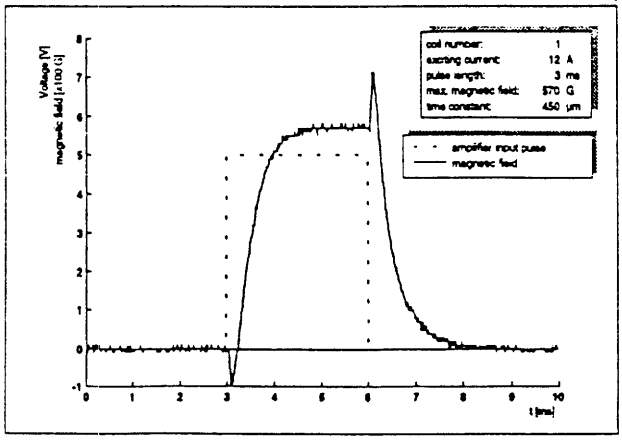

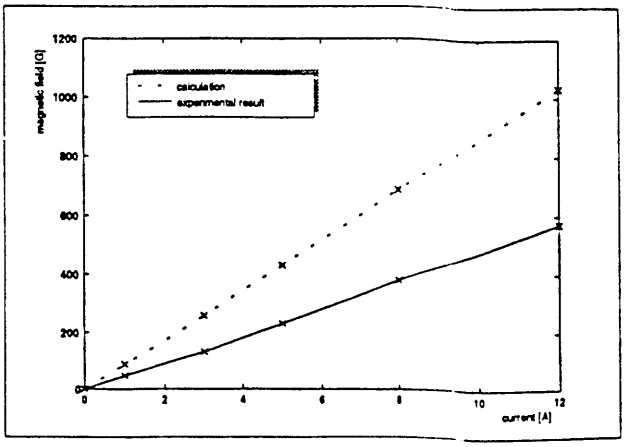

Coil 2 Data Sheet

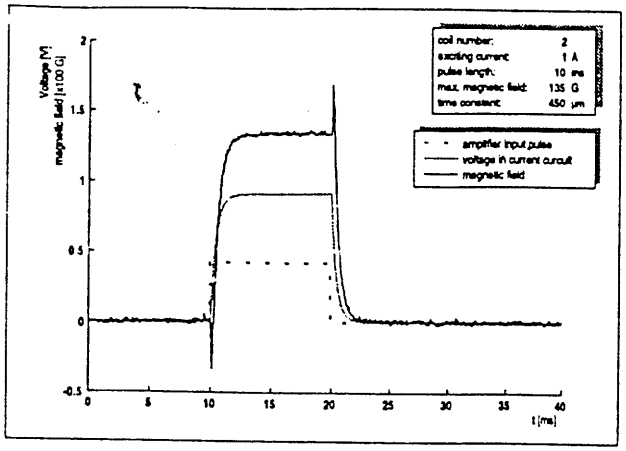

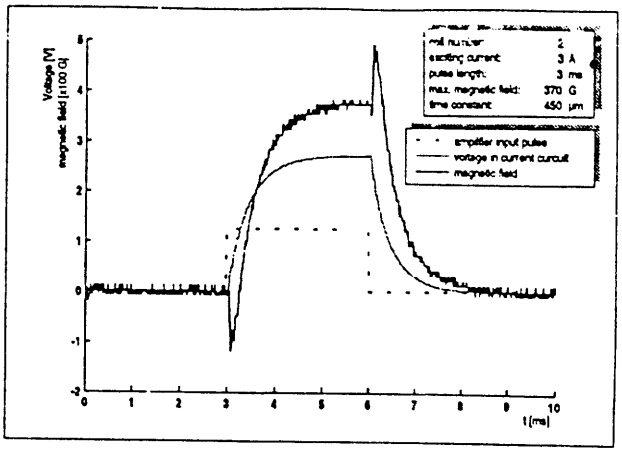

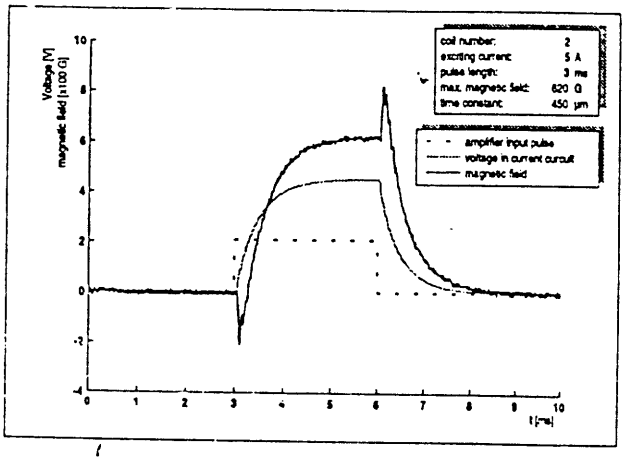

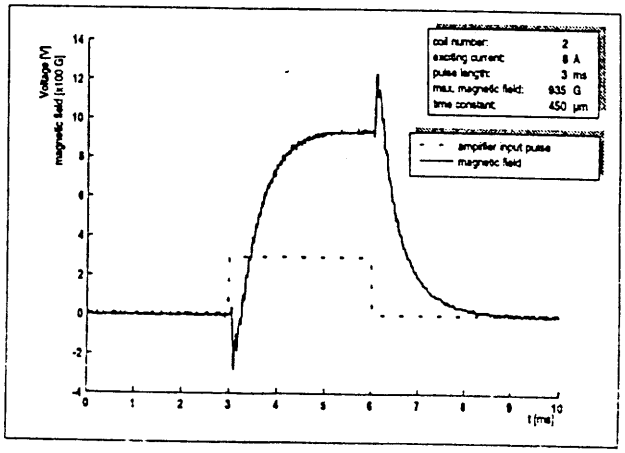

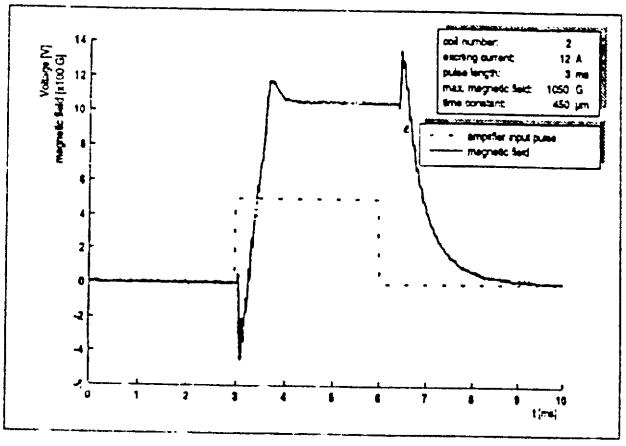

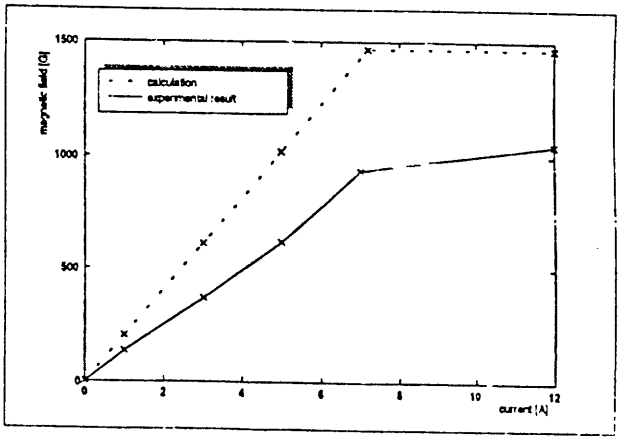

Coil 3 Data Sheet

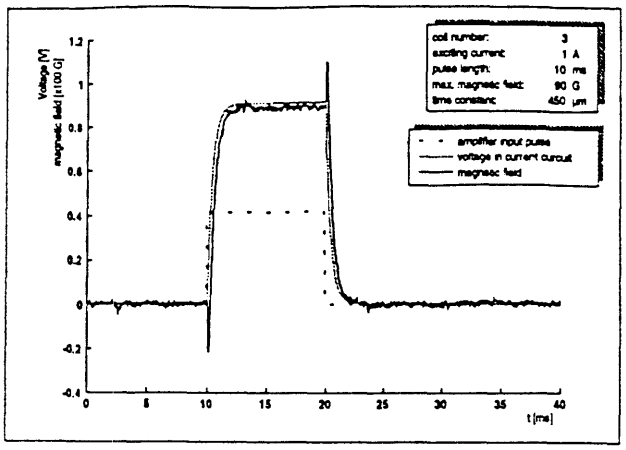

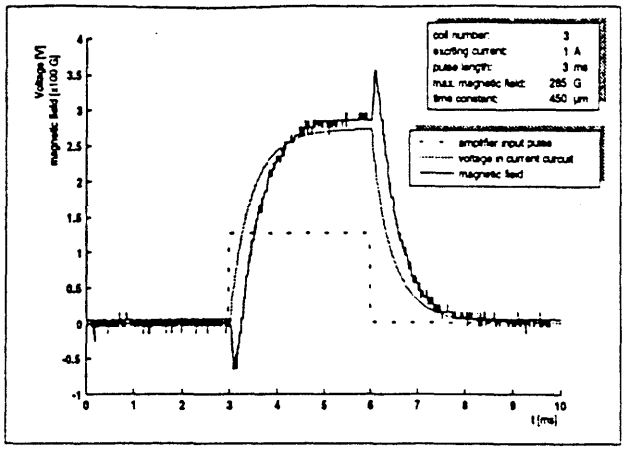

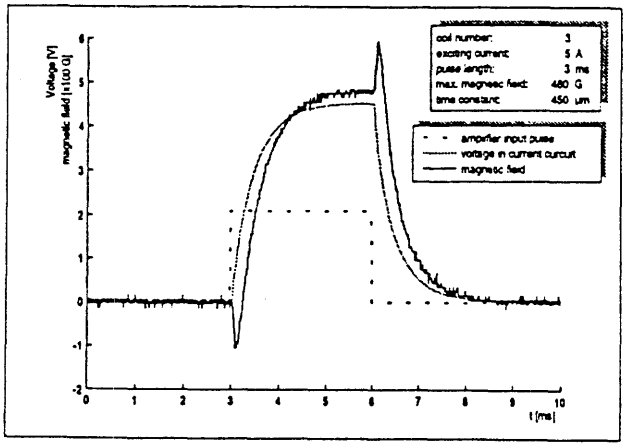

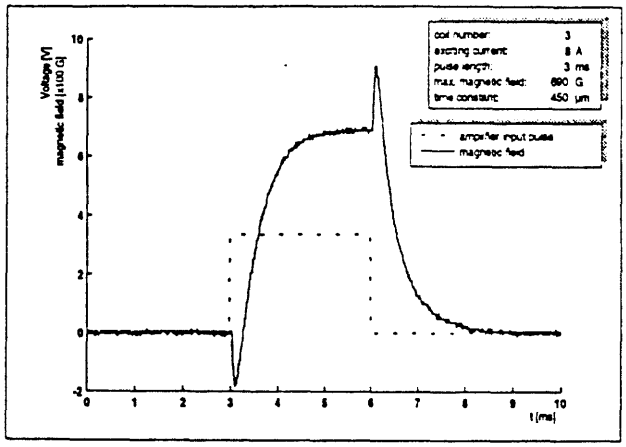

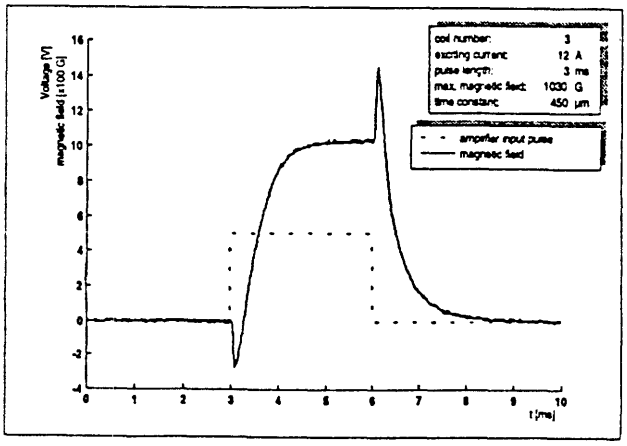

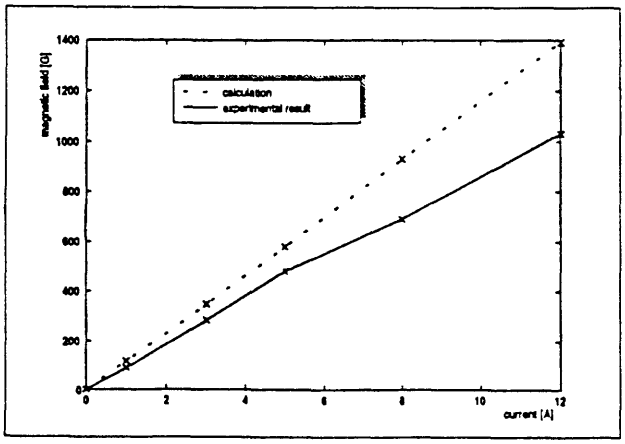

Coil 5 Data Sheet

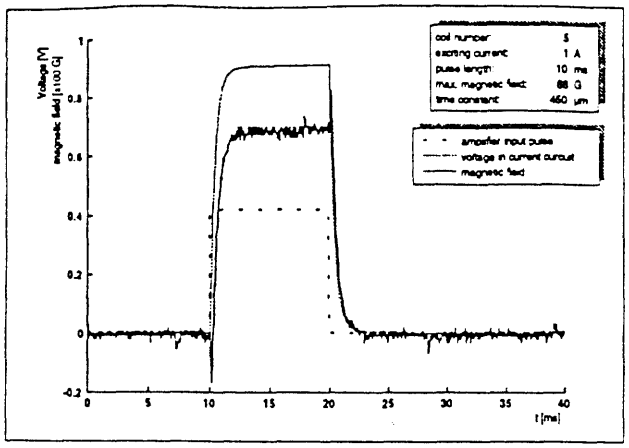

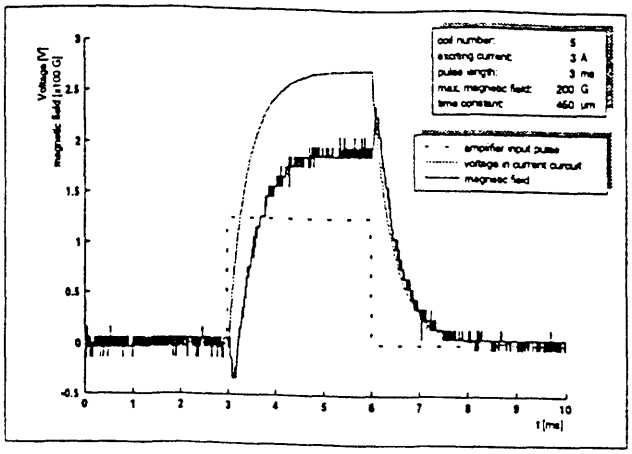

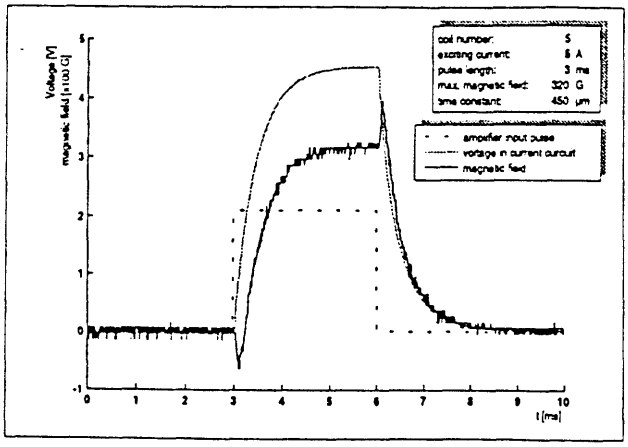

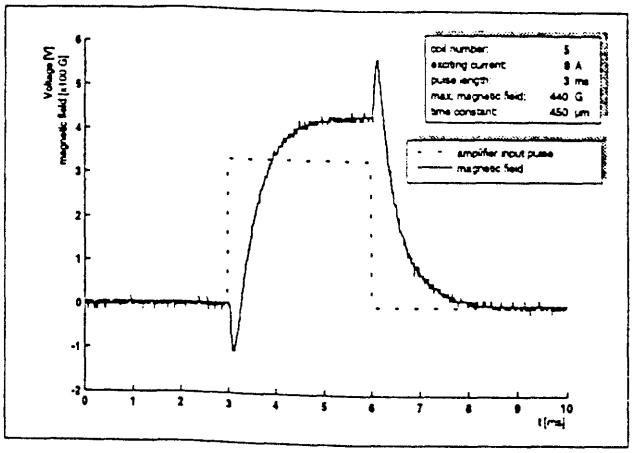

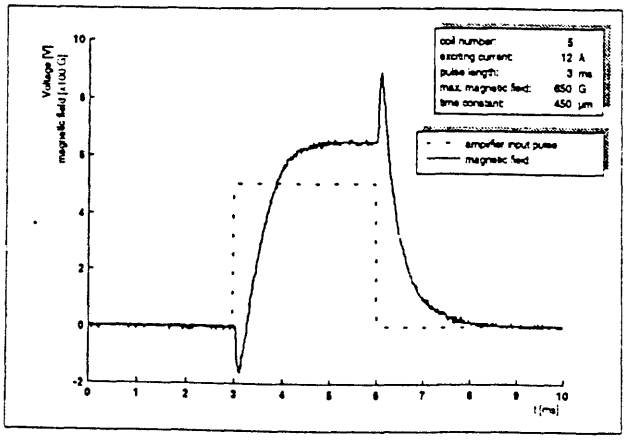

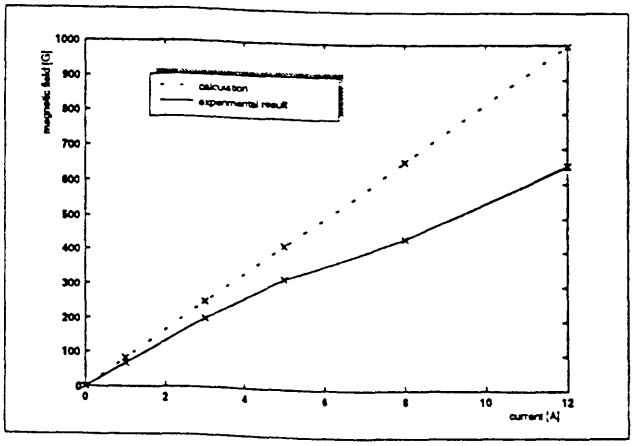

Coil 6 Data Sheet

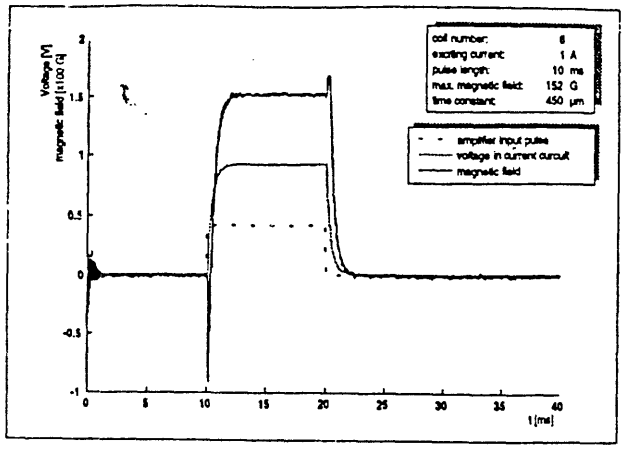

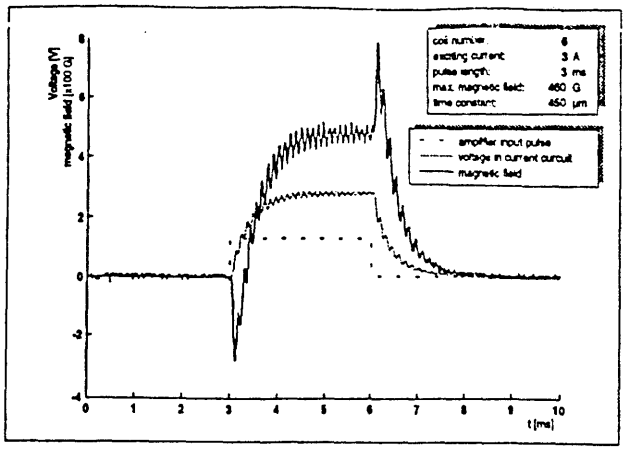

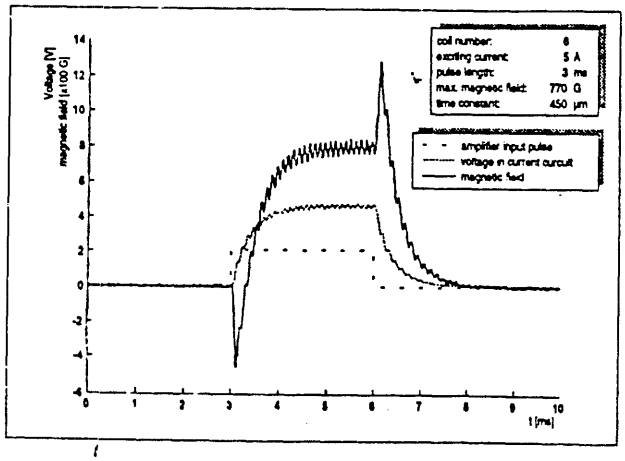

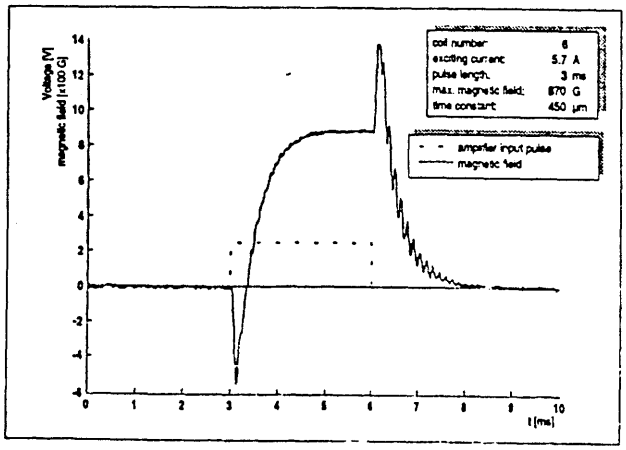

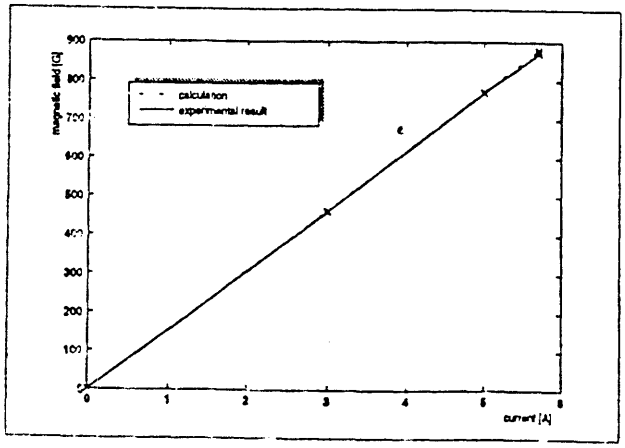

Coil 7 Data Sheet

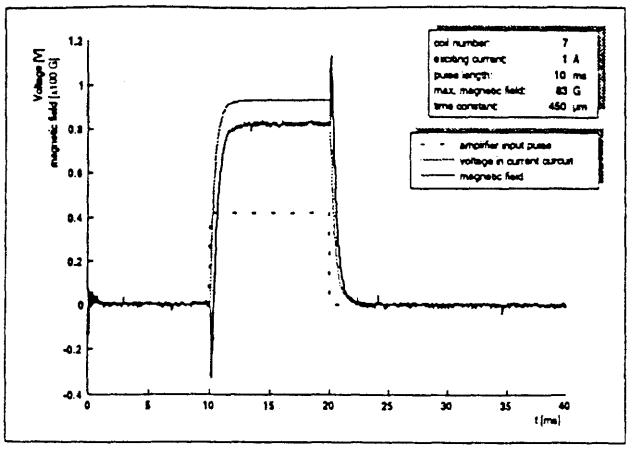

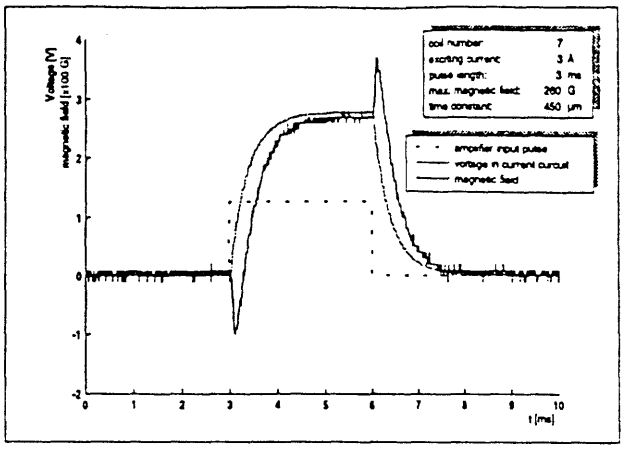

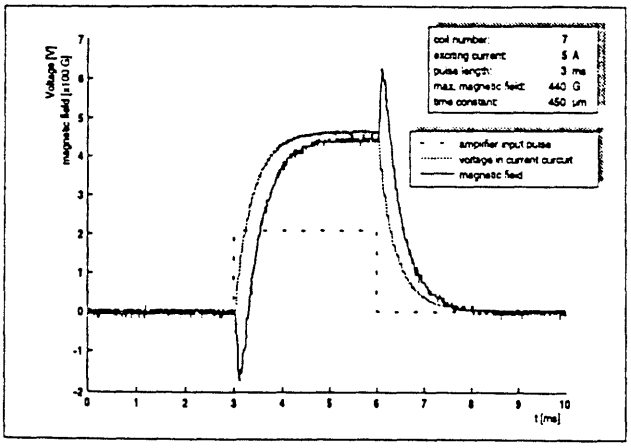

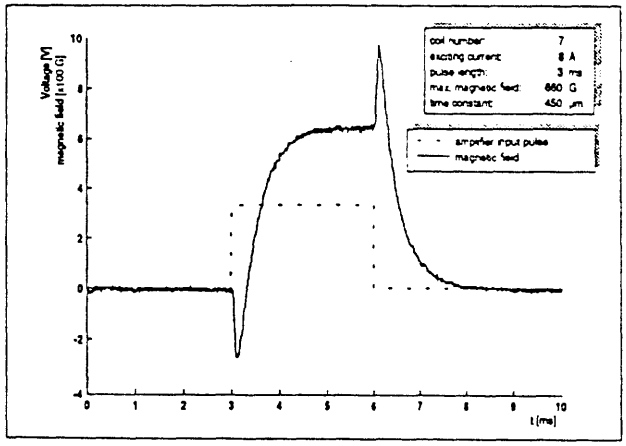

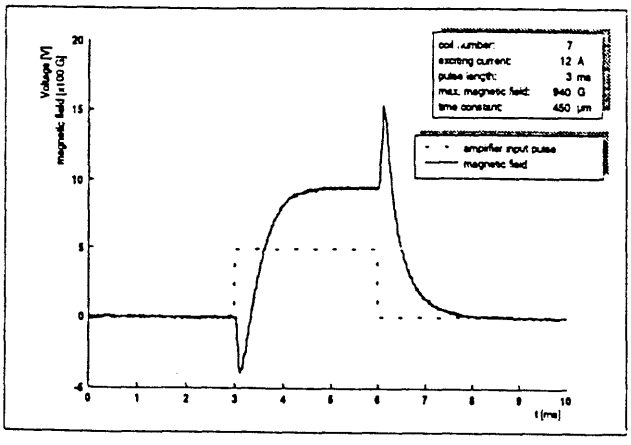

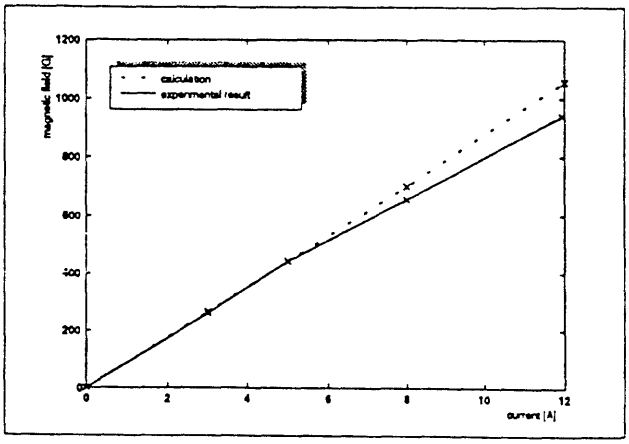

Coil 8 Data Sheet

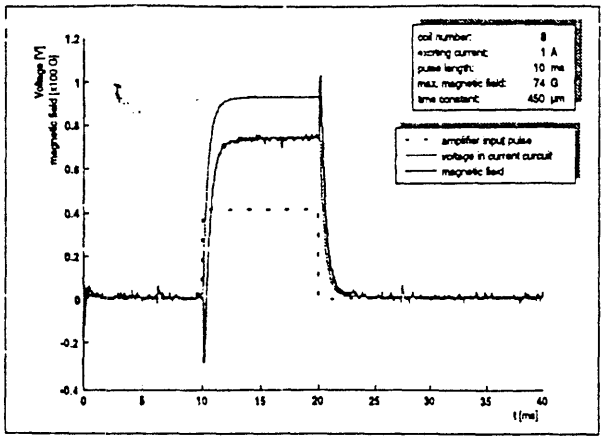

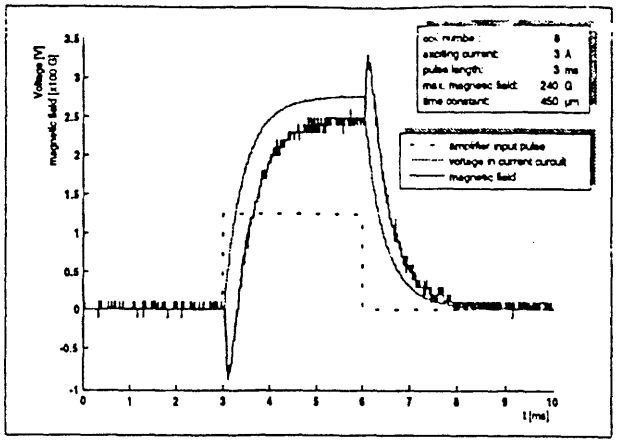

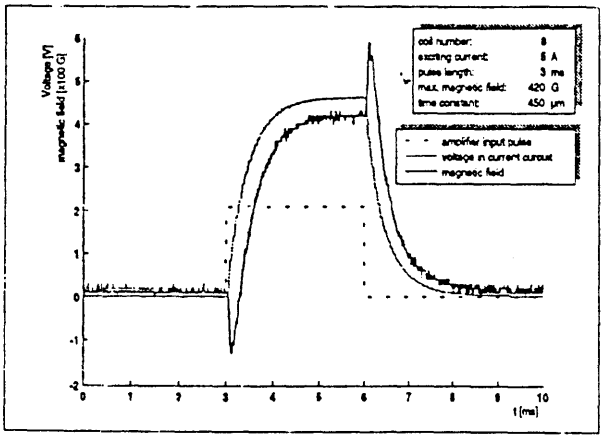

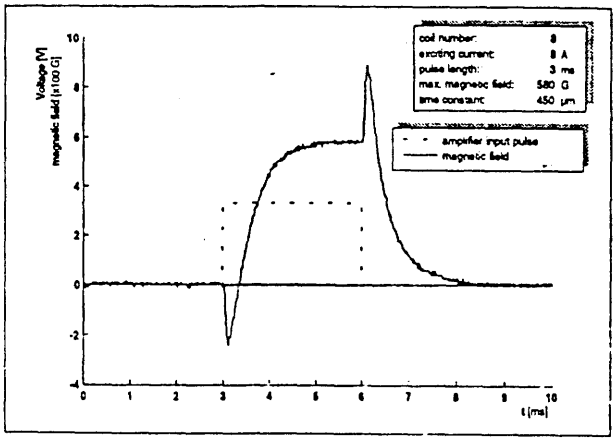

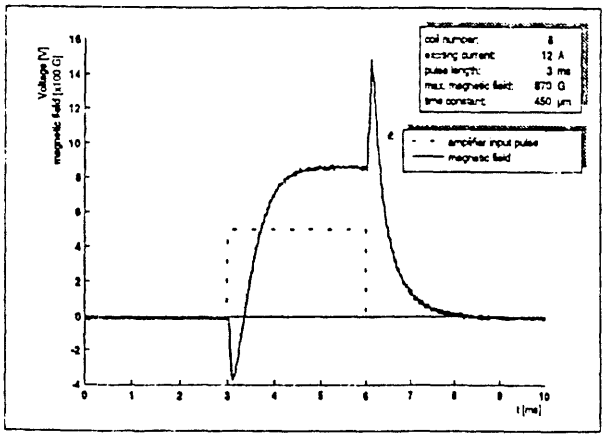

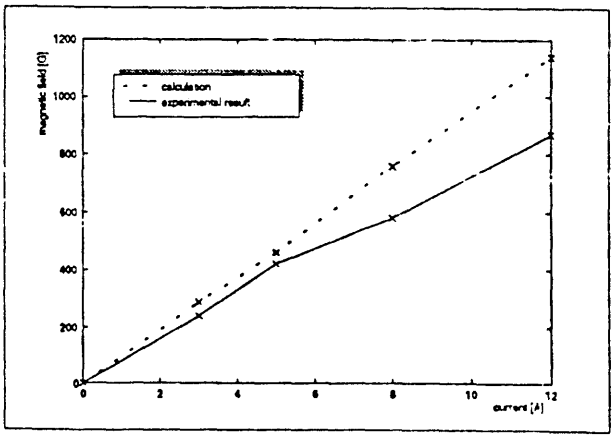

Bibliography

[1] Grochowski, E. and Hoyt, R.F., "Future Trends in Hard Disk Drives", IEEE Trans. Magn 32(3), p1850 (1996)

[2] B.D. Cullity, "Introduction to Magnetic Materials", Addison-Wesley Publishing Company, Inc. 1972 ISBN 0-201-01218-9

[3] R.L. White, Richard M.H. New, R. Fabian and W. Pease, "Patterned Media: A Viable Route to 50 Gbit/in^2 and Up for Magnetic Recording?," IEEE Trans. Magn. 33(1), p990 (1997)

[4] S.E. Lambert, I.L. Sanders, A.M. Patlach, M.T. Krounbi, IEEE Trans. Mag. MAG-23, p3690 (1987)

[5] S.E. Lambert, I.L. Sanders, A.M. Patlach, M.T. Krounbi, S.R. Hetzler, J. Appl. Phys., 69, p4724 (1991)

[6] K. Watanabe, R. Takeda, K. Okada and H. Takino, "Demonstration of Track Following Technique Based on Discreate Track Media", IEEE Trans. Magn. 29(6), p4030 (1993)

[7] J.F. Smyth, S. Schultz and D.R. Fredkin, "Hysteresis in Lithographic Arrays of Permalloy Particles: Experiment and Theory", J. Appl.Phys.69(8), p5262(1991)

[8] J.F. Smyth, S. Schultz and D. P. Kern, H. Schmid and D. Yee, "Hysteresis of submicron permalloy particulate arrays", J. Appl. Phys. 63 p4239(1998)

[9] G.A. Gibson and S. Schultz, "Magnetic Force Microscope Study of the Micromagnetics of Submicrometer Magnetic Particles", J. Appl. Phys. 73(9), p4516 (1993)

[10] G.A. Gibson, J.F. Smyth, S. Schultz and D.P. Kern, "Observation of the Switching Fields of Individual Permalloy Particles in nanolithographic Arrays via Magnetic Force

Microscopy", IEEE Trans. Magn. 27(6), p5187 (1991)

[11]M. Lederman, G.A. Gibson and Schultz, "Observation of Thermal Switching of a Single Ferromagnetic Particle", J. Appl. Phys. 73(10), p6961 (1993)

[12]R. O'Barr and S. Schultz, "Switching Field Studies of Indiidual Single Domain Ni Columns", J. Appl. Phys. 81(8), p5458 (1997)

[13]R. O'Barr, M. Lederman and S. Schultz, "Preparation and Quantitative Magnetic Studies of Single-Domain Nickel Cylinders", J. Appl. Phys. 79(8), p5303 (1996)

[14]R. O'Barr, S.Y. Yamamoto and S. Schultz, "Fabrication and Characterization of Nanoscale Arrays of Nickel Columns", J. Appl. Phys. 81(8), p4730 (1997)

[15]M. Lederman, R. O'Barr, and S. Schultz, "Experimental Study of Individual Ferromagnetic Sub-micron Cylinders", IEEE Trans. Magn 31(6), p3793 (1995)

[16]S.Y. Chou, "Patterned Magnetic Nonostructures and Quantized Magnetic Disks", Proceedings of the IEEE. 85(4), p652 (1997)

[17]S.Y. Chou, P.R. Krauss, and L. Kong, "Nanolithographically Defined Magnetic Structures and Quantum Magnetic Disk", J. Appl. Phys. 79(8), p6101 (1996)

[18]L. Kong and S.Y. Chou, "Nonmonotonic Length Dependence of Switching Field of Nanolithographically Defined Single-Domain Nickel and Cobalt Bars (abstract)", J. Appl. Phys. 79(8), p5067 (1996)

[19]L. Kong, L. Zhuang and S.Y. Chou, "Writing and Reading 7.5 Gbit/in^2 Longitudinal Quantized Magnetic Disk Using Magnetic Force Microscope Tips", IEEE Trans. Magn. 33 p3019 (1997)

[20]R.M.H. New, R.F.W. Pease and R.L. White, "Effect of Magnetocrystalline Anisotropy in Single-Domain Polycrystalline Cobalt Islands", IEEE Trans. Magn. 31(6), p3805 (1995)

[21]R.M.H. New, R.F.W. Pease and R.L. White, "Physical and Magnetic Properties of Submicron Lithographically Patterned Magnetic Islands", J. Vac. Sci. Technol. B 13(3),

p1089 (1995)

[22] R.M.H. New, R.F.W. Pease and R.L. White, "Submicron Patterning of Thin Cobalt Films for Magnetic Storage" J. Vac. Sci. Technol. B. 12(6), p3196 (1994)

[23] R.M.H. New, R.F.W. Pease and R.L. White, R.M. Osgood, and K. Babcock, "Magnetic Force Microscopy of Single-Domain Single-Crystal Iron Particles with Uniaxial Surface Anisotropy", J. Appl. Phys. 79(8), p5851 (1996)

[24] J. Shi, D.D. Awschalom, P.M.Petroff, and K. Babcock, "Assembly and Imaging of Submicron Ferromagnets in GaAs", J. Appl. Phys. 81(8), p4331 (1997)

[25] J. Shi, S. Gider, K. Babcock, and D.D. Awschalom, "Magnetic Clusters in Molecular Beams, Metals, and Semiconductors", Science, Vol. 271, p937 (1996)

[26] A. Fernandez, P.J. Bedrossian, S.L. Baker, S.P. Vernon and D.R. Kania, "Magnetic Force Microscopy of Single-Domain Cobalt Dots Patterned Using Interference Lithography", IEEE Trans. Magn. 32(5), p4422 (1996)

[27] Spallas, J.P., A.M. Hawryluk, and D.R. Kania, "Field Emitter Array Mask Patterning Using Laser Interference Lithography", J. Vac.Sci. Technol. B 13(5), p1973(1995)

[28] Spallas, J.P., R.D. Boyd, J.A. Britten, A. Fernandez, A.M. Hawryluk, M.D. Perry, and D.R. Kania, "Fabrication of sub-0.5 μm Diameter Cobalt Dots on Silicon Substrates and Photoresist Pedestals on 50 cm X 50 cm Glass Substrates Using Laser Interference Lithography", J. Vac.Sci.Technol. B 14(3), p2005 (1996)

[29] G. Meier, M. Kleiber, D. Grundler, D. Heitmann, and Wiesendanger, "Vertical polarization of quantum magnets in high density arrays of nickel dots with small height to diameter ratio", Applied Physics Letters, 72(17) p2168, (1998)

[30] M. Farhoud, M. Hwang, Henry I. Smith, M.L. Schattenburg, J.M. Bae, K. Youcef-Toumi and C.A. Ross, "Fabrication of Large Area Nanostructured Magnets by Interferometric Lithography", IEEE Trans. Magn. 34(4) P.1, p1087 (1998)

[31] T.A. Savas, M.L. Schattenburg, J.M. Carter and H.I. Smith, "Large-area achromatic

interferetric lithography for 100 nm period gratings and grids with novel applications", J. Vac. Sci. Technol. B 14 p4167 (1996)

[32] E.P. Wohlfarth, "Relations between Different Modes of Acquisition of the Remanent Magnetization of Ferromagnetic Particles", J. Appl. Phys. 29 p595(1958)

[33] E.H. Frei, S. Shtrikman and D. Treves, "Critical Size and Nucleation Field of Ideal Ferromagnetic Particles", Physical Review 106(3), p446 (1957)

[34] D.R. Fredkin, T.R. Kochler, "Numerical Micromagnetics of Small Particles", IEEE Trans. Magn. 24(6), p2362 (1988)

[35] D.R. Fredkin, T.R. Koehler, "Ab initio micromagnetic calculations for particles", J. Appl. Phys. 67 p5544 (1990)

[36] D.R. Fredkin, T.R. Koehler, J.F. Smyth and S. Schultz, "Magnetization reversal in permalloy particles: micromagnetic computations", J. Appl. Phys. 69 p5276 (1991)

[37] S. Shtrikman, and D. Treves, "Micromagnetics",p395 of vol. 3 of [15]

[38] A. Aharoni, "Elongated Single-Domain Ferromagnetic Particles", J. Appl. Phys. 63(12), p5879(1998)

[39] A. Aharoni and J.P. Jakubovics, "Field induced magnetization structure in small isotropic spheres", IEEE Trans. Magn. 32 p4463(1996)

[40] J. Gadbois and J-G Zhu, "Effect of Edge Roughness in Nanoscale Magnetic Bar Switching", IEEE Trans. On Magn. 31(6), p3802 (1995)

[41] D.D. Awschalom and D.P. DiVincenzo, "Complex dynamics of mesosopic magnets", Physics Today p43 (April 1995)

[42] B. Doudin, A. Blondel and J.P. Ansermet, "Arrays of Multilayered nanowires", J. Appl. Phys. 79 p6090 (1996)

[43] J. Meier, B. Doudin and J.P. Ansermet, "Magnetic Properties of Nanosized Wires", J. Appl. Phys. 79 p6010(1996)

[44] K. Ounadjela, R. Ferre, L. Louail, J.M. George, J.L. Maurice, L. Piraux and S. Dubois,

"Magnetization Reversal in Cobalt and Nickel Electrodeposited Nanowires", J. Appl. Phys. 81 p5455 (1997)

[45] S.Y. Chou, M. Wie, P.R. Krauss, P.B. Fischer, "Study of Nanoscale Magnetic Structures Fabricated Using Electron-Beam Lithography and Quantum Magnetic Disk", J. Vac. Sci. Technol. B 12(6) (1994)

[46] P.R. Krauss and S.Y. Chou, "Fabrication of Planar Quantum Magnetic Disk Structure Using Electron Beam Lithography, Reactive Ion Etching, and Chemical Mechanical Polishing", J. Vac. Sci. Technol. B 13(6), p2850 (1995)

[47] P.R. Krauss, P.B. Fischer and S.Y. Chou, "Fabrication of Single-Domain Magnetic Pillar Array of 35 nm Diameter and 65 Gbits/in^2 Density", J. Vac. Sci. Technol. B 12(6), p3639 (1994)

[48] S. Kirsch, A. Pollman, M. Thielen, H. Weinforth, A. Carl and E.F. Wassermann, "Preparation and characterization of large scale periodic magnetic microstructures(abstract)", J. Appl. Phys. 81 p5474 (1997)

[49] J.R. Banbury and W.C. Nixon, "The Direct Observation of Domain Structure and Magnetic Fields in the Scanning Electron Microscope", J.Sci.Instrum., 44,889 (1967)

[50] D.J. Fathers et al., "A New Method of Observing Magnetic Domains by Scanning Electron Microscopy", Phys. Status Solidi (a), 20,535 (1973)

[51] D. Gabor, "Microscopy by Reconstructed Wavefronts", Proc. R. Soc. London, Ser. A, 197,454 (1949)

[52] Tonomura et al., "Direct Observation of Fine Structure of Magnaetic Domain Walls by Electron Holography", Phys. Rev. Lett., 44,1430(1980)

[53] J. Unguris et al., "High Resolution Magnetic Microstructure Imaging Using Secondary Electron Spin Polarization Analysis in a Scanning Electron Microscope", J. Micros., 139,RP1 (1985)

[54] A. Aharoni, "Some Recent Development in Micromagnetics at the Weizmann Institute

of Science", J. Appl. Phys. 30, p70S(1959)

[55]G.F. Hughes, "Magnetizatio Reversal in Cobalt-Phosphrus Films", J. Appl. Phys. 54,5306 (1983)

[56]R.H. Victora, "Quantitative Theory for Hysteretic Phenomena in CoNi Magnetic Thin Films", Phys. Rev. Lett., 58,1788 (1987)

[57]R.H. Victora, "Micromagnetic Predictions for Magnetization Reversal in CoNi Films", J.Appl.Phys., 62,4220(1987)

[58]J.-G. Zhu and H.N. Bertram, "Micromagnatic Studies of Thin Metallic Films", J. Appl. Phys., 63, 3248 (1988)

[59]J.-G. Zhu and H. N. Bertram, "Magnetization Reversal in CoCr Perpendicular Thin Films", J. Appl. Phys., 66, 1291(1989)

[60]J.S. Shi, T. Zhu, M. Durlam, E.Chen, S. Tehrani, Y.F. Zheng, and J-G Zhu, "End Domain States and Magnetization Reversal in Submicron Magnetic Structures", IEEE Trans. On Magn. 34(4), p997 (1998)

[61]Y. Zheng and J-G Zhu, "Switching Field Variation in Patterned Submicron Magnetic Film Elements", J. Appl. Phys. 81(8), p5471 (1997).

[62]J. Moreland and P. Rice, "High-resolution, Tunneling-Stabilized Magnetic Imaging and Recording", Appl. Phys. Lett. 57(3), p310 (1990)

[63]T. Ohkubo, J. Kishigami, K. Yanagisawa and R. Kaneko, "Submicron Magnetizing and Its Detection Based on the Point Magnetic Recording Concept", IEEE Trans. Magn, 27(6), p5286 (1991)

[64]T. Ohkubo, J. Kishigami, K. Yanagisawa and R. Kaneko, "Submicron Magnetizing and Its Detection Based on the Point Magnetic Recording Concept", IEEE Translation Journal on Magnetics in Japan, 8(4), p245 (1993)

[65]T. Ohkubo, K. Yanagisawa and R. Kaneko, and J. Kishigami "Magnetic Force Microscopy for High-Density Point Magnetic Recording", Electronics and

Communication in Japan, Part2, Vol. 76, No. 5, p94 (1993)

[66] T. Ohkubo, J. Kishigami, K. Yanagisawa and R. Kaneko, "Reduced-area Magnetic Bit Recording and Detection Using Magetic Force Microscopy Based on Application of Bidirectional Magnetomotive Force", IEEE Trans. Magn, 29(6) (1993)

[67] T. Ohkubo, Y. Maeda and Y. Korhimoto, "Point Magnetic Recording Using a Force Microscope Tip on Co-Cr Perpendicular Media with Compositionally Separated Microstructures", IEEE Trans. Electron. Vol. E78-C, No. 11, p1523 (1995)

[68] S. Manalis, K. Babcock, J. Massie, V. Elings and M. Dugas, "Submicron Studies of Recording Media Using Thin-Film Magnetic Scanning Probes", Appl. Phys. Lett. 66(19), 2585 (1995)

[69] O. Watanuki, Y. Sonobe, S. Tsuji, F. Sai, "Small Magnetic Patterns Written with a Scanning Tunneling Microscope", Trans. Magn. 27(6) (1991)

[70] K.L. Babcock, V.B. Elings, J. Shi, D.D. Awschalom and M. Dugas, "Field Dependence of Microscopic Probes in Magnetic Force Microscopy", Appl. Phys. Lett. 69(5), p705(1996)

[71] R. Proksch, E. Runge, et al, J. Appl. Phys. 78, 3303 (1995)

[72] O. Henkel, "Reamnenzverhalten und Wechselwirkungen in hartmagnitischen Trilchen kollektiven", Phys. Status Solidi 7 p919 (1964)

[73] P.R. Bissel, R.W. Chantrell, G, Tomika, J.E. Knowles and M.P. Sharrock, "Remanent Magnetization and demagnetization measurements on particulate recording media", IEEE Trans. Magn. 25 p3650 (1989)

[74] R. Proksch and B. Moskowitz, "Interactions between Single Domain Particles", J. Appl. Phys. 75(10), p5894 (1994)

[75] M. Pardavi-Horvath, "Switching Properties of a Regular Two-Dimensional Array of Small Uniaxial Particles", IEEE Trans. Magn, 32(5), p4458 (1996)

[76] M. Pardavi-Horvath, G. Jheng, G. Vertesy, and A. Magni, "Interaction Effects in

Switching of a Two Dimensional Array of Small Particles", IEEE Trans. Magn, 32(5), p4469 (1996)

[77] X.H. Huang and M. Pardavi-Horvath, "Local Demagnetizing Tensor Calculation for Arbitrary Nonellipsoidal Bodies", IEEE Trans. Magn. 32(5), p4180 (1996)

[78] L.S. Fan, H.H. Ottensen, T.C. Reiley, and R.W. Wood, "Magnetic Recording Head Positioning at Very High Track Densities Using a Microactuator-Based, Two-Stage Servo System", IEEE Trans. On Magn., 32(5), p3584 (1996)

[79] K. Mori, T. Munemoto, H. Otsuki, Y. Yamaguchi, and K. Akagi, "A Dual-Stage Magnetic Disk Drive Actuator Using a Piezoelectric Devices for a High Track Density", IEEE Trans. Magn, 27(6), p5298 (1991)

[80] Data Storage Magazine, April 1998

[81] H.J. Mamin, B.D. Terris, L.S. Fan, S. Hoen, R.C. Barret, and D. Rugar, "High-Density Data Storage Using Proximal Probe Techniques", IBM J. Res. Develop. Vol. 39 No. 6, p681(1995)

[82] R. Evans, P. Carlson and W. Messner, "Two-Stage Microactuator Keeps Disk Drive on Track", Data Storage magazine, April 1998

[83] S.C. Minne, Ph. Flueckiger, H.T. Soh, and C.F. Quate, "Atomic Force Microscope Lithography Using Amorphous Silicon as a Resist and Advances in Parallel Operation", J. Vac. Sci. Technol. B 13(3), p1380 (1995)

[84] S.C. Minne, S.R. Manalis and C. F. Quate, "Parallel Atomic Force Microscopy Using Cantilevers with Integrated Piezoresistive Sensors and Integrated Piezoelectric Actuators", Appl. Phys. Lett. 67(26), p3918 (1995)

[85] S.C. Minne, G Yaralioglu, S.R. Manalis, J.D. Adams, J. Zesch, A. Atalar and C.F. Quate, "Atomated Parallel High-Speed Atomic Force Microscopy", Appl. Phys. Lett. 72(18), p2340 (1998)

[86] S.C. Minne, J.D. Adams, G Yaralioglu, S.R. Manalis, A. Atalar and C.F. Quate,

"Centimeter Scale Atomic Force Microscope Imaging and Lithography", Appl. Phys. Lett. 73(12), p1742 (1998)

[87] S.R. Manalis, S.C. Minne and C. F. Quate, "Atomic Force Microscopy for High Speed Imaging Using Cantilevers with and Integrated and Sensor", Appl. Phys. Lett. 68(6), p871 (1996)

[88] S.R. Manalis, S.C. Minne and A. Atlar and C. F. Quate, "High-Speed Atomic Force Microscopy Using an Integrated Actuator and Optical Lever Detection", Rev. Sci. Instrum. 67(9), p3294 (1996)

[89] D.W. Pohl, "Some Thoughts about Scanning Probe Microscopy, Micromechanics, and Storage", IBM J. Res. Develop. Vol. 39 No. 6, p701 (1995)

[90] D. Rugar, H.J. Mamin, P. Guethner, S.E. Lambert, J.E. Stern, I. MacFadyen, and T. Yogi, "Magnetic Force Microscopy: General Principles and Application to Longitudinal Recording Media", J. Appl. Phys. 68(3), p1169 (1990)

[91] D.A. Walters, J.P. Cleveland, N.H. Thomson, P.K. Hansma, M.A. Wendman, G. Gurley, and V. Elings, "Short Cantilever for Atomic Force Microscopy", R.S.I. 67(10) 3583-90 (1996)

[92] H.J. Mamin and D. Rugar, "Thermo-mechanical Writing with an Atomic Force Microscope Tip", Appl. Phys. Lett. 61(8), p1003 (1992)

[93] S.G. Kim, K.H. Hwang, Y.J. Choi, Y.K. Min and J.M. Bae, "Micromachined Thin-Film Mirror Array for Reflective Light Modulation", Annals of the CIRP Vol. 46/1/1997 p455

[94] S.G. Kim, K.H. Hwang, J. Hwang, M.K. Koo and G.W. Lee, "Thin-film Micromirror Array", SID Asia Disply 98 (1998)

[95] K.H. Hwang, Y.J. Song and S.G. Kim, "Thin-Film Micromirror Array for High-Brightness Projection Displays", Japanese Journal of Applied Physics, Vol 37, p7704(1998)

[96] Y. Xu, S.A. Miller and N.C. Mcdonald, in the Proceedings of Transducers '95 (Royal Swedish Academy of Engineering Science, IVA, Stockholm, Sweden, 1995), p636 n

[97] S. Watanabe and T. Fujii, "Micro-Fabricated Piezoelectric Cantilever For Atomic Force Microscopy", Rev. Sci. Instrum. 67(11), p3898 (1996)

[98] D.W. Pohl, R. Moller, "Tracking Tunneling Microscopy", Rev. Sci. Instrum. 69(6) (1998)

[99] J.J. Saenz, N. Garcia, P. Grutter, E. Meyer, H. Heinzelmann, R. wiesendanger, L. Rosenthaler, H.R. Hidber, H.J. and Guntherodt, "Observation of Magnetic Forces by the Atomic Force Microscope", J. Appl. Phys. 62(10), p4293 (1987)

[100] J.J. Saenz, N. Garcia, "Theory of Magnetic Imaging Force Microscopy", Appl. Phys. Lett. 53(15) (1988)